

# Studies of Length Scales in Semiconducting Polymers using Scanning Photocurrent Contrast Microscopy

A Thesis submitted in partial fulfillment of the  
requirements of the degree of

*Doctor of Philosophy*

By

**Dinesh Kabra**



Chemistry and Physics of Materials Unit  
Jawaharlal Nehru Centre for Advance Scientific Research  
(A Deemed University)  
Bangalore – 560064 (India)  
May 2007

## **Declaration**

---

---

I hereby declare that the thesis entitled “Studies of Length Scales in Semiconducting Polymers using Scanning Photocurrent Contrast Microscopy.” is an authentic record of research work carried out by me under the supervision of Prof. K. S. Narayan at the Molecular Electronics Lab, Chemistry and Physics of Materials Unit, Jawaharlal Nehru Centre for Advanced Scientific Research, Bangalore, India. The thesis has not previously formed the basis for the award of any Degree, Diploma, Associateship or Fellowship.

Dinesh Kabra

**To**

**My Dear Parents & Wife '*Niti*'**



**JAWAHARLAL NEHRU CENTRE FOR ADVANCED  
SCIENTIFIC RESEARCH**

Jakkur, Bangalore 560064, India

K. S. NARAYAN

PHONE: 91 80 2208 2822

FAX: 91 80 2208 2766

e-mail: narayan@jncasr.ac.in

---

May 16<sup>th</sup>, 2007

**Certificate**

Certified that the work described in this thesis titled “Studies of Length Scales in Semiconducting Polymers using Scanning Photocurrent Contrast Microscopy” has been carried out by *Mr. Dinesh Kabra* under my supervision at the Molecular Electronics Lab, Chemistry and Physics of Materials Unit, Jawaharlal Nehru Centre for Advanced Scientific Research, Bangalore, India.

Prof. K. S. Narayan

---

## ACKNOWLEDGEMENT

---

---

*“Outstanding achievements are not possible in vacuum. It needs lot of help and assistance besides a healthy environment, luckily I had.”*

I had been very fortunate to work under excellent guidance of **Prof. K. S. Narayan**. At this moment, I would like to thank him for introducing me to the area of conjugated polymer. The freedom that he gave me in workspace, the support, constructive criticism, abundant scientific inputs during discussions helped me to shape up my research career. His never subsiding enthusiasm and high spirit was a continuous source of motivation to carryout high quality science. At the end of this fruitful journey with him full of continuous learning, I have emerged as a better candidate personally and professionally. I would also express my gratitude to his family for kind moral support and timely good dinner on festivals.

I would like to take opportunity to show my gratitude to **Prof. C. N. R. Rao**, chairperson of C.P.M.U., whose presence is a big source of inspiration.

I thank my collaborators **Prof. N. S. Vidhyadhiraja (T.S.U., JNCASR)** and **Prof. S. Ramakrishnan (I.P.C. department, IISc)**. I thank them for the encouraging discussions and guidance for solving the problems.

I thank my friends and collaborators **S. Sriram (Sayanu)**, **Dr. K. Nagesh**, **Dhritiman Gupta**, **Dr. Vasuda Bhatia**, **Asst. Prof. Th. B. Singh (Johannes Kepler University, Linz- Austria)** for the science and other general fun filled discussions we had together.

A very special thanks to my all lab colleagues, present and past, **Dr. Alagiriswamy**, **Dr. A. G. Manoj**, **Dr. S. Dutta**, **Basavraj**, **Arun**, **Manu**, **Hemant**, **Shruti**, **Jasmeet**, **Sachi**, **Manojit**, **Sajini**, **Ravi** for useful scientific and non-scientific discussions and for making my stay very pleasant.

I express a very special thanks to **Ms. Priya Sony** and **Mr. Ankur Modi** for their constant encouragement and mental support throughout my academic career.

I acknowledge all my Ph.D. batchmates and other friends in JNCASR and IISc for constructive scientific interactions and an enjoyable stay during the course of my Ph.D.

I also acknowledge Technical, Administrative and Academic staffs for their help in respective field during my stay and a special thanks to *Mr. A. N. Jaychandra* for his kind support.

And finally on a more personal level:

I would like to express my deep sense of gratitude to my dearest parents and family members for their blessings, support and inspiration to maneuver the whole. Finally, I must express my deepest appreciation to my wife *Niti*. Without her constant encouragement, inspiration, help and enthusiasm, it would never have been possible to accomplish the Ph.D. smoothly.

*Dinesh*

# Preface

---

---

Semiconducting polymer films when photoexcited with defined beam profiles generate excess charge carriers from the electronically excited state, which eventually spread over a volume exceeding the beam-sample cross-section. The thesis focuses on the studies of these length scales in model polymer systems, which are of fundamental importance in understanding the transport mechanisms and are crucial parameters for device development. A modified scanning photocurrent contrast microscopy technique was designed and implemented for these studies. Patterned device substrates with dimensions over a large range (1  $\mu\text{m}$  to 2 mm) were used in these experiments. This approach essentially utilized a photocurrent-contrast imaging of the polymer film sandwiched between the patterned substrate and a top Schottky-type electrode, where the incident light beam scans regions beyond the uniform electric field region of the overlapping electrodes. The electron/hole transport processes can be independently evaluated by positioning the narrow-light beam selectively over the anode/cathode regions, enabling the estimation of the efficacy of hole transport vis-à-vis electron transport. Sizable photocurrent-signals between the electrodes are observed even at lateral distances several microns away from the counter electrode. While this current in general decays monotonically as a function of distance from the counter electrode, the functional forms depends on the specific microscopic properties of the polymer semiconductor, hence the method is particularly suited to directly estimate the degree of

disorder and spatial anisotropy in the electrical transport parameters. These length scales in the first approximation corresponds to the mobility-lifetime product ( $\mu\tau$ ). The values of these intrinsic parameters are extracted for variety of semiconducting polymers (poly(3-hexylthiophene)(P3HT), Poly(2-methoxy-5-(2-ethylhexyloxy)-1,4-phenylene vinylene) (MEHPPV) and Poly(9,9-dioctylfluorene-alt-bithiophene) (PFO-TT)). The implications of these results are discussed in detail in the thesis.

An outcome of the studies led to the explanation of lateral photovoltaic (LPV) effect observed in these systems. LPV is observed using a local optical probe on device structures consisting of the semiconducting polymer film with a Schottky type back contact and a front pair of ohmic contacts. The measurements carried out for a large range of interelectrode length ranging from 25  $\mu\text{m}$  to 2 cm is studied in detail as a function of temperature, wavelength, and modulation frequency of the photoexcitation. A spreading impedance approach in the context of a discrete circuit element model is used to obtain a quantitative understanding of the spatial dependence and the frequency response of the LPV.



# List of Publications

---

---

## Reference related to thesis work

- 1) **D. Kabra** and K. S. Narayan "Direct Estimation of Transport Length Scales in Semiconducting Polymers" *Adv. Mat.*, 2007 (DOI: 10.1002/adma.200602405)
- 2) **D. Kabra**, S. Shriram, N. S. Vidhyadhiraja and K. S. Narayan "Charge Carrier Dynamics in Organic Semiconductors by Position Dependent Optical-Probing" *J. Appl. Phys.* Vol. **101**, pp 65110-65115 (2007).
- 3) **D. Kabra**, N. S. Vidhyadhiraja and K. S. Narayan "Lateral Photovoltaic Effect in Conjugated Polymers Based Structures For Position Sensitive Detectors" *Cintelliq Organic Electronics Conference - 2006*
- 4) K. S. Narayan, **D. Kabra**, and S. Dutta "Polymer Based Photodetectors", *Mat. Res. Soc. Symp. Proc. Vol. 814* © 2004.
- 5) **D. Kabra**, Th. B. Singh and K. S. Narayan "Semiconducting Polymer Based Position Sensitive Detectors", *Appl. Phys. Lett.* Vol. **85**, pp. 5073-5075 (2004).
- 6) J. Verma, **D. Kabra**, K. S. Narayan and N. S. Vidhyadhiraja "A Study of Charge Transport in Disordered Organic Films" *European Phys. of J. Appl. Phys.* 2007 (submitted)

## Research News

- 7) **D. Kabra** and K. S. Narayan "Polymer Photo-detector" *Laser Focus World*, Feb. 2005

## Miscellaneous Publicaions

- 8) V. Bhatia, D. Gupta, **D. Kabra** and K. S. Narayan, "Optical and Electrical Features of Surface Ordered Regioregular Polyhexylthiophene" *J. Mat. Science* 2007 (in press)
- 9) K. Nagesh, D. Gupta, **D. Kabra**, K. S. Narayan and S. Ramakrishnan, "Tunable two-colour patterning of MEHPPV from a single precursor", *J. Mat. Chem.* Vol. **17**, pp 1682-1686 (2007)

- 10) D. Gupta, **D. Kabra**, K. Nagesh, S. Ramakrishnan, K. S. Narayan, "Efficient Bulk Heterojunction Photovoltaic Cell based on Energy Transfer in Graded Band-gap MEH-PPV Polymers.", *Adv. Func. Mat.* Vol. **17**, pp 226-232 (2007)
- 11) K. Nagesh, **D. Kabra**, K. S. Narayan, S. Ramakrishnan, "Modulating phase-separation in blends of MEHPPV-x with different conjugation lengths.", *Synth. Met.* Vol. **155**, pp- 295, 2005. (On Cover page)
- 12) **D. Kabra**, Kripasindhu Sardar and K. S. Narayan, "Gallium Nitride nanoparticles for solar-blind detectors.", *Proc. Indian Acad. Sci. (Chem. Sci.)* Vol. **115**, pp 459-463 (2003).

### **Research News**

- 13) D. Gupta, **D. Kabra**, K. Nagesh, S. Ramakrishnan, K. S. Narayan, "Plastic Solar Cells Make Light Work", *Chemistry World* (Royal Society of Chemistry), July 24th, 2006.

# TABLE OF CONTENTS

---

<b>1</b>	<b>GENERAL INTRODUCTION</b>	<b>1</b>
<b>2</b>	<b>DEVICE FABRICATION AND MEASUREMENT TECHNIQUES</b>	<b>43</b>
	2.1 INTRODUCTION	
	2.2 MATERIALS	44
	2.2.1 Poly(3-hexylthiophene) (P3HT)	
	2.2.2 Poly(2-methoxy-5-(2-ethylhexyloxy)-1,4-phenylene vinylene) (MEHPPV)	
	2.2.3 Poly(dioctylfluorene-co-bithiophene) (PFO – TT)	
	2.3 DEVICE FABRICATION PROCESS	53
	2.3.1 Two Terminal Device Structures	
	2.3.2 Three Terminal Device Structures	
	2.4 EXPERIMENTAL TECHNIQUES USED IN CONJUNCTION WITH THE DEVICES	56
	2.4.1 Intensity Modulated Photocurrent Spectroscopy	
	2.4.2 I-V Measurement Setup	
	2.4.3 DC transient Measurement Setup	
	2.4.4 Temperature Dependent Measurement Setup	
	2.4.5 Electron Microscopy	
	2.4.6 X-ray Diffraction (XRD) and Grazing Incidence X-ray Diffraction (GIXRD) Measurements	
	2.4.7 Spatial Photocurrent Measurement Setup	
	2.4.8 Optical Scanning Probe Microscopy	
	2.5 ADVANTAGE OF PHOTOCURRENT MICROSCOPY	68
<b>3</b>	<b>LENGTH SCALES OF PHOTO-GENERATED CHARGE CARRIERS IN SEMICONDUCTING POLYMERS</b>	<b>75</b>
	3.1 INTRODUCTION	
	3.2 STRATEGY	76
	3.3 EXPERIMENTAL STUDIES	79
	3.3.1 Photocurrent Modulation Spectroscopy	
	3.3.2 Scanning Electron Microscopy	
	3.3.3 Scanning Photocurrent Contrast Microscopy	
	3.4 SIMULATIONS	90
	3.5 DISCUSSION	95
	3.6 CONCLUSIONS	98

<b>4</b>	<b>ENHANCEMENT IN ELECTRICAL TRANSPORT AND AMBIPOLAR CONDUCTION</b>	<b>101</b>
	4.1 INTRODUCTION	
	4.2 OPTICAL AND ELECTRICAL ANISOTROPY	103
	4.2.1 Polarized Absorption Spectroscopy	
	4.2.2 Polarized Photocurrent Spectroscopy	
	4.2.3 Field Emission Scanning Electron Microscope	
	4.3 SCANNING PHOTOCURRENT CONTRAST MICROSCOPY	107
	4.4 DISCUSSION	113
	4.5 SUMMARY	115
<b>5</b>	<b>STUDIES OF CHARGE CARRIER DYNAMICS USING LATERAL PHOTOVOLTAIC EFFECT: POSITION SENSITIVE DETECTORS</b>	
	5.1 INTRODUCTION	119
	5.2 PHOTOPHYSICS OF LPV AND DISCRETE CIRCUIT ELEMENT MODEL	121
	5.3 ROUTE TO LPV OBSERVATIONS	127
	5.3.1 Photocurrent Spectroscopy	
	5.3.2 Wavelength Dependence	
	5.3.3 I-V Characteristics	
	5.3.4 Channel Length Dependence of LPV	
	5.3.5 Chopper frequency dependence of LPV	
	5.3.6 Temperature Dependence of LPV	
	5.3.7 External Bias Dependence on LPV	
	5.3.8 2D Optical Scanning	
	5.4 SIMULATIONS	140
	5.5 DISCUSSION	144
	5.6 CONCLUSIONS	146
<b>6</b>	<b>SUMMARY AND FUTURE DIRECTIONS</b>	<b>151</b>
	6.1 SUMMARY	
	6.2 FUTURE DIRECTIONS	153

# CHAPTER 1

## General Introduction

---

The field of polymer electronics has developed at an impressively fast pace over the last decade. The primary interest and pursuits in this field three decades ago were to realize polymers, which had metallic characteristics in terms of the electronic conductivity. The field evolved over a period, with the emphasis shifting from studying metallic properties in these systems to utilizing the semiconducting features in the undoped state of these materials. Studies of metallicity in model conducting polymers such as polyacetylene was pioneered by Heeger, MacDiarmid and Shirakawa who were honored with the Nobel prize for chemistry in the year 2000 [1, 2]. Prior to this novel discovery, polymers were considered to be important plastic materials as they were easy to process from solution and their mechanical properties could be tailor-made during synthesis. However, intrinsically conducting polymers sounded something like a paradox. PA (poly(acetylene)) is the classic example of conjugated polymers, which displays metallic conductivity upon doping with Iodine. Conducting polymers such as Poly(aniline) (PAni), poly(3,4-ethylenedioxythiophene) PEDOT and polypyrrole have been shown to be more viable from the utility and application standpoint.

The field received a tremendous impetus in the last two decades on realization of optoelectronic devices based on the semiconducting nature of these materials. In particular, the phenomenon of electroluminescence in conjugated semiconducting polymers spurred wide interest in the field. [3]. Such as the light emitting diodes and polymer based photovoltaic cells have drawn considerable attention. Rapid strides in the development of devices have been made over a relatively short period since the discovery of the electroluminescence in these systems [4].

The emission properties involve exciton formation and radiative decay while the photovoltaic properties rely on efficient photoinduced charge separation. In

electroluminescent (EL) devices, electrons and holes are injected from the cathode and anode, respectively, which traverse through the hole transporting & the electron transporting layers to provide higher possibility of exciton formation and subsequently radiative recombination. In photovoltaic, the active medium typically consists of donor-acceptor species. Upon the absorption of light by donor polymer, an ultrafast electron transfer (within 50 fs) to molecular acceptor takes place. Under appropriate mixing conditions, interpenetrating networks can be formed, such that the electron transport occurs in acceptor molecular network and the hole transport in donor polymer network [5].

The possibility of relatively defect-free semiconductor polymer-insulator interface led to the improvement in the field effect transport devices. A model polymer system, which has been used to study field effect transport properties are the regioregular polyalkylthiophenes. A major breakthrough [6] was the demonstration of a field effect transistor with a higher charge carrier mobility, of  $0.045 \text{ cm}^2/\text{V}\cdot\text{s}$ , based on solution-cast region-regular poly (3-hexylthiophene) (RR-P3HT) on treated  $\text{SiO}_2$  substrates. An integrated optoelectronic all polymer device consisting of polymer FET and other polymer LED was demonstrated as a single pixel [7]. The high charge carrier mobility in thiophene based polymer is ascribed to the self-ordering properties, resulting in nanometer-sized lamellae. The two-dimensional nature of charge transport [8,9] within these lamellae was investigated using various spectroscopic and structural information. The performance of FETs based on ordered polymer system has shown gradual improvements, with recent reports of mobility as high as  $0.2 \text{ cm}^2/\text{V}\cdot\text{s}$  [10]. These improvements were possible by a combination of breakthroughs in synthesis procedures to obtain stable polymers, modification of process conditions, and engineering surfaces to promote ordered film growth on insulating surfaces.

Continuous improvement in the device efficiencies have been made in academic and industrial research laboratories over the last 15 years, after the initial breakthroughs. These improvements were made possible by rigorous understanding of different issues pertaining to the material synthesis, photophysics, transport, interfacial processes, and

device physics associated with these systems. Efforts related to engineering, product design, packaging, have resulted in commercial products from leading consumer electronics establishments. The initial OLEDs have progressed rapidly and led to first commercial consumer electronic products incorporating OLED displays. By exciting a fluorescent conjugated polymer in a microcavity using high laser intensities, optically driven laser activity was shown in 1996 [11]. This is a pre-requisite for developing electrically driven stimulated electroluminescence diode lasers based on conjugated polymers. The progress was not only restricted to case of OLEDs but also towards organic field effect transistors (OFETs) based logic circuits [12, 13], Light emitting FETs [14], organic photovoltaic cells [15] and memory device [16]. These devices have found successful application in the area of radio frequency identification (RFID) tags [17], smart cards [18], sensors [19] etc.

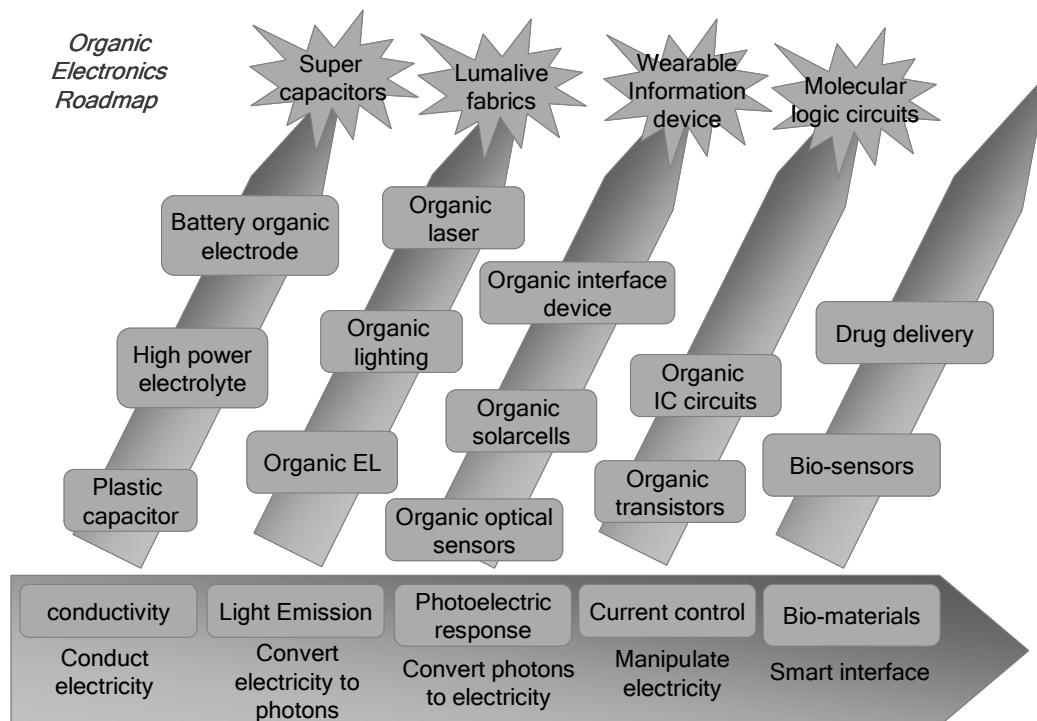


**Figure 1.1** Chart to depict properties and applications

The organic electronics roadmap charting the progress made in the temporal plane has been presented in *Figure 1.1*. A vivid image regarding the evolution of the field in terms of phenomena and its applications can be gathered by studying the map. As shown in *Figure 1.1*, the horizontal axis indicates the properties (conductivity in 1970s [1, 2], polymer electroluminescence in 1990s [3], photoelectric in 1992 [4], current control devices in 1988 [20]) findings in organic electronics over a period of time and the vertical axis shows the present and future potential in various domains.

The stages from design of materials to final device product have realized in less time as compare to other existing technologies, makes polymer electronics more fascinating. However, numerous factors come into play to achieve the final goals. Some of which includes; inherent limitations and restrictions from the materials point of view such as efficiencies, speed and stability. Competing technologies, environmental factors and economics are other factors, which are extraneous in nature. Progress in this field has to followed the advances in our understanding of the fundamental transport properties of conjugated polymer materials. The underlying science is tremendously exciting owing the weak intermolecular interactions, low dielectric constants and the presence of disorder in the semiconducting polymer systems that make them distinctively different and unique systems, for exploring a wide variety of solid-state phenomena.

It is possible to use existing polymer processing techniques such as offset printing, ink-jet printing, vacuum deposition systems, gravure printing, flexographic printing, roll-to-roll printing, patterning, and inline manufacturing for electronically active functional polymer system. These processing options do not exist for inorganic semiconductor technology. These techniques are quite mature at well developed industrial scale and ready to produce a range of products, currently in the pipeline of the organic-electronics industries. On the other hand, new techniques have been explored to make these inherently disordered materials in to an order using either physical templates [21] or chemical treatments of substrates [22].

The properties of conjugated polymer system have an apparent similarity to amorphous Si (a: Si). However, these are not equivalent in terms of microscopic charge



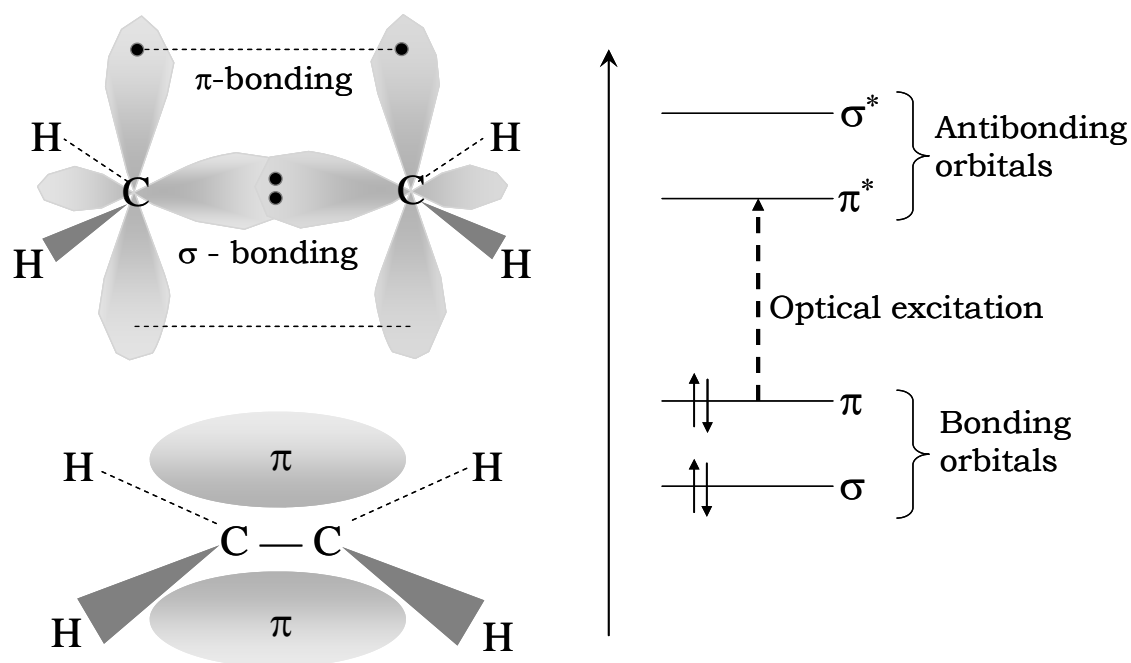
transport mechanisms. Recent observations of the field effect mobility in organic semiconducting materials are comparable to that of amorphous Si [23]. The possibility of tuning the molecules facilitates the engineering of molecular assembly to tailor the electrical transport requirements. The speed and performance of such printed devices is not comparable to devices manufactured in the traditional silicon industry; but the cost for each device is very nominal. This along with the fact, that tedious silicon processing is more elaborate unlike easy processable polymers, makes organic electronics even more interesting. One of the goals in polymer semiconductors is to achieve carrier mobility as high as possible. Measurements on single-crystal organics [24] and theoretical estimates suggest an upper limit on the mobility of about  $10 \text{ cm}^2\text{V}^{-1}\text{s}^{-1}$ . The practical upper limit is unknown, but the obvious approach is to continue removing the sources of disorder, as they are identified. This is possible to achieve by better control over the molecular structure and film morphology. The present mobility of  $0.2 \text{ cm}^2\text{V}^{-1}\text{s}^{-1}$  is already enough for their use in displays and solar cells. A mobility of  $>1 \text{ cm}^2\text{V}^{-1}\text{s}^{-1}$  would exceed the technology benchmark for thin-film semiconductors — a:Si. However, it must be said that there is more to a successful electronic device technology than mobility alone. Hence, predictions of an electronic technology revolution must be treated with due care.

However, low charge mobility compared to single crystalline Si, and other identifying characteristics, limit the range of applications envisioned for organics. Organic semiconductors are not meant to replace traditional Si electronics, but rather to complement it and extend its capabilities. The following sections provide a background to the central theme of the thesis. A variety of concepts and approaches existing in the field is presented. These sections do not form a complete survey and is restricted to subjects relevant to the thesis.

## Materials Overview

There are two major classes of organic semiconductors: low molecular weight molecular solids and conjugated polymers. Both have in common a conjugated  $\pi$ -electron system being formed by the  $p_z$ - orbitals of  $sp^2$  – hybridized C- atoms in the molecule.(see *Figure*

1.2). As compared to the sigma-bonds forming the backbone of the molecules, the  $\pi$ -bonding is significantly weaker.

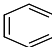
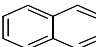
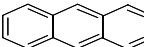
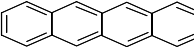
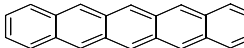


**Figure 1.2** Left:  $\sigma$ - and  $\pi$ - bonds in ethane, as an example for the simplest conjugated  $\pi$ - electron system. The right viewgraph shows the energy levels of a  $\pi$ - conjugated molecule. The lowest excitation is between the bonding  $\pi$ -orbital and anti-bonding  $\pi^*$ -orbital (adopted from [25])

Therefore, the lowest electronic excitations of conjugated molecules are  $\pi$ - $\pi^*$  transitions with an energy gap typically between 1.5 eV to 3.0 eV leading to light absorption and emission in the visible spectral range. As shown in **Table 1.1**, for the family of Polyacenes the energy gap can be controlled by restricting the degree of conjugation in a molecule. Thus, chemistry offers a wide range of possibilities to tune the optoelectronic properties of organic molecular semiconducting materials. In similar fashion, one can synthesize polymers with variable conjugation lengths to tune the band gap and with the advantage of its solubility, in different organic solvents. [26]

An important difference between the two classes of materials is the way, they are processed to form thin films Small molecules are usually deposited from the gas phase by sublimation or evaporation, whereas conjugated polymers are processed from the solution

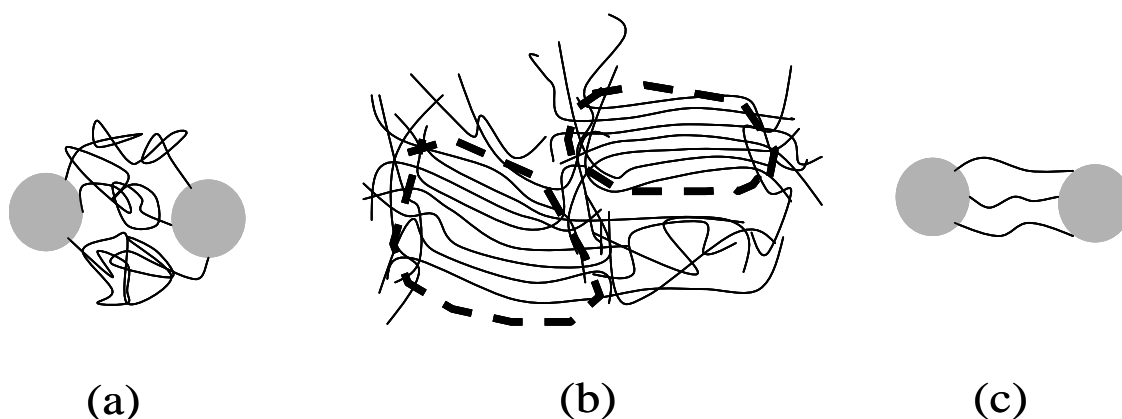
**Table 1.1** Molecular structure of the first five polyacenes, together with the wavelength of main absorption peak (adopted from [27])

Molecule	Structure	Absorption Maximum
Benzene		255 nm
Naphthalene		315 nm
Anthracene		380 nm
Tetracene		480 nm
Pentacene		580 nm

e.g. drop casting, spin coating, dip coating, printing techniques as per the requirement. The controlled growth of highly ordered thin films, by either vacuum deposition or solution processing, is still a subject of ongoing research. This is very crucial to improve the device performance and will be discussed in detail in Chapter 2. As the structure has a strong impact on the functional properties, understanding the structure formation, i.e., the growth process, and finding methodologies to optimize the structural definition is a prerequisite for technological progress. Understanding the science of the growth process itself provides several fundamental challenges. The semiconducting polymers (see in **Table 1.2**) which were used to carry out this thesis work are (i) Poly(2-methoxy-5-(2-ethylhexyloxy)-1,4-phenylene vinylene) (MEHPPV), (ii) Poly(3-hexylthiophene) (P3HT) and (iii) Poly(9,9-dioctylfluorene-alt-bithiophene) (PFO – TT). These are three model polymer systems, extensively used for organic electronics and optoelectronic devices due to their specific material characteristics. While working with these polymers specific issues involving the morphology of individual chains (e.g. twisting and bending of the chain backbone), need special consideration. Another key and almost ubiquitous feature

of electronic polymers is the important role of inter-chain interactions, which strongly depend on the nano-scale variations of local order in the system.

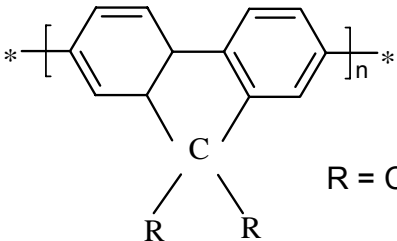
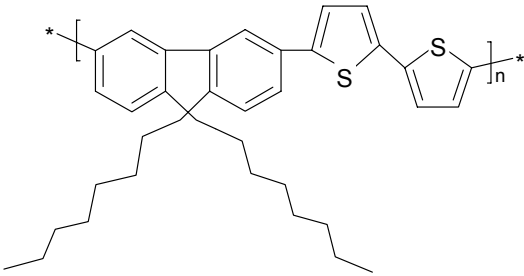
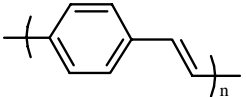
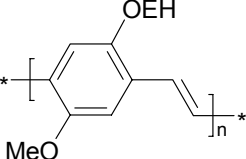
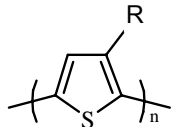
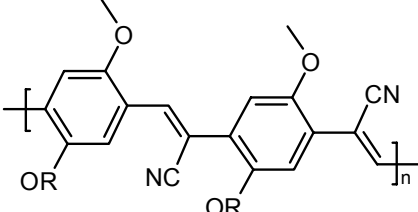
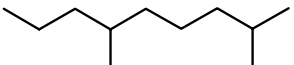
Extensive structural studies of polymers have led to the development of ordered structures in disordered polymer films, where the chains are relatively well packed and nearly crystalline and in regions between these crystalline-like portions, the interchain correlation are of very short range. Further, as indicated in *Figure 2.3*, the disordered regions could be coil-like or rod-like. The local morphology is very sensitive to the preparation of the materials and the means by which films are prepared.



**Figure 1.3** Polymer chain conformations (a) coil- like (b) order chains domain and (c) rigid backbone rod- like, in a solid polymer film

Hence, materials of the same composition may have very different electronic properties depending on the solvents used and the means of preparing the films like annealing conditions, deposition techniques etc. The transport length-scale dependence on processing conditions and implications of the control of the structural order on the photo-physics and device-physics of the semiconducting polymers has been discussed in detail in Chapter 3. The structurally induced charge transport in polymer films will be discussed in a variety of conjugated polymers. It was found that nano-scale variations in local order control much of the physical phenomena in these materials.

**Table 1.2** Semiconducting polymers: chemical structures, energy levels and IUPAC name (adopted from [28])

Chemical Structure	Physical Properties	IUPAC name
 <p style="text-align: center;"><math>R = C_8H_{17}</math></p>	HOMO 2.4 LUMO 5.7	Poly(9,9-dioctylfluorene) (PFO)
	HOMO 3.1 LUMO 5.5	Poly(9,9-dioctylfluorene- <i>alt</i> -bithiophene) (PFO-TT or PF8T2)
	HOMO 2.7 LUMO 5.2	Poly(para-phenylene vinylene) (PPV)
	HOMO 2.8 LUMO 5.0	Poly(2-methoxy-5-(2-ethylhexyloxy)-1,4-phenylene vinylene) (MEHPPV)
 <p style="text-align: center;"><math>R = C_6H_{13}</math></p>	HOMO 2.7 LUMO 4.9	Poly(3-hexylthiophene) (P3HT)
 <p style="text-align: center;"><math>R =</math> </p>	HOMO 3.2 LUMO 5.4	Poly(2,5-dihexoxy- $\alpha$ , $\alpha'$ -dicyno- <i>p</i> -xylylidene- <i>alt</i> -2,5-dihexoxy- <i>p</i> -xylylidene) (CN-PPV)

## Quasiparticles as Charge Carriers

Charge carriers in conjugated polymer have been interpreted in terms of self-localized excitations, which are quasi-particles with structural deformation over several repeating units. These excitations can be classified mainly into *solitons* [29], *polareons* [30] and *bipolarons* [31], which directly contribute to charge transport in different cases according to the chemical and physical properties of the doped or undoped polymeric materials. In this thesis, *polareons* and *bipolarons* have been explored as the charge carrier species in the polymer systems. These positive and negative characters of charge carriers have been denoted as holes and electrons, respectively.

### Polareons

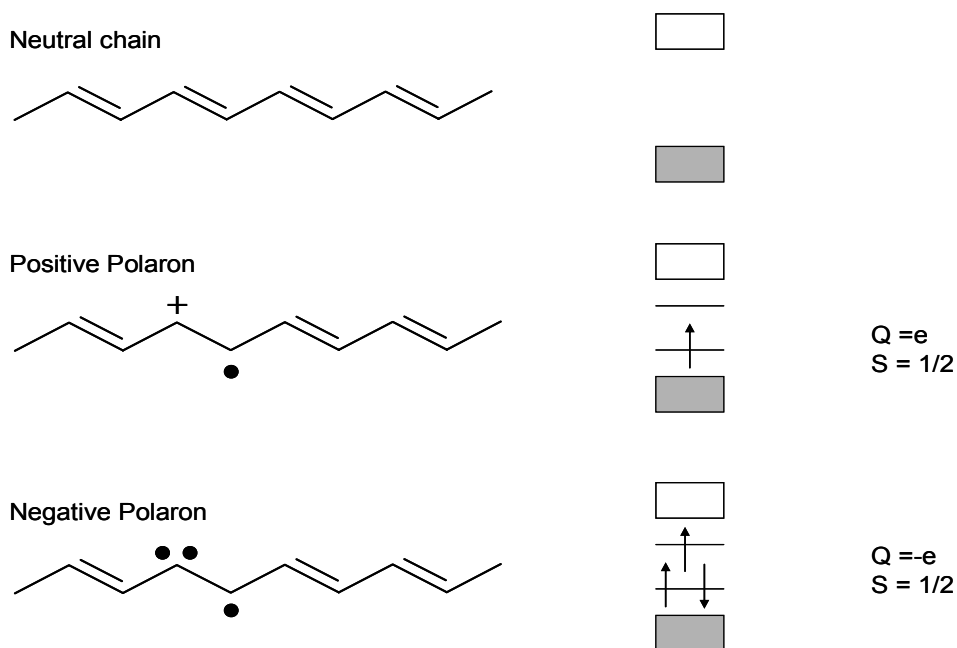


**Figure 1.4** Various types of polareons with their spin and charge states, gray and white box represent filled and empty level, respectively [32].

Upon doping the polymer, the excess isolated electron or hole is self-trapped within ~100 femto-seconds by the deformation, induced in the chain to enable a lower energy level [30]. The deformation under the influence of charge carrier, results in the formation of

*polaron*, which contributes to hopping transport in non-degenerated and degenerated conjugated polymers. A polaron can travel along the polymer chain without changing its shape and represents localized solitary waves. The strong electron-phonon coupling is responsible for the formation of polarons in conjugated system. The polaron has either a smaller radius or a larger radius depending upon the strength of the electron-phonon coupling. These quasi-particles are classified as positive polaron and negative polaron according to the nature of charge carrier involved and typically consist of single-charged and  $\frac{1}{2}$  spin states. The two additional energy levels that are located symmetrically at the centre of the gap can identify the existence of polaron. The relative location of the energy levels with respect to HOMO and LUMO depends on the chain length. The energy states show, definite parity (even or odd) under the consideration that the conjugated system preserves inversion symmetry, even when the side groups would tend to violate it. The transitions among the levels are governed by the selection rules, which require parity transformation between the concerned levels.

### Bipolarons

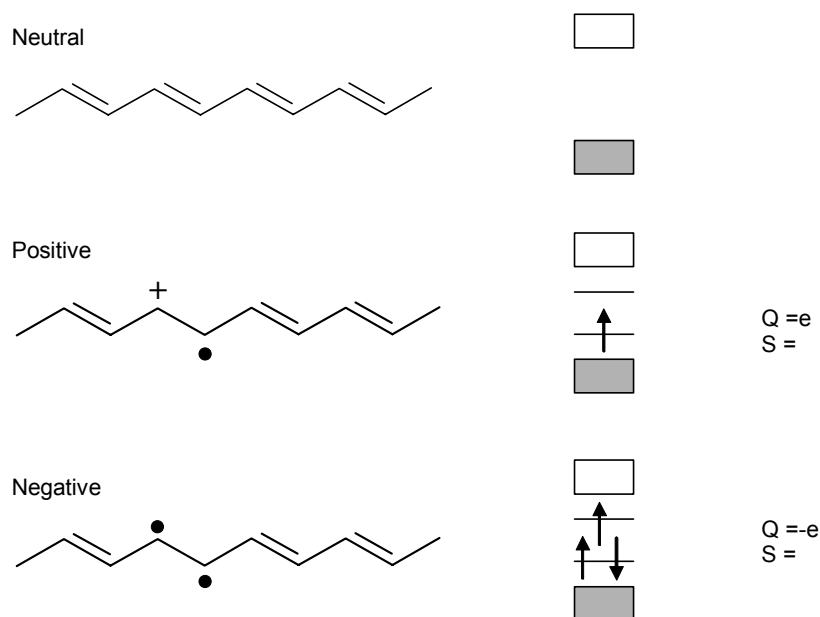


**Figure 1.5** Various types of polarons with their spin and charge state, gray and white box represent filled and empty level, respectively [32].

In doped non-degenerated ground state polymer, it is observed that there is an increase in conductivity by orders of magnitude without any appreciable change in magnetic susceptibility while doping. Since in this case, possibility of soliton formation is improbable, the concept of new quasi-particle, called *bipolaron*, with double charge but no spin, has been introduced. Two like charges with opposite spins bind together in the same conjugation length to form a bipolaron. The repulsion between the two like charges under consideration and the entropic term must be compensated by the influence of nearby oppositely charged ions that donated the charges to the chain in order to stabilize the bipolaron. The existence of bipolarons of either positive or negative charge introduces two subgap energy levels similar to polarons. However, the stability of a bipolaron strongly depends on the temperature and the concentration of charge carriers. Low charge concentration or higher temperature increases configurational entropy that promotes a dissociation of a bipolaron into two polarons. Photoinduced absorption, chemical doping, charge modulation spectroscopy etc. have been adopted successfully, to detect the existence of bipolarons in several non-degenerated ground state polymers.

## **Electrical Transport in Organic Semiconductors**

Charge-carrier transport phenomena in disordered organic solids have been the subject of intensive research for many years, largely stimulated by the use of these materials in electro-photographic receptors, organic light-emitting devices, organic solar cells, thin-film transistors, etc. Many recent studies of a wide range of molecularly doped polymers ~MDP's and conjugated main chain- and pendant-group polymers, as well as vapor-deposited molecular glasses, have been described, within the framework of the Gaussian disorder model of Bassler [33, 34]. The model is premised, on the argument that charge-carrier transport occurs by hopping through a Gaussian density of transport states ~DOS of energetic widths. Later, Gartstein and Conwell [35] suggested that the spatial correlation of the energies of transport sites in disordered media must be taken into account in order to properly describe the field dependence of mobility over the broad field range. The outline of conceptual approaches for charge carriers hopping in these



non-crystalline organic materials has been discussed in brief in order to understand the experimental results described in Chapter 3.

### **The Continuous Time Random Walk (CTRW) Formalism**

Lax, Montroll and Scher [36, 37, 38] proposed a milestone in understanding the charge transport in an amorphous network, in terms of continuous time random walk. It is based on the idea that one can interpret the effect of disorder in a material by formally replacing the conventional exponential waiting time distribution of waiting times, of a crystalline semiconductor by an algebraic distribution of waiting times of the form,  $\psi(t) \sim t^{-(1+a)}$ , with  $0 < a < 1$  being a dispersion parameter, while retaining the crystal structure of the sample. This shows, a hierarchy of sites regarding their ability to transfer a charge carrier to an adjacent site. Thus, opening faster and slower routes for charge transport and this formalism was able to explain the phenomenon of transit time dispersion of the TOF measurements. The approach was heuristic in the sense that the origin of the algebraic waiting time distribution remained unspecified. However, later it was found that in the case of multiple trapping model the dispersion parameter,  $a = T/T_0$  (where  $kT_0$  is the characteristic energy of trap states) is a concrete example of the CTRW formalism. This affords an interpretation of experimental transport data for hydrogenated a:Si and chalcogenide like systems, in which the density of states distribution is exponential.

### **The Gill Equation**

The CTRW approach has also been applied to charge transport in molecularly doped polymers because of similar dispersive transport observation [39], which was a direct feature of the positional disorder of transport sites. This issue initiated some controversy as it was argued that the variation of the jump distances could hardly explain the magnitude of the observed effects [40]. Another argument against the notion that positional disorder alone controls the transport was the measurement of the charge carrier

mobility as a function of temperature and electric field. The studies on a broad class of polymer [41, 42] revealed, (i) activated behavior of charge carrier mobility yielding an activation energy of 0.4 – 0.6 eV, independent of chemical constitution and synthesis, if analyzed in terms of Arrhenius equation. (ii) a field dependence of the mobility resembling the Poole-Frenkel law,  $\ln\mu \sim SE^{1/2}$ , over an extended range of electric fields [43] and (iii) a deviation of both magnitude and a reversal of sign of S above a certain temperature [44]. A famous equation proposed by Gill [45] explains this terminology

$$\mu(F, T) = \mu_0 \exp\left(-\frac{\Delta_0 - \beta F^{1/2}}{kT_{eff}}\right), \frac{1}{T_{eff}} = \frac{1}{T} - \frac{1}{T^*} \quad (1.1)$$

where  $T^*$  is the temperature at which extrapolations of the  $\log \mu$  versus  $1/T$  lines intersect. This equation was just a fitting to experimental data with no theoretical foundation. There were few serious issues in implementing this equation, like; (i) assumption behind an original form of the Poole-Frenkel effect, implies that transport is trap limited and charged when empty. (ii) it fails to account, for the transition to dispersive transport at lower temperatures.

### The Hopping Approach

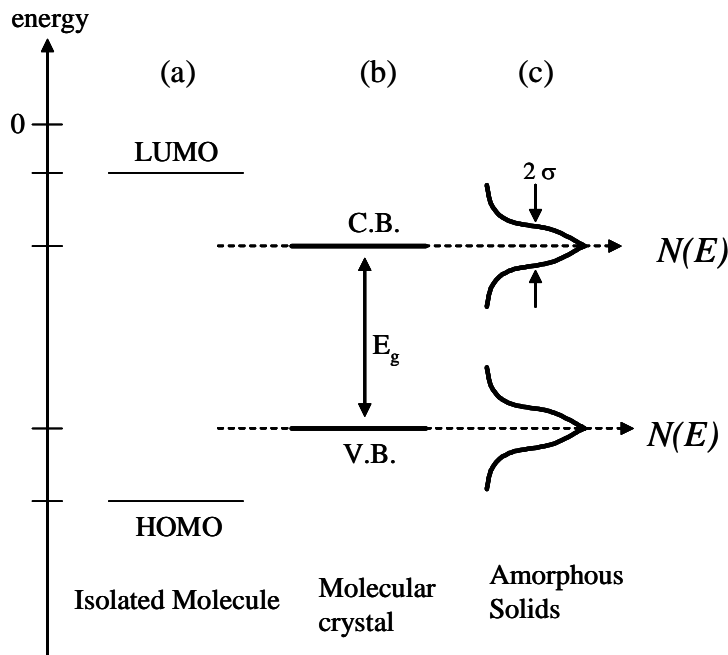


**Figure 1.6** Energy levels of (a) an isolated molecule, (b) a molecular crystal and (c) an amorphous solid. The width of the Gaussian DOS in an amorphous solid is typically in the range of  $\sigma = 80$  to  $120$  meV, whereas the bandwidth in molecular crystals is less than  $100$  meV. (figure adopted from [46])

The weak intermolecular coupling in molecular crystals leads to a narrow valence and conduction band, typically 0.1 eV or less [27], which results in the mean free path of an order of lattice parameter at 300 K. In molecularly doped polymers, which are inherently disordered. The elementary transport occurs due to charge transfer between adjacent transporting sites present in neighboring molecule or segments of main chain of polymer. In chemical terms, this is a redox process involving chemically identical yet physically different moieties. This elementary step depends on temperature and electric field, which decides the charge carrier mobility in these systems. The activation energy for these systems is a combine contribution of inter- and intra-molecular interactions. The former arises from the physical in-equivalence of the hopping sites due to local disorder and latter is due to a change in molecular conformation upon removal or addition of an electron from transport sites. This model assumes that the coupling of the charge carrier to inter- or intra-molecular modes is weak and the activation energy of transport reflects the static energetic disorder of the hopping sites. Bassler et al first time modeled charge transport in these organic solids via Monte – Carlo simulations [35] , which can be idealized for an arbitrary adjustable degree of disorder and devoid of any accidental complexity. The essential input parameter is the width of the distribution of hopping states [DOS]. It is usually assumed to be of Gaussian shape:

$$g(E) = \frac{1}{\sqrt{2\pi}\sigma} \exp\left(-\frac{E^2}{2\sigma^2}\right) \quad (1.2)$$

Because in organic solids optical absorption generates neutral rather than charged excitations, there is no direct experimental evidence of this assumption. However, it is known, that inhomogeneously broadened absorption profiles of molecules embedded in a glassy matrix are of Gaussian shape. The hopping rate for these solids according to Miller and Abrahams is as follows [47]:

$$\nu_{ij} = \nu_0 \exp\left(-2\gamma a \frac{r_{ij}}{a}\right) \exp\left[-\frac{|E_j - E_i| + (E_j - E_i)}{2kT}\right] \quad (1.3)$$

where  $r_{ij}/a$  is the relative jump distance between hopping sites  $i$  and  $j$ ,  $\gamma$  is the coupling matrix element between the sites,  $a$  the mean inter-site distance and  $\nu_0$  the frequency factor (attempt to jump frequency). In a disordered medium the inter-site distance and the coupling among the transport molecules is usually non-spherical, and has a local variation, so the overlap parameter  $2\gamma a = \Gamma$  also has a distribution about a fixed value. This distribution is also referred to as a positional or off-diagonal disorder. Effects of these disorder have been simulated and is well documented in the literature [48, 49]. The essential observations of these approaches are the following:

- (i) Upon starting in a random site within the DOS, a charge carrier tends to relax towards tail states featuring a logarithmic decay law. The diffusivity of particle decreases with time, and gives rise to dispersive transport of charge carriers.
- (ii) The superposition of an external electric field tilts the DOS. Therefore, local activation energy is lowered and the charge carrier mobility increases as a function of EF in the absence of positional disorder. At high electric field, when electrostatic potential overcompensates the energetic disorder, the drift velocity of carrier packet saturates since the transport is largely unidirectional and the asymmetric jump rate reduces mentioned in the Miller-Abrahams model.
- (iii) In the intermediate field range the temperature and field dependences of the charge carrier mobility are predicted to be of Pool-Frenkel type ( $\mu \propto \exp(\sqrt{E})$ ).
- (iv) At weak electric fields, hopping within an intrinsically broadened DOS is equivalent to multiple trapping in a system with a discrete transport level and an energetically disperse distribution of trapping levels [50].
- (v) Under quasi equilibrium conditions, the diffusive spreading of an initially  $\delta$ -shaped sheet of charge carriers drifting across a sample is anomalously large. This is an inherent signature of the disorder induced broadening of the waiting

time distribution. It is accompanied with a field-induced increase of the Einstein  $\mu/D$  ratio whose value in discrete system is  $e/kT$  [51].

## Einstein Relation for Disordered Semiconductors

It is well established that charge transport in disordered semiconductors is not fully characterized by the conventional current continuity equations. In the context of organic semiconductors, it is accepted that the mobility is exponential in the square root of the electric field ( $\mu \propto \exp(\sqrt{E})$ ); however, this modification is also often found to be insufficient. The deviation of the experimental results from the conventional current continuity equations (where Einstein relation  $\rightarrow D/\mu = k_B T$ ) description is typically explained, either in the context of transport under non-equilibrium conditions or with the aid of detailed Monte Carlo simulations of hopping transport. A common feature of these detailed studies is that it does not consider (or even preclude) effects associated with the charge density. One of the quoted indications for the standard continuity equations being incomplete, is the finding that the ratio between the diffusion coefficient of charge carriers and the mobility is larger than the classical Einstein relation of  $kT/q$  (i.e.,  $D/\mu > k_B T$ ). A basic explanation for enhancement of Einstein relation relies on two possible reasons (schematic is shown in *Figure 1.7*)

- (i) the density of states (DOS) is a Gaussian
- (ii) the charge carriers can be described as being at equilibrium conditions (i.e., one can use Fermi–Dirac statistics).

The relation between the diffusion coefficient ( $D$ ) and the mobility ( $\mu$ ) of the low-density limit is given by  $D/\mu = kT/q$  (Einstein relation) where  $k$  is the Boltzmann coefficient,  $q$  is the charge of the particle, and  $T$  is the characteristic temperature. A generalized relation between the diffusion coefficient and the mobility (i.e., generalized Einstein relation) can be derived for a general charge-carrier energy-distribution function, and a general DOS function

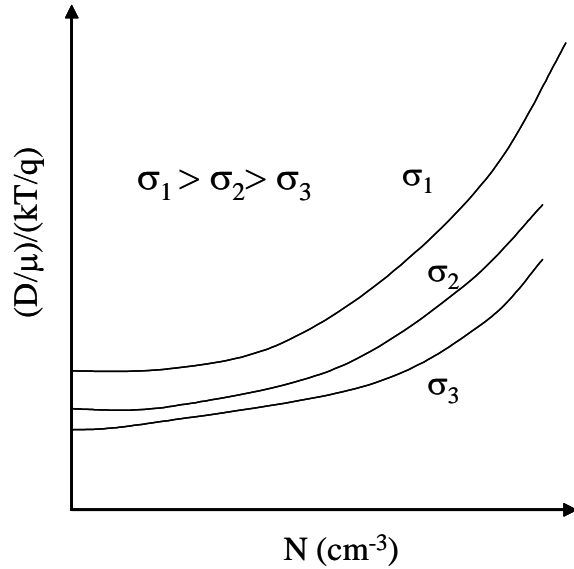


**Figure 1.7** Schematic of enhancement of the Einstein relation, relative to low density limit ( $kT/q$ ), as a function of the filling of the density of states for different Gaussian variance ( $\sigma$ )

$$\frac{D}{\mu} = \frac{P}{q} \frac{\partial P}{\partial E_F} \quad (1.4)$$

where  $P$  is the particle concentration and  $E_F$  is the chemical potential.

The general Einstein relation has been so far derived for high-density (degenerate) crystalline semiconductors or degenerate semiconductors, having a band tail, i.e., a distribution of states in the forbidden gap. The generalized Einstein relation is calculated for a Gaussian density of states (NOT a tail), as is often assumed in the case of organic semiconductors and a few other amorphous semiconductors. **Eq 1.5** gives the functional form of a Gaussian DOS

$$DOS(E) = \frac{N_V}{\sqrt{2\pi} \cdot \sigma} \exp \left[ - \left( \frac{E - E_0}{\sqrt{2\pi} \cdot \sigma} \right)^2 \right] \quad (1.5)$$

where  $E$  is the energy,  $E_0$  is Gaussian centre,  $N_V$  is the effective DOS and  $\sigma$  is width of the DOS. The spatial distribution function could be either homogeneous (which describes uniform spatial distribution) or slightly different (to account for the specific morphology).

For the sake of simplicity, a typical interstates distance is considered to be  $r_{typ} = \sqrt[3]{N_V^{-1}}$ .

Issues relating to long range energetic correlation [52, 53] and morphological effects are

not discussed here. For the system being in equilibrium state of the system charge energy-distribution function can be described as

$$p(E) = DOS(E)f(E) \quad (1.6)$$

or the total density ( $P$ ) as

$$P = \int_{-\infty}^{\infty} p(E)dE = \int_{-\infty}^{\infty} DOS(E)f(E)dE \quad (1.7)$$

where  $f(E)$  is Fermi-Dirac distribution function, therefore

$$\frac{D}{\mu} = \frac{kT}{q} \frac{\int_{-\infty}^{\infty} \exp\left[-\left(\frac{E-E_0}{\sqrt{2}\sigma}\right)^2\right] \frac{1}{1 + \exp\left(\frac{E-E_F}{kT}\right)} dE}{\int_{-\infty}^{\infty} \exp\left[-\left(\frac{E-E_0}{\sqrt{2}\sigma}\right)^2\right] \frac{\exp\left(\frac{E-E_F}{kT}\right)}{\left[1 + \exp\left(\frac{E-E_F}{kT}\right)\right]^2} dE} \quad (1.8)$$

When the major part of the charge energy distribution is far from the chemical potential (i.e., the Fermi-Dirac distribution can be approximated by a Boltzmann distribution), the generalized Einstein relation approaches the classical value ( $D/\mu = kT/q$ ). This non-degeneracy condition is applicable when the Gaussian variance ( $\sigma$ ) is small and the chemical potential is at distance more than  $5 kT$  from the Gaussian center  $E_0$ .

A more realistic Gaussian variance to describe organic semiconductors is in the order of 80–120 meV ( $\sigma = 3-6$  at room temperature). In such a case, the charge concentration peak remains near the chemical potential even when it is  $20 kT$  below the center of the Gaussian,  $E_0$ . This implies that an amorphous organic semiconductor always degenerates down to very low charge concentration, and, the classical Einstein relation is not expected to hold, under any realistic condition. Therefore, the generalized Einstein relation has to be calculated in full form.

## Interfaces

It is found that the performance of organic optoelectronic devices depends significantly on the properties of the interfaces such as electronic structure and morphological aspects of interfaces. This feature can be exploited to improve the characteristics of a device. A well known example is the incorporation of charge-transporting and charge-blocking layers in LEDs. The role of morphology is especially significant when there is more than one active organic component, i.e., in a composite active layer. (Interfaces can be major factor within a one component system too, e.g., the influence of grain boundaries on charge transport or on propagation of light). A prime example of a composite system is the photovoltaic material based on the donor-acceptor concept. The major issues here are the interface area and the continuity of the different components.

The microstructure of an organic-based optoelectronic device is mostly realized through a series of processing steps, each of which can be engineered to optimize performance. In case of polymer, it have been found that the microstructure of the polymer layer depends strongly on the processing history. This is due to the non-equilibrium and metastable character of polymer solids. This aspect needs careful consideration. One can use an entirely different approach to obtain a desired microstructure for a specific purpose, using self-organization properties of cleverly designed molecules.

### Organic-Metal Interfaces

In electronic devices, electronic signal or electric power should be exchanged between a device and an external circuit; charge carriers must move across the interface between the device and the electrode attached to it. Thus, the understanding of the interface between an organic semiconductor and the electrode is a key issue for organic devices.



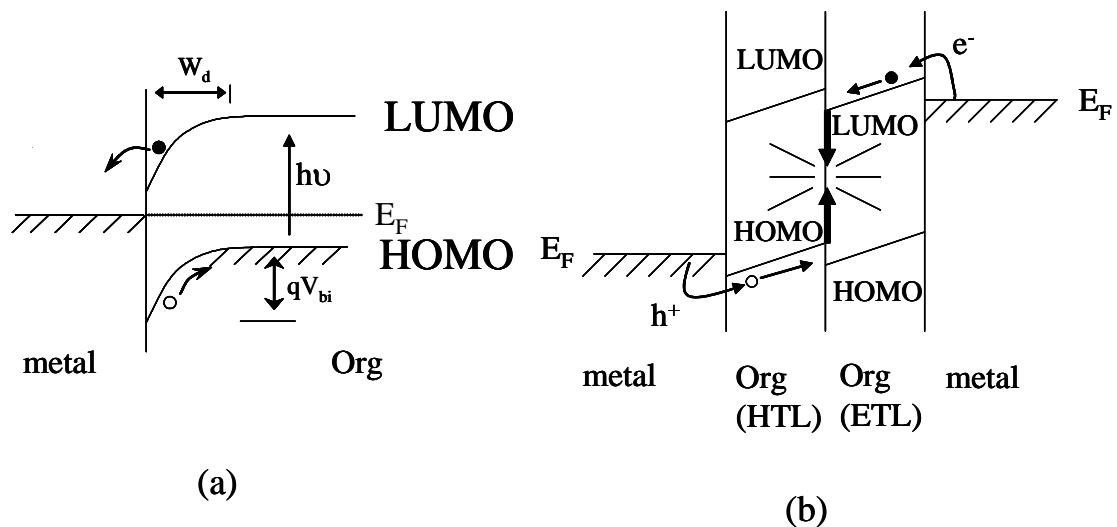


**Figure 1.8** Conventionally used energy diagrams of organic devices. (a) Organic solar cells (b) Organic electroluminescent (EL) devices.

For example, in organic electroluminescent (EL) devices, electrons and holes are injected from the cathode and anode, respectively. The related processes have been shown in **Figure 1.8b** using a conventional energy diagram. The lowering of the barrier height for carrier injection at organic – metal interfaces is crucial for the performance of device. The influence of interfaces is not only limited at the interface, but the properties of bulk semiconductor are affected in the region near the interface. For example, in photovoltaic (PV) cells, the space charge layer with band bending plays decisive role in the performance of the device as shown in **Figure 1.8a**. The gradient of potential curve in the space charge layer is important for the efficiency of the separation of electron – hole generated by photon absorption. Thus, the answer to following question “how do the energy levels of an organic solid and a metal align at their interface?” is a key in the interface business. A simple model assuming a common vacuum level at the organic – metal interface had been applied to estimate the interfacial electronic structure of organic devices. The traditional model is in analogy to the Mott – Schottky model, which is widely used in inorganic semiconductor – metal interfaces. Its validity to organic system is still under research. S. Narioka et al has shown in 1995 [54], the energy level alignment problem of organic – semiconductor/ metal interface, where the invalidity of the assumption of a common vacuum level was clearly demonstrated by the results of

ultraviolet photoemission spectroscopy. The studies on various organic solids revealed that the model is not valid for most organic – metal interfaces [55, 56]. The invalidity of the assumption implies that the vacuum level does not align but shifts at organic – metal interfaces. These studies covered not only the energy level alignment problem but also other important factors such as the structures and reactivity of organic – metal interfaces. Material science of organics and further progress in the basic understanding of the above-mentioned factors are highly desired for the development of organic devices. The work function of metal and position of HOMO – LUMO level of organic- semiconductor primarily decides the ohmic or Schottky character, which has been discussed in the following section.

### (a) Ohmic Interface

The charge injection properties of a metal/semiconductor contact can be discussed in terms of the energy barrier at the interface, the carrier mobility of organic semiconductor, its carrier density (doping level), the presence of mobile ions, and the sample geometry. A review article by G. G. Malliaras et al on organic/metal ohmic interface has been used to explain physical processes at Ohmic interface [57].

Let us consider the simple case of a metal electrode injecting electrons in trap-free semiconductor. There is a limit for injecting the electrons in semiconductor, depicted as a solid line in *Figure 1.9*. At lower voltages (and neglecting diffusion), the motion of free electrons present in semiconductor determines the current and the current density is given by Ohm's law, **Eq. 1.9**

$$J_{OHM} = eN_0\mu \frac{V}{L} \quad (1.9)$$

where  $e$  is the charge of an electron,  $N_0$  is the number of free electrons per unit volume,  $\mu$  is their mobility,  $V$  is applied voltage and  $L$  is the sample length.

As the voltage increases, electrons injected from the contact begin to outnumber the ones that are initially present inside the semiconductor. This occurs when the number

of electrons becomes approximately equal to  $C \times V$ , where  $C$  is the capacitance of the sample. This is the space charge limited (SCL) regime, where the current density is given by the Mott-Gurney law [58], **Eq. 1.10**

$$J_{SCL} = \left(\frac{9}{8}\right) \epsilon \epsilon_0 \mu \frac{V^2}{L^3} \quad (1.10)$$

where  $\epsilon \epsilon_0$  is the dielectric constant. Eq. 1.11 gives the threshold voltage  $V_0$  at which the current turns from ohmic to SCL by equating the two currents

$$V_0 = \left(\frac{8}{9}\right) \epsilon N_0 \frac{L^2}{\epsilon \epsilon_0} \quad (1.11)$$

The above discussion assumes that the injecting contact does not pose any limitation in the flow of current through the semiconductor. Therefore, the solid line in **Figure 1.9** represents the density of the bulk limited current,  $J_{\text{bulk}}$ , which is either ohmic or SCL current in this example. However, in many cases, the contact ends up limiting the amount of current that flows through the sample. The dashed line in **Figure 1.9** depicts the result. The current is now smaller in magnitude than that of the bulk limited current and it is called as an injection-limited current,  $J_{\text{inj}}$ , its functional dependence is unknown as it depends on the mechanism of injection. A figure of merit for contact performance is the injection efficiency, defined by Eq. 1.12

$$\eta = \frac{J_{\text{INJ}}}{J_{\text{BULK}}} \quad (1.12)$$

There are two different regimes for carrying out injection efficiency measurements. In the first regime,  $V_0$  is small and the bulk limited current is space charge limited current; (see **Eq. 1.10**) this regime is relevant to the contacts in OLEDs, where the organic layer is depleted (charge density of the order of  $10^{13} \text{ cm}^{-3}$ ) and the sample length is of the order of 100 nm. In such cases,  $V_0$ , ( $\sim \text{mV}$ ) is much smaller than the typical driving voltage for an OLEDs ( $\sim \text{V}$ ). In the second regime,  $V_0$  is large and, it is the ohmic current, as shown in **Eq. 1.9**, that represents the bulk limited current. This regime is relevant to contacts in OTFTs, where the distance between the source and drain electrodes is  $\sim 10 - 100 \mu\text{m}$  and the organic layer is doped by the field effect.

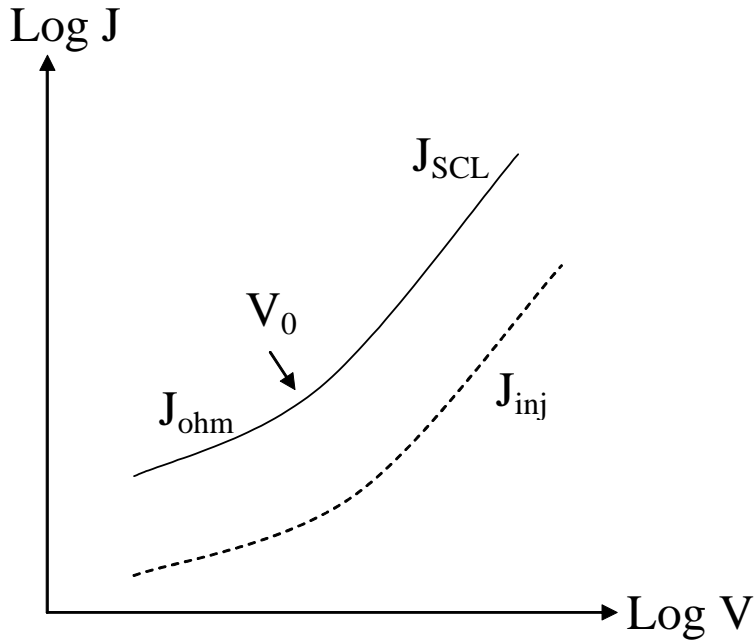


**Figure 1.9** Bulk limited (solid line) and injection limited (dash line) current density versus voltage characteristics for a trap free semiconductor. The threshold voltage  $V_0$  at which bulk limited current becomes space charge limited current, is indicated. Adopted from [57]

### (b) Schottky Interface

The Mott – Schottky model is a well known textbook model for inorganic semiconductor/metal contact. **Figure 1.10** illustrates this model for an n-type semiconductor. When a metal solid and semiconducting solid are isolated, the vacuum level (VL), at infinite distance away from surface of metal & semiconductor, is a common energy level for both solids. When the two solids come in contact, the model, two assumptions are made. The first assumption is that the VLs of semiconductor and metal coincide (VL alignment). According to this assumption, the barrier height for hole (or electron) injection,  $\phi_{Bp}$  ( $\phi_{Bn}$ ) is determined as follows

$$\begin{aligned}\Phi_B^p &= I - \Phi_m \\ \Phi_B^n &= \Phi_m - \chi = \Phi_m - (I - E_g) = E_g - \Phi_B^p\end{aligned}\quad (1.13)$$

where  $I$ ,  $\chi$  and  $E_g$  are ionization potential, electron affinity and energy gap of a semiconductor, respectively. The assumption of VL alignment is often invalid for inorganic – metal interfaces, where some interface states exist. On the other hand, this assumption has been widely used to find injection barrier heights for organic devices. This is probably due to two reasons. Firstly, weak interaction at organic – metal

interfaces can be expected from the Van-der Waals nature of organic solids. Secondly, the VLs of a metal and an organic solid are believed to be a good, common energy reference between the two solids. However, the VL at infinite distance from the surface is not adequate for the definition of work function.

The second assumption is the Fermi level alignment of two solids with band bending. In most cases, the work function is different between a semiconductor and a metal and there is an offset of the Fermi level, which corresponds to chemical potential of this situation. Thus, if the electron (and hole) can be exchanged across the interface, the total system should go to the thermodynamic state with the alignment of Fermi level between the two solids. In such a redistribution of the charges, the potential distribution at the interfacial region is governed by the Poisson equation, which expresses the relation between the charge and potential distributions. As a result, a diffusion layer with band bending is formed that aligns the Fermi energies of the two solids, with a built-in potential  $V_{bi}$  in the organic layer. In the Mott – Schottky model  $V_{bi}$  in the space charge region or the diffusion layer, corresponds to the difference of work-functions between a metal and a semiconductor, i.e.,  $V_{bi} = \Phi_m - \Phi_s$ . The above model is very simple one, as common VL alignment is not achieved at most organic – metal interfaces. The observed experimental results show deviation from the expected model results. This shift is called vacuum shift,  $\Delta$ . The shift is actually hypothetical; the concept of vacuum level shift does not make any sense at the interface, as there is no vacuum space where a VL is defined. In this sense, an interfacial VL is a virtual concept for conveniently discussing the energetic of the interfaces. When we consider  $\Delta$ , the barrier height can be expressed as  $\Phi_m - \Phi_s + \Delta$ . The existence of  $\Delta$  also affects the behavior of band bending, where  $V_{bi}$  can be expressed as  $\Phi_m + \Delta - \Phi_s$ . Thus, the understanding of energy level alignment, especially the VL shift, is crucial for estimating and controlling the interfaces of organic devices.

$$\Phi_B^p = I - (\Phi_m + \Delta) \quad (1.14)$$

$$\Phi_B^n = \Phi_m + \Delta - \chi = \Phi_m + \Delta - (I - E_g) = E_g - \Phi_B^p \quad (1.15)$$

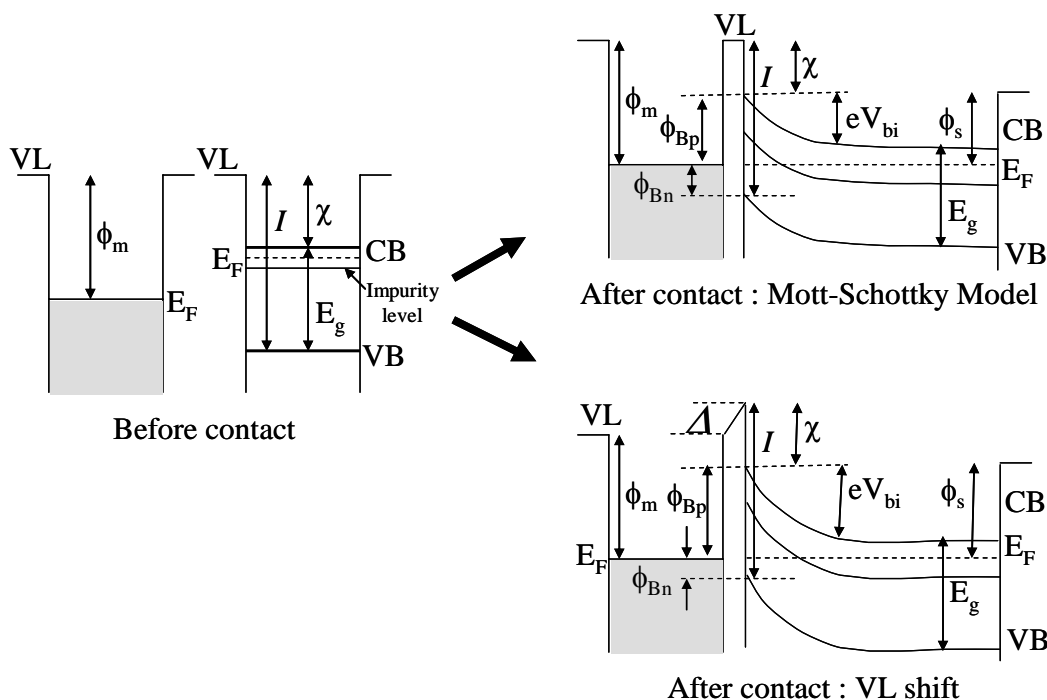


**Figure 1.10** Energy level alignment models at semiconductor- metal interfaces. Top: Mott-Schottky model. Bottom: the case with vacuum level shift. The energy levels are bent by charge redistribution in the semiconductor to achieve the electrical equilibrium with the alignment of Fermi levels of the two solids. This leads to buildup of built-in-potential,  $V_{bi}$ , within a space charge layer.

## Organic- Organic Interface

A novel concept based on interpenetrating blends of donors and acceptors sandwiched between two asymmetrical contacts (two metals with different work functions), has been proposed for photovoltaic devices (photo detectors and solar cells). When the donor molecule is optically excited, a valence electron is promoted to the lowest unoccupied molecular orbital (LUMO) accompanied with a slight relaxation of the molecular structure, and a bound electron – hole pair or “exciton” is created (**Figure 1.IIA**). The presence of acceptor facilitates dissociation of the exciton into free charge

carriers by allowing the promoted electron to lower its energy by transferring it to the LUMO of the acceptor (*Figure 1.11B*). Under the influence of the built-in-field caused by the asymmetrical contacts, separation of the opposite charges takes place with the holes being transported in the donor phase and electrons in the acceptor phase. In this way, an interpenetrating blend can be considered as a network of donor – acceptor hetero-junctions that allows efficient exciton dissociation and balanced bipolar transport throughout the volume. The performance of this type of device is very sensitive to the morphology of the blend as exciton dissociation occurs only at the donor – acceptor interface. To ensure efficient exciton dissociation, an acceptor species should be within the exciton diffusion range, from any donor species and vice versa. To put differently, the characteristic sizes of the channels of the phases should be matched to this diffusion range.

Moreover, both the donor and acceptor phases should form a continuous network to allow bipolar charge transport. Since the exciton diffusion range is typically about 10 nm and hence shorter than the light absorption depth, a properly dimensioned network of donor – acceptor hetero-junction should be more efficient in terms of the exciton dissociation than a double – layer structure with a single, planar donor – acceptor hetero-junction. However, such a system of spatially distributed donor – acceptor hetero-junctions may contain imperfections that degrade performance, such as fully dispersed domains and cul-de-sac-type discontinuities of the donor and/or acceptor phases. Furthermore, an enlarged phase boundary volume accompanies this extended interface area in which donor and acceptor species are molecularly mixed. This is likely to result in increased energy level disorder, causing an increase of the charge trap density and a reduction of the electron and/or hole mobility. Hence, though exciton dissociation can be enhanced but transport is impeded by the circuitous geometry of the interface. For these and other reasons, the device performance becomes lower than expected.

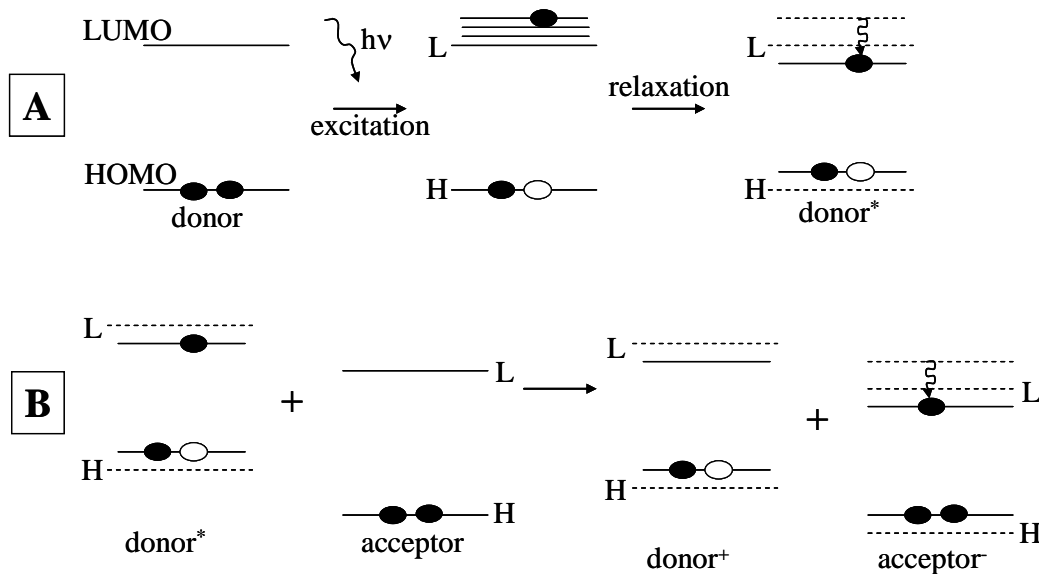


**Figure 1.11** (A) Creation of the bound electron– hole pair (exciton, designated with \*) in an organic molecular semiconductor upon excitation by light and subsequent relaxation. (B) Electron transfer between donor\* and acceptor: a hole carrier (donor<sup>+</sup>) and an electron carrier (acceptor<sup>-</sup>) are created.

## Interaction of Electromagnetic Radiation with Organic Semiconductors

The mechanism, by which absorption of photon in a conjugated polymer produces charge carriers, has been a topic of lively discussion. It has been generally accepted that, in conventional organic solids, such as molecular crystals, molecular glasses, made up of oligomers and molecularly doped polymers in which the host acts as an inert binder-absorbed photons, generate singlet or after intersystem crossing, triplet neutral excitations [35]. Transfer of one of the constituent charges to an adjacent chromophore, thus creating a charge transfer state, requires additional energy, as does the subsequent escape of the electron – hole pair from its mutual Coulombic potential. The difference between the energy of fully separated charges and the singlet exciton energy is referred to as exciton binding energy  $E_b$  that is of the order of 1 eV.

It is well known that, in bulk of molecular solids, a vibrationally relaxed exciton needs an energy  $\gg KT$ , at room temperature, in order to dissociate in a pair of free



charges. Therefore, intrinsic photoconduction should commence at higher photon energies only. This is confirmed by experiments on pure Anthracene crystals, in which, photo-injection from the electrodes was eliminated [59]. However, unless special precautions are taken, there is always some photogeneration occurring, closer to the absorption edge, notably, if the illuminated node is biased positively [60]. It is caused by exciton dissociation at the electrode, when the electron is transferred to the electrode and the remaining hole is only weakly bound to its image-charge in the metal. In principle, this process should be symmetric with respect to the electrode polarity. However, it is not and the reason is charge carrier trapping at the interface. In systems, with moderately low oxidation potentials, there are always unintentional oxidation products, serving as deep electron traps [61,62]. The photocurrent is yielded as a function of photon energy, i.e., penetration depth of the light has been used as a probe for exciton diffusion length of the exciton, which can reach the electrode. Unfortunately, this method yields meaningful results only when the diffusion lengths are of order of incident light penetration depth. There is clear evidence that in conjugated polymers polymer/electrode interface play a role an important role in photoconduction. Dissociation of excitons in the bulk can occur when the sample is deliberately or unintentionally doped by dopants with either high electron affinity or very low oxidation potential. In the course of its diffusion, an exciton can transfer one of its charges to the dopant. Photovoltaic power conversion using  $\pi$ -conjugated polymers rests upon this process [63, 64, 65]. To be efficient, it has to ensure that every exciton reaches a dopant, the generated electron – hole pairs dissociate into free carriers rather than recombine geminately [66, 67]. The condition under which vibrationally relaxed singlet exciton can dissociate is that the relevant rate constant is comparable to the rate of exciton decay to the ground state. Since, in molecular crystals the energy of a charge transfer state is  $\sim 0.5$  eV larger than that of singlet exciton [68], thermally activated dissociation is noncompetitive. In  $\pi$ - conjugated polymers, this process is feasible provided, there is an electric field applied that is sufficiently strong to compensate for the energy mismatch. On the other hand, conjugated polymer on-chain excitons are already comparable to the intermolecular separation [69]. This helps in

charge transfer from one chain to adjacent chain, unlike, in molecular crystals where extra energy is needed for the process. Fluorescence quenching in polymers by electric field as large as  $1 \text{ MV}\cdot\text{cm}^{-1}$  [70, 71] provides unambiguous evidence that a neutral singlet exciton can dissociate into a pair of charges. Transient absorption of the created charges proves that dissociation occurs within the entire lifetime of the singlet excitons [72].

## Transport Length Scales in Semiconductors

The physics of semiconducting organic devices (FETs, LEDs, photovoltaics) is quite different from the physics of inorganic semiconductors. In conventional doped inorganic semiconductors, the current characteristics are n-type or p-type. The physics of 1-D dimensional transport in conjugated systems are uniquely different as described in the earlier sections. However, it is useful to evaluate and define equivalent quantities to compare the figure of merit and performance parameters of organic devices involving photogenerated charge carriers. Conjugated semi conducting polymer material parameters can be compared with that of inorganic semiconductors and molecular solids, as shown in **Table 1.3**. Transport of charges due to diffusion mechanism provides a characteristic length scale of semiconductors, called diffusion length. Charge carrier diffusion length  $\sim L_d$  is an important parameter in determining the performance devices such as solar cells, bipolar transistors, optical detectors, and more. This diffusion is exactly analogous to a diffusion of natural gas with a concentration gradient exists in container. There are many different techniques that have been used to determine  $L_d$  in inorganic semiconductors, which can be an important tool for polymeric semiconductors characterizations. Some of the most widely used methods are:

- (i) Electron-beam induced currents (EBICs) [73]
- (ii) Surface photovoltage (SPV) [74]
- (iii) Photoluminescence (PL) [75]
- (iv) Steady State Photogating Method (SSPG) [76, 77]
- (v) Optical Beam Induced Current (OBIC) [78]

**Table 1.3** Inorganic and organic semiconducting material parameters[(i) →[79], (ii) →[79], (iii) →[80], (iv) →[81]]

Material	Si [(i)]	GaAs[(ii)]	Amorphous Si [(iii)]	Polymers [(iv)]
Parameters				
Mobility ( $\mu$ ) ( $\text{cm}^2\text{v}^{-1}\text{s}^{-1}$ )	$\mu_e = 1500$ $\mu_h = 450$	$\mu_e = 8500$ $\mu_h = 400$	$\mu_e = \sim 1-10$ $\mu_h = \sim 1-10$	$\mu_e = 10^{-5}$ $\mu_h = 10^{-3}$
Diffusion Coefficient (D) ( $\text{cm}^2\text{s}^{-1}$ )	$D_e = 3.88$ $D_h = 1.16$	$D_e = 22.0$ $D_h = 1.03$	$D_e \text{ \& } D_h \approx 10^{-3}$ to $10^{-5}$	$D_e = \sim 10^{-8}$ $D_h = \sim 10^{-6}$
Diffusion length ( $L_d$ ) ( $\mu\text{m}$ )	$L_{de} = \sim 10^4$ $L_{dh} = \sim 10^4$	$L_{de} =$ $L_{dh} = 30-50$	$L_{de} = \sim 0.20$ $L_{dh} = \sim 0.20$	$L_{de} = \text{????}$ $L_{dh} = \text{????}$
Resistivity ( $\rho$ ) ( $\Omega\text{-cm}$ )	$2.3 \times 10^5$	$10^8$	$3.3 \times 10^4$	$\sim 10^6$
Dielectric Constant ( $\epsilon$ )	11.9	13.1	$\sim 11.8$	$\sim 3.5$
Energy gap (eV) at 300K	1.12	1.424	$\sim 1.35$	1.0 - 3.0
Crystal Structure	Diamond	Zincblende	Amorphous	Amorphous-polycrystalline
Minority carrier lifetime ( $\tau$ ) (s)	$2.5 \times 10^{-3}$	$\sim 10^{-8}$	Undoped $10^{-12} - 10^{-1}$	Undoped $10^{-12} - 10^{-1}$
Temperature coefficient	Negative	Negative	Negative	positive

### (i) EBIC Technique

In the EBIC method, a p-n junction or a Schottky barrier is viewed edge-on. With the scanning electron microscope in a line scan mode, the electron beam scans the semiconductor perpendicular to the potential barrier and generates electron-hole pairs. The generated charge carriers then diffuse to the junction, where the electrons and holes are separated and a current is generated, in the external circuit. This current, referred to as the EBIC current, reflects the amount of excess carriers generated. A theoretical fit to the experimentally measured current allows for the evaluation of L. The main disadvantage of the EBIC technique is that, the shape of the EBIC curve depends on several additional factors apart from L, most importantly, on the surface recombination velocity (SRV) of the surface on which the beam impinges.

## (ii) SPV Technique

In the SPV method, a super-band-gap energy monochromatic light of a wavelength  $\lambda$  illuminates the semiconductor. The intensity of the light  $I$  is changed in order to keep the measured photovoltage (which is proportional to the concentration of the minority carriers available by the surface) constant. Under certain assumptions [72], an  $I$  versus  $\lambda$  curve of the form  $I = C[1/\alpha(\lambda) + L]$  (where  $C$  is a constant) is obtained. Combining the  $I(\lambda)$  results with the knowledge of the  $\alpha(\lambda)$  dependence enables the extraction of  $L$ . Hence, the main disadvantage of the SPV technique is that, it requires an accurate knowledge of the  $\alpha(\lambda)$  dependence of the measured semiconductor.

## (iii) PL Technique

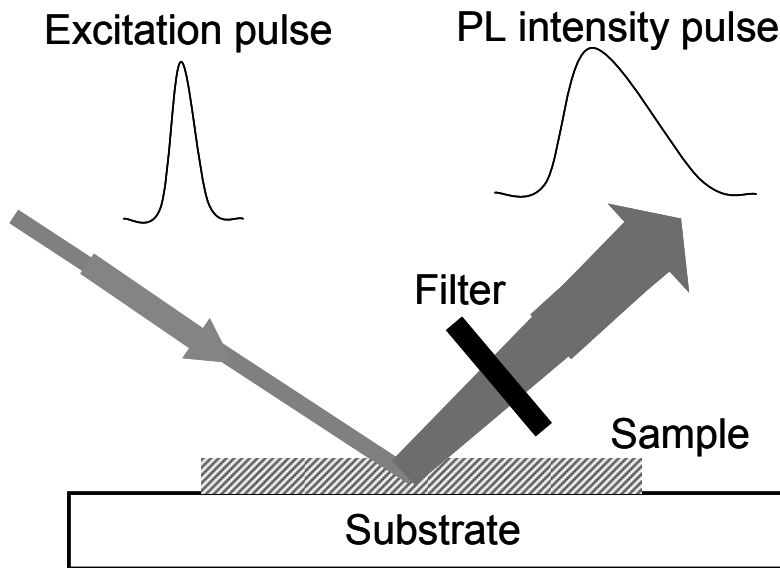


*Figure 1.12 Schematic of time resolved PL setup*

Time resolved PL measurement studies give the information about minority carrier lifetime ( $\tau$ ) and diffusion coefficient ( $D$ ) of the carriers. In this technique, a Gaussian beam of pulse light is used to excite the sample and emitted Gaussian PL decay measurements are carried out using photon-counting technique. When the radial intensity

profile of the excitation light is irradiated on sample, the density distribution of electron-hole pairs just after the short pulse excitation is proportional to  $\exp[-2(x^2 + y^2)/w_{exc}^2]$ . The electron-hole pairs then diffuse laterally with the diffusion constant  $D$  and recombine with the lifetime,  $\tau$ , which is expressed by the following equation for the density  $n(x, y, t)$ ,

$$n(x, y, t) = n_0 \left(1 + 8tD/w_{exc}^2\right)^{-1} \times \exp\left[-2(x^2 + y^2)/(w_{exc}^2 + 8tD) - t/\tau\right] \quad (1.16)$$

The PL intensity observed is proportional to the electron-hole pair density within the Gaussian radius  $w_{obs}$ , where  $w_{obs}$  is the Gaussian radius of intensity profile at the observed wavelength. Integrating  $n(x, y, t)$  for  $x$  and  $y$  with the weight function  $\exp[-2(x^2 + y^2)/w_{obs}^2]$ , one can obtain an analytical expression of the PL intensity  $I(t)$  as follows

$$I(t) = I_0 \left[1 + 8tD/(w_{exc}^2 + w_{obs}^2)\right]^{-1} \exp[-t/\tau] \quad (1.17)$$

The fitting of measured time resolved PL with  $I(t)$  can give  $D$  and  $\tau$ , whence diffusion length  $L = \sqrt{D\tau}$  also.

#### (iv) SSPG Technique

In SSPG, two coherent light beams of different intensities, those interfere and create a photocarriers grating, illuminate the sample. If the grating period is much larger than the carrier diffusion length, a well-defined concentration grating of photocarriers is created in the sample. On the other hand, when the grating spacing is comparable to or shorter than the diffusion length an almost uniform carrier's concentration occurs in spite of non-uniform photogeneration. In order to detect the photocarriers grating amplitude, which is a good indicator of the diffusion length  $L$ , a photocurrent perpendicular to the grating fringes is measured, in this technique. The SSPG theory developed by Ritter, Zeldov and Weiser, based on small-signal approach connects the magnitude of the measured photocurrent with the ambipolar diffusion length under the assumption of local space charge neutrality. [76, 77] The consequences derived from their theory are at

present widely utilized for the analysis of SSPG experimental data [82, 83]. This technique is applicable for extended states, hopping transport and widely used for disordered semiconductor systems.

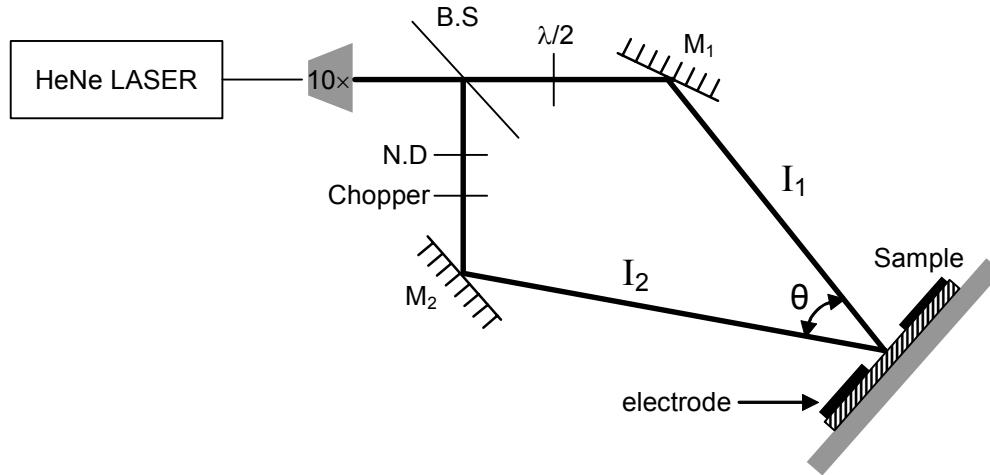


*Figure 1.13 Schematic of SSPG setup*

### (v) OBIC Technique

In OBIC technique, a focused optical beam (it can be from far field optical microscope or confocal or near field microscope setup) is used to scan the sample. When the sample is illuminated with a monochromatic focused light beam with energy higher than the band gap of semiconductor, it generates electron-hole pairs locally at illumination site. These photogenerated carriers give rise to a photocurrent in output circuit as a function of illumination position from the collecting electrode. The photocurrent in this process is diffusion – recombination mode driven, which gives the information about the mobility-lifetime product ( $\mu\tau$ ) for material used for studies. This is almost similar to the EBIC setup but with many advantages over EBIC technique like (i) It is non-destructive technique. (ii) It is at atmospheric pressure in ambient. (iii) It is a material specific probe (light wavelength). (iv) There is high spatial resolution ( $\sim 10$  nm using aperture less probe in near field regime). (v) There are simultaneously optical and electrical measurements. (vi) spectroscopy with very high resolution  $\rightarrow$  (a) to study

single quantum structures (i.e., dots, wires, particles) or single molecule chromophores, (b) to reduce background emission when studying these small objects. This technique has been used to characterize variety of inorganic semiconductors. As shown in schematic **Fig 1.13**, it can give an estimation of  $L_d$  in coplanar devices for semiconducting polymer based devices [84]. It becomes more interesting in the case of sandwich devices also where wavelength of optical beam decides the charge generation region [85, 86], so this technique with different excitation energy beam can provide complete 3D information about sample.

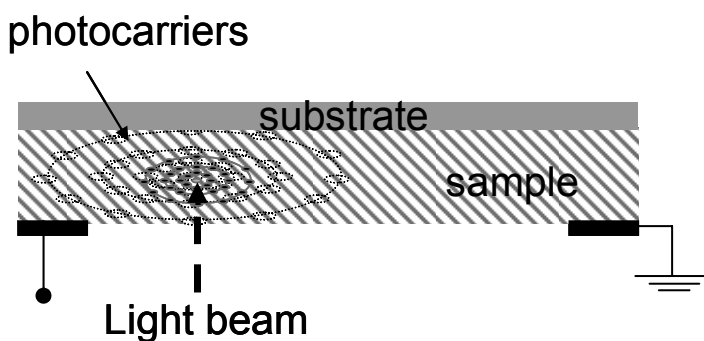


*Figure 1.14 Schematic of OBIC setup*

## Thesis Overview

This research work started with the primary motivation to determine transport length scales for photoinduced negative (electron) and positive (holes) charge carriers in conjugated polymer semiconductors. Conjugated polymer chains packing in solid state give an amorphous network. This thesis presents a photophysical insight of length scales involved and effect of ordering the polymer chains on electrical transport parameters. A study on both kind of charge carriers (electrons and holes), in single device without any external bias, can reveal the degree of ambipolar conduction in these polymer films. However, molecular level calculations have predicted there is asymmetry in carrier transport arising from macroscopic as well as from microscopic parameters. The electronic levels are expected to be not symmetric under different doping conditions. This asymmetry of electronic levels provides an additional contribution in mismatch of transport parameters for electron and holes [87]. There are two crucial facts, which make

them better conductors for one kind of charge carriers (i) there is mismatch of electronic levels of contact metal electrodes and semiconductor, hence different extraction efficiency and (ii) charge carriers- trapping centers of electrons through extrinsic impurities in the semiconductor or at the semiconductor–dielectric interface.

These inherently disordered polymer semiconductors has complex electronic transport processes and very difficult to provide an exact physical model. There are reports in literature for device modeling of these organic semiconductor devices using equivalent circuit model. These circuit models are supposed to provide important material and device parameter, with the compromise in deep microscopic details of physical processes. Nevertheless, this thesis demonstrates a successful use of discrete circuit element model for semiconducting polymer based photovoltaic structure. This model provides important information about photoinduced carrier dynamics along device parameters [88, 89]. This thesis demonstrates the general approach for studying length scales in model polymer systems. The model systems chosen were 2-D ordered (P3HT), disordered MEHPPV and nematic liquid crystalline (oriented poly(dioctylfluorene-bithiophene), PFO-TT on rubbed substrates) systems. Problems were defined in the context of existing information in the literature. Experiments were carried out to address these questions. The results in form of decay lengths prevailing in the system were analyzed in terms of the relative degree of disorder, efficacy of hole transport vis-à-vis electron transport, and the preferred directions of transport. The implications of the results and the understanding also form the basis of large area position and polarization dependent sensors from these polymer based semiconductors. The applications were demonstrated over large length scales with options such flexible substrate to fabricate angle sensitive detector, 1D and 2D co-ordinate of optical beam, electrically tunable spatial response, polarization sensor from aligned polymer chains based devices.



## References

---

- [1] H. Shirakawa, E. J. Louis, A. G. MacDiarmid, C. K. Chiang and A. J. Heeger, *J. Chem. Soc. Chem. Commun.* **16**, 578 (1977)
- [2] C. K. Chiang, C. R. Fincher, Jr., Y. W. Park, and A. J. Heeger, H. Shirakawa, E. J. Louis, S. C. Gau, and Alan G. MacDiarmid, *Phys. Rev. Lett.* **39**, 1098 (1977)
- [3] J. H. Burroughes, D.D.C. Bradley, A. R. Brown, R. N. Marks, K. Mackay, R. H. Friend, P. L. Burn, A. B. Holmes, *Nature* **347**, 539 (1990)
- [4] N. S. Sariciftci, L. Smilowitz, A. J. Heeger, F. Wudl, *Science* **258**, 1474 (1992)
- [5] G. Yu, J. Gao, J. C. Hummelen, F. Wudl, A. J. Heeger, *Science* **270**, 1789 (1995)
- [6] Z. Bao, A. Dodabalapur, A. Lovinger *Appl. Phys. Lett.* **69**, 4108 (1996)
- [7] H. Sirringhaus, N. Tessler, R. H. Friend, *Science* **280**, 1741 (1998)
- [8] H. Sirringhaus, P. J. Brown, R. H. Friend, M. M. Nielsen, K. Bechgaard, B. M. W. Langeveld-Voss, A. J. H. Spiering, R. A. J. Janssen, E. W. Meijer, P. Herwig, and D. M. de Leeuw, *Nature* **401**, 685 (1999)
- [9] R. Osterbacka, C. P. An, X. M. Jiang, Z. V. Vardeny, *Science* **287**, 839 (2000)
- [10] G. Wang, J. Swensen, D. Moses, A. J. Heeger, *J. Appl. Phys.* **93**, 6137 (2003)
- [11] N. Tessler, G. J. Denton, R. H. Friend, *Nature* **382**, 695 (1996)
- [12] A. R. Brown, A. Pomp, C. M. Hart, D. M. de Leeuw, *Science* **270**, 972 (1995)
- [13] C. J. Drury, C. M. J. Mutsaers, C. M. Hart, M. Matters, and D. M. de Leeuw, *Appl. Phys. Lett.* **73**, 108 (1998)
- [14] A. Hepp, H. Heil, W. Weise, M. Ahles, R. Schmechel, H. V. Seggern, *Phys. Rev. Lett.* **91**, 157406 (2003)
- [15] K. Kim, J. Liu, M. A. G. Namboothriy, D. L. Carroll, *Appl. Phys. Lett.* **90**, 163511 (2007)
- [16] H. E. Katz, X. M. Hong, A. Dodabalapur, and R. Sarpeshkar, *J. Appl. Phys.* **91**, 1572 (2002)
- [17] <http://www.polyic.com> (13.56 MHz, Stability > 1 year, working distance ~ 10 meters)
- [18] K. Tada, M. Onoda, *Thin Solid Films* **499**, 19 (2006)

- 
- [19] B. Crone, A. Dodabalapur, A. Gelperin, L. Torsi, H. E. Katz, A. J. Lovinger, Z. Bao, *Appl. Phys. Lett.* **78**, 2229 (2001)
- [20] J. H. Burroughes, C. A. Jones, R. H. Friend, *Nature* **335**, 137 (1988)
- [21] F. C. Grozema, T. J. Savenije, M. J. W. Vermeulen, L. D. A. Siebbeles, J. M. Warman, A. Meisel, D. Neher, H. -G. Nothofer, U. Scherf, *Adv. Mat.* **13**, 1627 (2001)
- [22] R. J. Kline, M. D. McGehee, M. F. Toney, *Nat. Mat.* **5**, 222 (2006)
- [23] I. McCulloch, M. Heeney, C. Bailey, K. Genevicius, I. MacDonald, M. Shkunov, D. Sparrowe, S. Tierney, R. Wagner, W. Zhang, M. L. Chabinyc, R. J. Kline, M. D. McGehee, M. F. Toney, *Nat. Mat.* **5**, 328 (2006)
- [24] R. A. Street, J. E. Northrup, A. Salleo, *Phys. Rev. B* **71**, 165202 (2005)
- [25] K. P. C. Volhardt *Organische Chemie*, VCH-Verlag, Weinheim 1990.
- [26] (i) G. Padmanaban, S. Ramakrishnan, *J. Am. Chem. Soc.* **122**, 2244 (2000)  
(ii) K. Nagesh, D. Kabra, K.S. Narayan, S. Ramakrishnan, *Synth. Met.* **155**, 295 (2005)
- [27] M. Pope, C. W. C. E. Swenberg *Electronic processes in Organic Crystals*, Clarendon Press, Oxford 1982.
- [28] Lay- Lay Chua, J. Zaumseil, J. -F. Chang, E. C. -W. Ou, P. K. -H. Ho, H. Sirringhaus, R. H. Friend, *Nature* **434**, 194 (2005)
- [29] (i) W. P. Su, J. R. Schrieffer, A. J. Heeger; *Phys. Rev. Lett.* **42**, 1698 (1979)  
(ii) W. P. Su, J. R. Schrieffer, A. J. Heeger, *Phys. Rev. B* **22**, 2099 (1980)
- [30] W. P. Su and J. R. Schrieffer, *Proc. Natl. Acad. Sci. USA* **77**, 5626 (1980)
- [31] J. L. Brédas, R. R. Chance, and R. Silbey, *Mol. Cryst. Liq. Cryst.* **77**, 319 (1981)
- [32] A. J. Heeger, S. Kivelson, J. R. Schrieffer, W. P. Su *Rev. of Modern Phys.* **60**, 781 (1988)
- [33] L. Pautmeier, R. Richert, H. Bassler, *Synth. Met.* **37**, 271 (1990)
- [34] H. Bassler, *Phys. Status Solidi B* **175**, 15 (1993)
- [35] Y. N. Gartstein, E. M. Conwell, *Chem. Phys. Lett.* **245**, 351 (1995)
- [36] E. W. Monroll, H. Scher, *J. Stat. Phys.* **9**, 101 (1973)
- [37] H. Scher, E. W. Monroll, *Phys. Rev. B* **12**, 2455 (1975)
- [38] J. Kalfter, R. Shibley, *Phys. Rev. Lett.* **44**, 55 (1980)

- 
- [39] G. Pfister, S. Grammatica, J. Mort, *Phys. Rev. Lett.* **37**, 1360 (1976)
- [40] B. Ries, H. Bassler, *Phys. Rev. B* **35**, 2295 (1987)
- [41] L. B. Schein, D. Glatz, J. C. Scott *Phys. Rev. Lett.* **65**, 472 (1990)
- [42] E. Muller – Horsche, D. Haarer, H. Scher *PRB* **35**, 1273 (1987)
- [43] S. J. Santos Lemus and J. Hirsch, *Philos. Mag. B*, **53**, 25 (1986)
- [44] A. Peled, L. B. Schein, *Chem. Phys.* **153**, 422 (1988)
- [45] W. G. Gill, *J. Appl. Phys.* **43**, 5033 (1972)
- [46] H. Bassler, *Phys. Stat. Sol. (b)* **107**, 9 (1981)
- [47] A. Miller, E. Abrahams, *Phys. Rev.* **120**, 745 (1960)
- [48] H. Bassler, *Phys. Status. Solidi B* **175**, 15 (1993) and reference cited therein
- [49] T. P. Carter, M. Manavi, W. E. Moerner, *J. Chem. Phys.* **89**, 1768 (1998)
- [50] B. Hartenstein, H. Bassler, A. Jakobs, K. W. Kehr, *Phys. Rev. B* **54**, 8574 (1996)
- [51] A. Hirao, H. Nishizawa, M. Sugiuchi, *Phys. Rev. Lett.* **75**, 1787 (1995)
- [52] Y. N Gartstein and E. M. Conwell *Chem. Phys. Lett.* **245**, 351 (1995)
- [53] Z. G. Yu, D. L. Smith, A. Saxena, R. L. Martin and A. R. Bishop *Phys. Rev. B* **63**, 085202 (2001)
- [54] S. Narioka et al, *Appl. Phys. Lett.* **67**, 1899 (1995)
- [55] (i) H. Ishii, K. Seki, *IEEE Trans. Electron Dev.* **44**, 1295 (1997)
- (ii) H. Ishii, K. Sugiyama, E. Ito, K. Seki, *Adv. Mat.* **11**, 605 (1999)
- [56] D. Yoshimura, H. Ishii, Y. Ouchi, E. Ito, T. Miyamae, S. Hasegawa, K. K. Okudaira, N. Ueno, K. Seki, *Phys. Rev. B* **60**, 9046 (1999)
- [57] Y. Shen, A. R. Hosseini, M. H. Wong, G. G. Malliaras, *Rev. chemphyschem* **5**, 16 (2004)
- [58] M. A. Lambert, P. Mark, *Current injection in solids*, Academic Press, New York, (1970)
- [59] K. Kato, C.L.Barun, *J. Chem. Phys.* **72**, 172 (1980)
- [60] R. R. Chance, C. L. Barun, *J. Chem. Phys.* **59**, 2269 (1973)
- [61] R. R. Chance, C. L. Barun, *J. Chem. Phys.*, **64**, 3573 (1976)

- 
- [62] D. Hertel, H. Bässler, S. Möller, H. Tillmann, H. H. Horhold, *Mol. Cryst. Liq. Cryst.* **355**, 175 (2001)
- [63] A. J. Heeger, *J. Chem. Phys. B* **105**, 8475 (2001)
- [64] C. J. Barbec, N. S. Sarciftci, J. C. Hummelen, *Adv. Func. Mater.* **11**, 15 (2001)
- [65] D. M. Russell, A. C. Arias, R. H. Friend, C. Silvaa, C. Ego, A. C. Grimsdale, K. Mullen *Appl. Phys. Lett.*, **80**, 2204 (2002)
- [66] M. C. Scharber, N. A. Schultz, N. S. Sarciftci, C. J. Barbec, *Phys. Rev. B* **67**, 85202 (2003)
- [67] A. Nollau, M. Hoffmann, T. Fritz, K. Leo, *Thin Solid Films* **368**, 130 (2000)
- [68] L. Sebastian, G. Weiser, G. Peter, H. Bässler, *Chem. Phys.* **75**, 103 (1983)
- [69] J. W. Vander Horst, P. A. Bobbert, M. A. J. Michels, H. Bässler, *J. Chem. Phys.* **114**, 6950 (2001)
- [70] B. Schweitzer, V. I. Arkhipov, H. Bässler, *Chem. Phys. Lett.*, **304**, 365 (1999)
- [71] D. Hertel, E. V. Soh, H. Bässler, L. J. Rothberg, *Chem. Phys. Lett.*, **361**, 99 (2002)
- [72] V. Gulbinas, Y. Zauhitsyn, V. Sundstrom, D. Hertel, H. Bässler, A. Yartsev *Phys. Rev. Lett.* **89**, 107401 (2002)
- [73] R. Hakimzadeh, S. G. Bailey, *J. Appl. Phys.*, **74**, 1118 (1993)
- [74] Alvin M. Goodman *J. Appl. Phys.* **32**, 2550 (1961)
- [75] C. H. Wang *IEEE Trans. Electron Devices* **38**, 2169 (1991)
- [76] D. Ritter, E. Zeldov, K. Weiser *Appl. Phys. Lett.* **49**, 791 (1986)
- [77] D. Ritter, E. Zeldov, K. Weiser *J. Appl. Phys.* **62**, 4563 (1987)
- [78] (i) T. Wilson, E. M. McCabe *J. Appl. Phys.* **58**, 2638 (1986)
- (ii) T. Wilson, E. M. McCabe *J. Appl. Phys.* **61**, 191 (1987)
- T. Wilson, E. M. McCabe, D. K. Hamilton *J. Appl. Phys.* **61**, 191 (1987)
- [79] S. M. Sze, "Physics of Semiconductor Devices" John Wiley publishers, 2001.
- [80] A. Madan, M. P. Shaw, "The Physics and Applications of Amorphous Semiconductors", Academic Press, Inc. 7.
- [81] R. Farchoni, G. Grosso, "Organic Electronic Materials: Conjugated Polymers and Low Molecular Weight Organic Solids", Springer Publisher Edition- 1<sup>st</sup> (2001)

- 
- [82] K. Weiser, E. Zeldov, D. Ritter, US Patent 4, 891, 582, 1990.
- [83] I. Balberg, A. E. Delahoy, H. A. Weakliem, *Appl. Phys. Lett.* **53**, 1949 (1988)
- [84] D. Kabra, K. S. Narayan, *Adv. Mat.* 2007 (in press)
- [85] S. Dutta, K. S. Narayan, *Appl. Phys. Lett.* **87**, 193505 (2005)
- [86] M. Breban, D. B. Romero, S. Mezheny, V. W. Ballarotto, E. D. Williams, *Appl. Phys. Lett.* **87**, 203503 (2005)
- [87] J. L. Bre´ das, J. P. Calbert, D. A. da Silva Filho, J. Cornil, *PNAS* **99**, 5804 (2002)
- [88] D. Kabra, S. Sriram, N. S. Vidhyadhiraja, K. S. Narayan, *J. Appl. Phys.* **101**, 64510 (2007)
- [89] J. Verma, D. Kabra, K. S. Narayan, N. S. Vidhyadhiraja, *European Phys. J. Appl. Phys.* 2007 (submitted)



# CHAPTER 2

## Device Fabrication and Measurement Techniques

### 2.1 Introduction

The design of device structures and the fabrication processes form an essential part in extracting the optimum properties of constituent materials. The measurement techniques and the different methods for analysis of the device characteristics are vital aspects for understanding the device physics and the active-material properties. This dissertation primarily deals with two device structures: (i) an asymmetric overlap of two terminal lateral structure (see *Figure 2.1a*) for lateral transport length scales measurements of photogenerated charge carriers [1] and (ii) a three terminal structure (see *Figure 2.1b*) for optical position sensitive detector [2, 3]. The following sections focus on the fabrication processes of these structures.

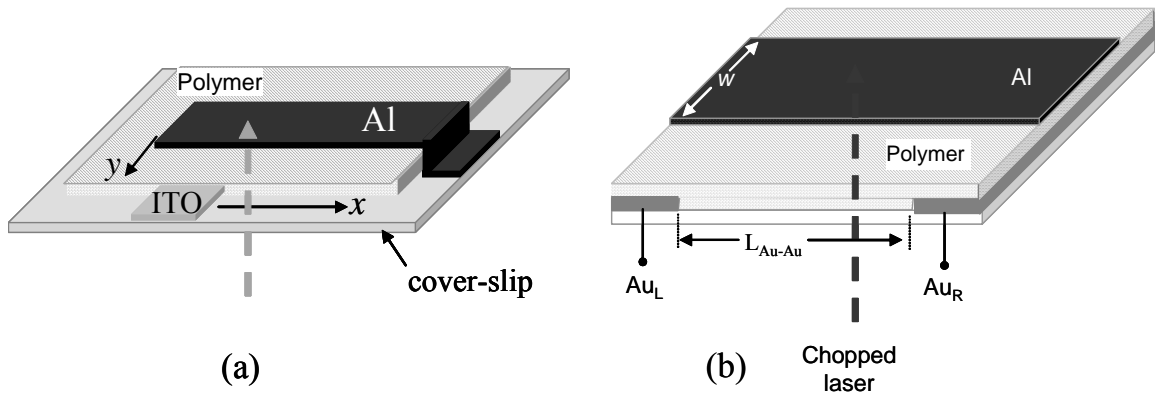


*Figure 2.1* Typical device structures (a) 2-terminals and (b) 3-terminals

The device structures were prepared on variety of substrates including quartz plate, glass plate, glass cover-slip of reduced thickness and polyethylene terephthalate (PET). Variety of factors such as the type of solvent, substrate treatment and annealing

conditions come into play during the fabrication process. The pre-treatment of the active material and purification process were also important considerations.

## 2.2 Materials

Three kinds of model semiconducting polymers were used for studies. They are as follows (1) P3HT, (2) MEHPPV and (3) PFO – TT.

The polymer chains were aligned using (a) surfactant Hexamethyldisilazane (HMDS) treated substrates and (b) rubbed Polyimide (PI) channels coated substrates. A brief description of polymers is presented.

### 2.2.1 Poly(3-hexylthiophene) (P3HT)

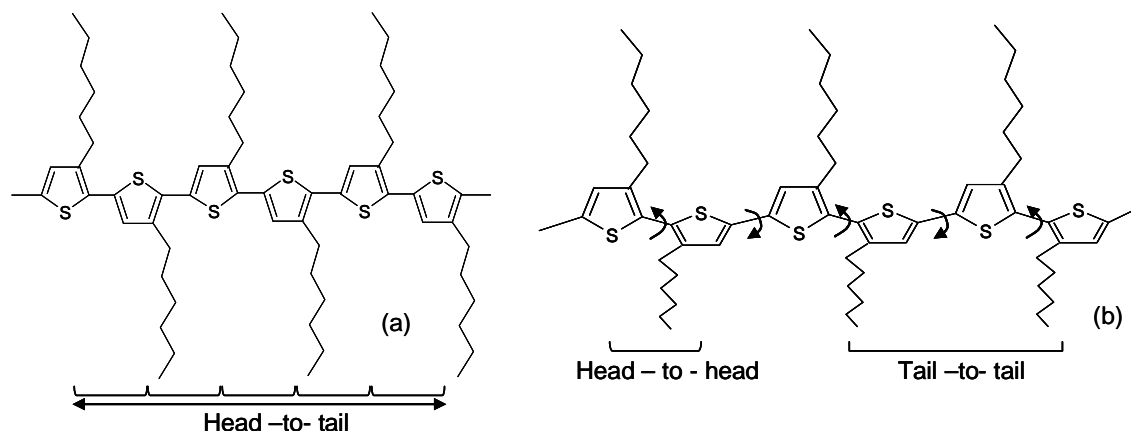


**Figure 2.2** (a) *rr*-P3HT chain, showing exclusively head-to-tail interaction, resulting in a planar backbone. (b) *rra*-P3AT chain, showing exclusively head-to-head and tail-to-tail interactions, resulting in twisting of the backbone.

P3HT belongs to the group of alkyl-substituted thiophene compounds usually referred to as poly(3-alkylthiophene) (P3AT). Polythiophene is a leading candidate for optoelectronic application due to sufficient thermal stability ( $T_g > 150\text{ }^\circ\text{C}$ ). In the quest of solubility and processibility, the first synthesis of P3AT was reported more than two decades ago [4]. Typically there are three well-known methods for synthesis of P3ATs, namely (i) electrochemical polymerization, (ii) oxidative polymerization of 3-alkylthiophene by oxidants like ferric chloride ( $\text{FeCl}_3$ ) and (iii) polymerization by



dedihalogenation of 2,5-dihalo-3-alkylthiophene [5]. The P3AT structure comprise of side chains attached to either one of the  $\beta$  - carbons (furthest from the sulphur atom), giving head – to – head, head – to – tail and tail –to – tail interactions between adjacent rings. Regioregular alkyl – substituted polythiophenes [6, 7] and oligothiophenes [8] have also been synthesized, in which alkyl chains are always substituted to the same type of  $\beta$ -carbon atom. This configuration results in a predominantly head–to–tail interaction, as shown in **Figure 2.2**, therefore reducing steric interactions between the alkyl chains.

In the alkyl-substituted oligothiophenes and poly(alkylthiophene), where the synthesis is not controlled to yield regioregular substitution, head – to –head and tail – to – tail interactions give rise to a twisted backbone, in which thiophene rings are not coplanar. This results in a reduction of the intra-molecular  $\pi$ -conjugation along the chain and also a slight increase in the separation between  $\pi$ -conjugated chains when stacked in the solid state, leading to reduced intermolecular  $\pi$ -stacking. In addition, regiorandom  $\beta$ -substitution can cause spatial disorder of the wave-function overlap of aromatic rings involved in cofacial  $\pi$ -stacking, which is detrimental to aggregation and intermolecular electrical conduction mediated by  $\pi$ -stacking. Regiorandom or lack of  $\pi$ -stacking also has an implication for the quantum efficiencies of fluorescence as torsional oscillations are

considered to be involved in some non-radiative decay channels [9].

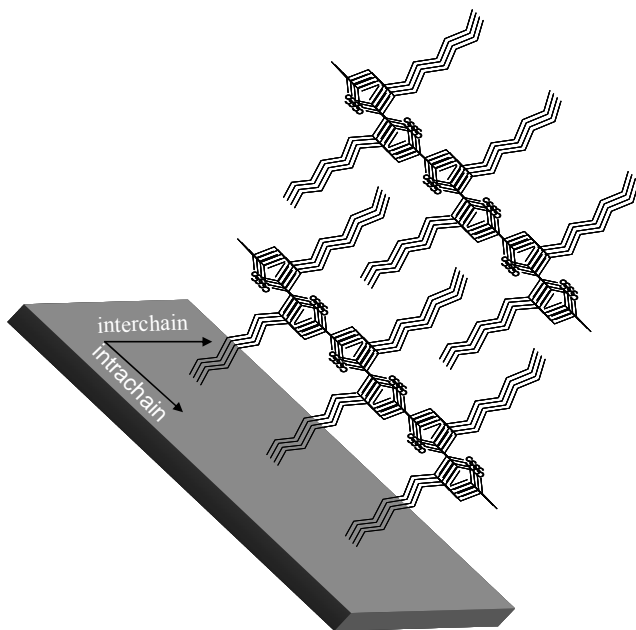


**Figure 2.3** Schematic view of intermeshed stacks of alkylthiophene chain

Solid state crystallographic studies [10] and images obtained by scanning tunneling microscopy (STM) [11] indicate that alkyl – substituted oligothiophenes and polythiophenes have a tendency to aggregate or self – assemble in a stacked interlocking comb-like structure as shown in **Figure 2.3**. In this case, the  $\alpha$ -carbon nearest to the sulphur atom involved in bonding of the oligomer backbone, leaves either one of the  $\beta$ -carbons available for substitution.

P3HT used in these studies were obtained from Aldrich, U.S.A. The organo Zinc reagents formed by reacting Ricke Zinc with 2,5 dihalothiophenes was used for synthesis of this polymer [12]. Absorption and photoluminescence spectroscopy results for P3HT

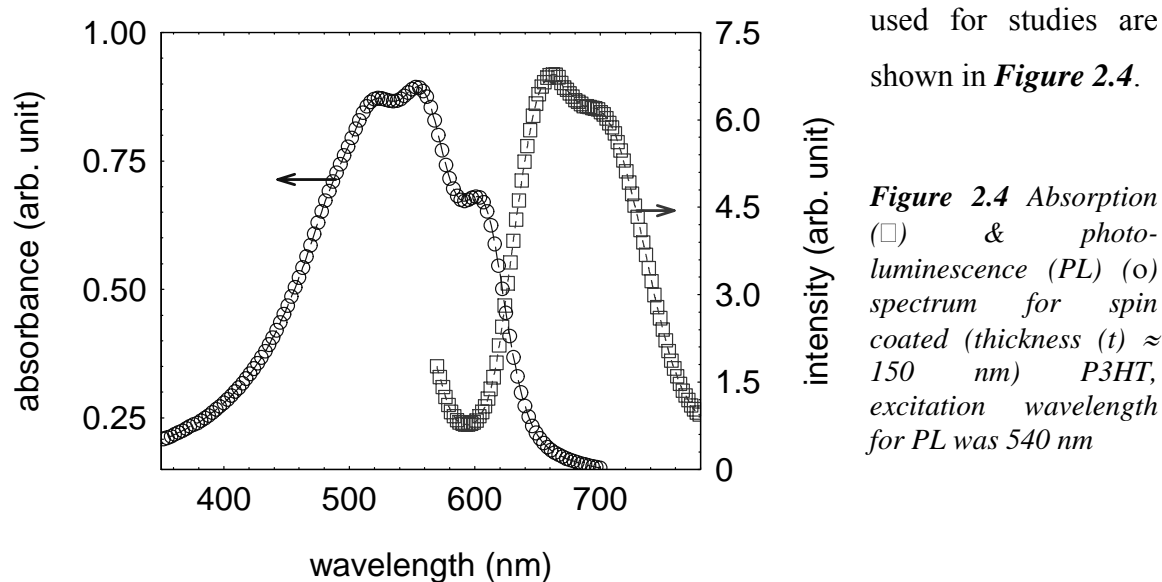


**Figure 2.4** Absorption ( $\square$ ) & photoluminescence (PL) ( $\circ$ ) spectrum for spin coated (thickness ( $t$ )  $\approx$  150 nm) P3HT, excitation wavelength for PL was 540 nm

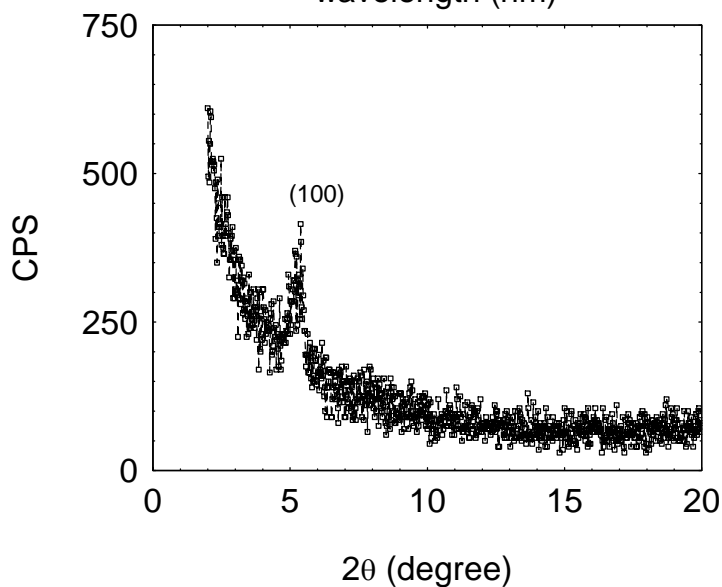


**Figure 2.5:** Grazing incidence-angle X-ray intensity as a function for scattering angle  $2\theta$  for regioregular P3HT film (3 mg/ml in  $\text{CHCl}_3$ ) on an insulating surface. The insulating surface was functionalized with HMDS

Grazing incidence angle x-ray diffraction (GIXRD) studies were done on P3HT films deposited on HMDS treated substrates, as shown in **Figure 2.5**. In GIXRD measurement (in plane), a peak at  $2q \gg 5^\circ$  ( $q$  is the angle of incidence), representing the (100) plane, was observed. The GIXRD measurement was conducted in CCMR, Cornell University, USA.

### HMDS

This is a surfactant, which passivates oxide based insulating surfaces hydrophobic in nature. This particular chemical property has made it one of the important chemicals for substrate treatment in solution based deposition techniques. Most of the conjugated polymer based devices are solution processible where polymer deposition is done on inorganic oxide surfaces ( $\text{SiO}_2$  and ITO). These polymer solutions generally

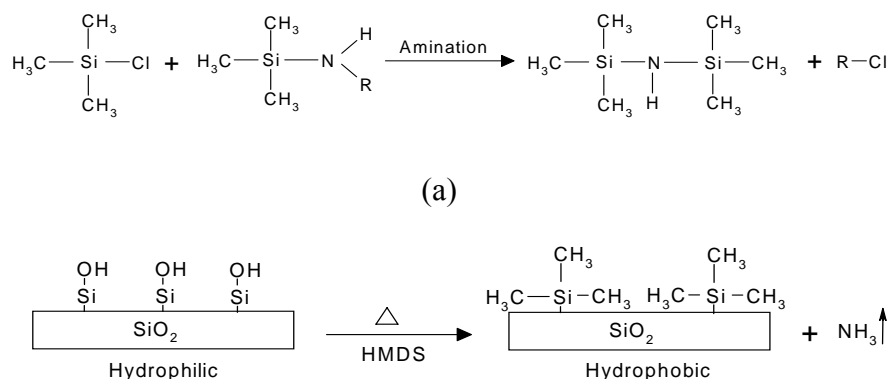


**Figure 2.6** (a) Synthesis of hexamethyldisilazane (HMDS) using amination method. (b) Surface modification of  $\text{SiO}_2$  using HMDS treatment.(b)

need hydrophobic surfaces for good adhesion, otherwise the films become irregular and inhomogeneous. For this reason the substrates is treated to make it defects free and have good linkage properties with polymers (a bridge between the inorganic substrate and the organic materials increasing the Van-der Waals interaction between the two surfaces). The common problem of oxide-coated silicon substrate ( $\text{Si}/\text{SiO}_2$ ) is the appearance of hydroxyl group in the form of silanol ( $\text{Si}-\text{OH}$ ) that makes the surface hydrophilic. The treatment  $\text{SiO}_2$  with HMDS replaces the hydroxyl groups at the  $\text{SiO}_2$  surface with methyl groups, forming  $[(\text{CH}_3)_3\text{Si}-\text{Si}]$  compound on the surface and ammonia as byproduct, as shown in **Figure 2.6**. Ammonia is conducted by heating under reflux. The apolar nature of the modified surface containing methyl groups apparently attracts the hexyl side chains of P3HT, which in turn leads to the assembly of lamella structure with b-axis oriented parallel to the substrate. HMDS treatment on insulating surface can be performed either by projecting HMDS vapor for 2 minutes at  $120^\circ\text{C}$  [13, 14] or by spin-coating HMDS, followed by annealing at  $120^\circ\text{C}$  for 1 hour [15].

### 2.2.2 Poly (2-methoxy-5-(2-ethylhexyloxy)-1,4-phenylene vinylene ) (MEHPPV)

MEHPPV is the most widely used polymer in electroluminescence devices. This polymer is a soluble derivative of poly(para- phenylene vinylene)(PPV). It has two side groups attached to phenyl ring at ortho (methoxy) and meta (ethylhexyloxy) positions. Chemical structure of MEHPPV is shown in *Figure 2.7*. This polymer is expected to be amorphous in nature due to flexible backbone and coiled, aggregates formed by long alkoxy sidegroup of chain in the solid state. Determination of the lowest energy structures in this polymer gives the relative values of ground state spacing between the chains and good idea of the sidegroups. Because of their planar backbones and long alkoxy sidegroups, their low-energy configurations in a film have the planes of the backbones parallel to each other. The results of such calculation suggest that there is a distance of 0.405 nm between the chains and exocyclic double bond on one chain sits over a ring of nearest neighbor [16].

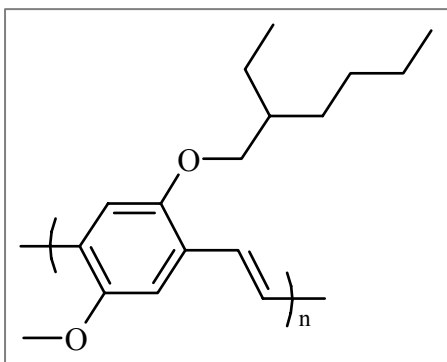


**Figure 2.7** Chemical Structure for Poly(2-methoxy-5-(2-ethylhexyloxy)-1,4-phenylene vinylene) [MEHPPV]

One of the earliest reports on direct synthesis of PPV was by Gilch *et al*, where PPV was prepared by adding excess potassium tert-butoxide to *p*-xylylenedichloride [17]. This method, widely known as Gilch route, yielded insoluble polymer, since there were no substituents on the phenyl rings. Soluble conjugated members of PPV family (MEHPPV) are usually prepared using Gilch method [18]. Even though it is the easiest synthetic method for PPV, Gilch route has certain problems like the formation of microgels, partial solubility, formation of luminescence-quenching tolane units, high

polydispersities [19]. Various groups have attempted improving the Gilch route by addition of additives like benzyl halide [20] or phenolic derivatives [21] to reduce the gel formation. Changing the solvent of polymerization medium is shown to decrease the poly-dispersities and gel formation [22]. Becker *et al.* showed that, by using a sterically crowded monomer with alkyl chains protecting the benzylic carbon like an umbrella, it was possible to bring down the tolane units considerably [23].

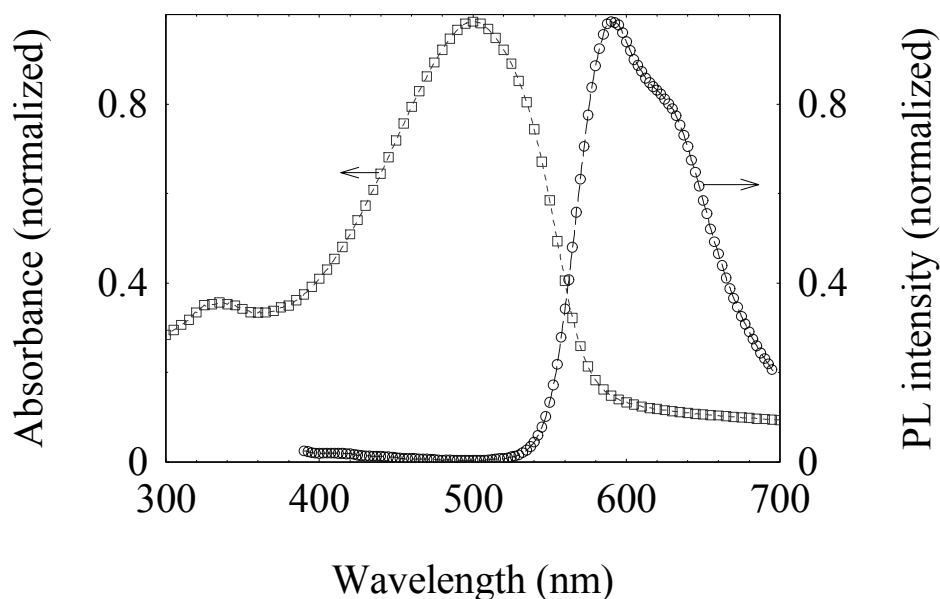


**Figure 2.8** Absorption ( $\square$ ) and photoluminescence (PL) ( $\circ$ ) spectrum for spin coated (thickness ( $t$ )  $\approx$  150 nm) MEHPPV polymer film on quartz substrates, excitation wavelength for PL was 500 nm.

MEHPPV used for studies, was synthesized by S. Ramakrishna et al using a novel methodology which provides a control of conjugation and hence the color of emission [24, 25] in this polymer. This approach relies on the random placement of thermally labile and inert groups on the precursor backbone followed by selective elimination of the labile group. The control of emission color was achieved by varying the mole-fraction of the thermally labile group in the precursor. The labile groups that have been utilized were acetate, xanthate and dithiocarbamate, while the inert one was a methoxy group [26]. MEHPPV with 100% conjugation length segments were used to carryout studies. Absorption and PL spectra are shown in **Figure 2.8**.

### 2.2.3 Poly ( dioctylfluorene-co-bithiophene ) (PFO – TT)

PFO-TT is derived from Poly(9,9-dioctylfluorene) (PFO). It has a rigid backbone, which results in a hairy-rod-like structure [27, 28]. High carrier mobilities and polarized photon emission are usually obtained when the conjugated polymer films are macroscopically ordered. For this reason, polyfluorenes and other self-aligning, liquid crystalline conjugated polymer semiconductors have attracted much recent attention [29, 30, 31].

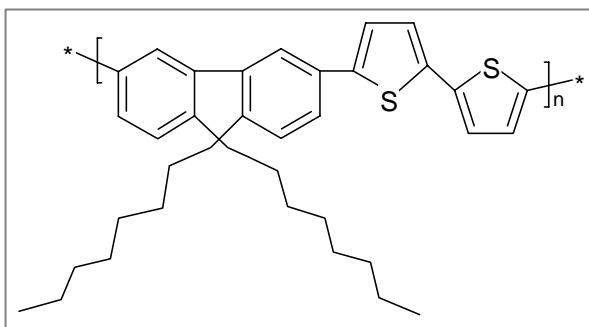


**Figure 2.9** Chemical structure for poly(dioctylfluorene-co-bithiophene) (PFO-TT or PF8T2)

Poly(9,9-dioctylfluorene-co-bithiophene) alternating copolymer (F8T2) has several characteristics that make it convenient for studying electrical characteristics of aligned polymer films: conjugated segments for charge transport, relatively good stability in air, and solubility in a wide range of solvents. Its chemical structure is shown in **Figure 2.9**. It also exhibits a thermotropic liquid crystal phase, since F8T2 is a main-chain liquid crystal polymer of the structure like a “hairy rod”. The octyl side chains protruding from the rod like backbone (hence the name “hairy rod”) facilitate solvation in organic solvents.

First attempts to synthesize soluble, processible poly(2,7-fluorene)s (PFs) via an attachment of a solubilizing substituent in the 9-position of the fluorene core, were published in 1989 by Yoshino and co-workers. They coupled 9,9-dihexylfluorene oxidatively with  $\text{FeCl}_3$  [32] and obtained low molecular weight poly(9,9-dihexylfluorene). The first transition-metal catalyzed coupling of 2,7-dibromo-9,9-dialkylfluorenes with Ni salt/zinc was described by Pei and Yang (Uniax Corp.) in 1996 [33]. Later on, a research group at DOW Chemical Corp [34] as well as eclerc and co –

workers [35] published the synthesis of 9,9-dialkylfluorenes following the Suzuki-type cross coupling [36] of 9,9-dialkylfluorenes-2,7-bisboronic acid or ester and 2,7-dibromo-9,9-dialkylfluorene monomers. 9,9-Dialkyl-PFs with alkyl side-chains containing more than 6 carbons are highly soluble in various organic solvents. They do not precipitate during the coupling reaction. The length and structure of alkyl substituents do not significantly vary the optical and electronic properties of the PFs in dilute solution, which indicates a negligible influence of the alkyl side chains on the electronic interaction between adjacent fluorine units. This is a consequence of the very favorable 9-position of alkyl substitution in 9,9-dialkyl-PFs, which is far away from the aryl-aryl coupled 2 and 7 positions. However, the structure of the alkyl side-chains strongly influence the solid-state packing of the polymers upon temperature treatment [37], upon exposing the film to solvent vapors [38], or upon treating the polymer with solvent/non-solvent mixture with increased quantity of nonsolvent [39].

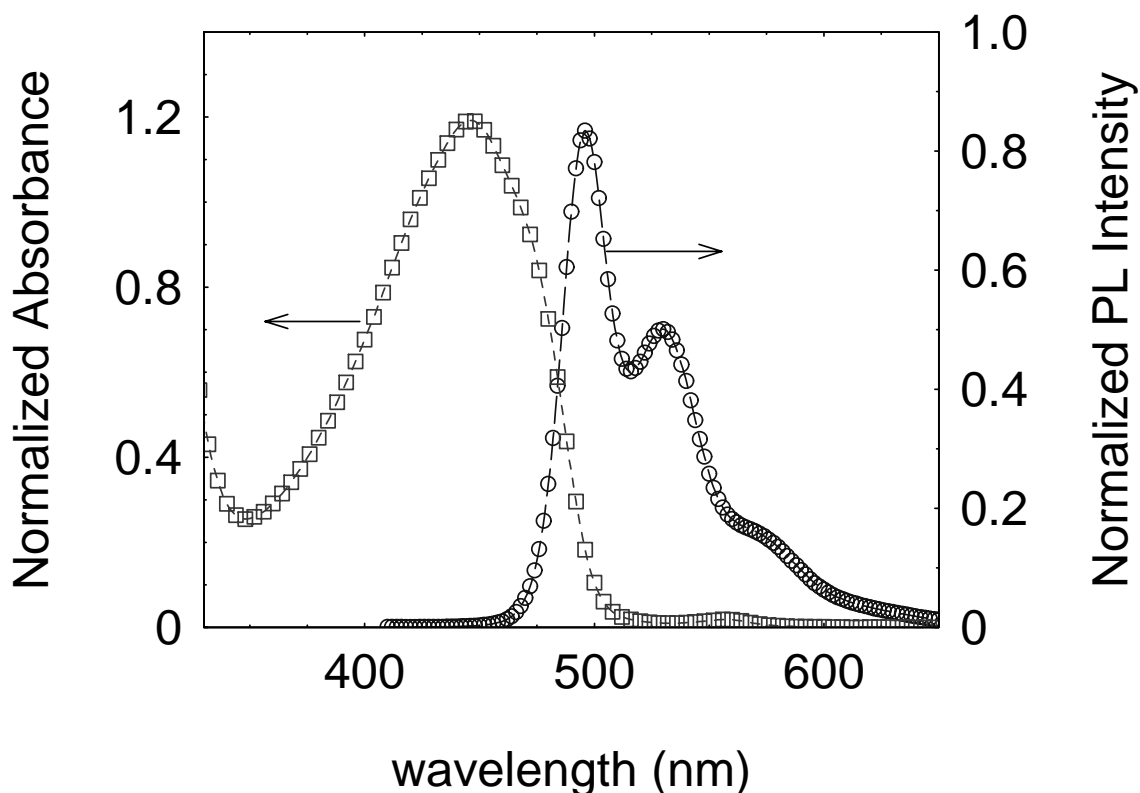


**Figure 2.10** Absorption (□) and photoluminescence (PL) (o) spectrum for spin coated PFO-TT polymer film on quartz substrates, excitation wavelength for PL was 470 nm.

### Polyimide (PI)

Polyimides are an interesting group of strong, astoundingly heat and chemical resistant polymers. Their strength, thermal and chemical resistance are high enough to replace glass and metals, such as steel, for many scientific industrial and academic applications. PI is an insulating elastomeric polymer, which has been extensively used in making waveguides structures for MOEMs, microfluidic devices, alignment layers for liquid crystalline polymers etc.

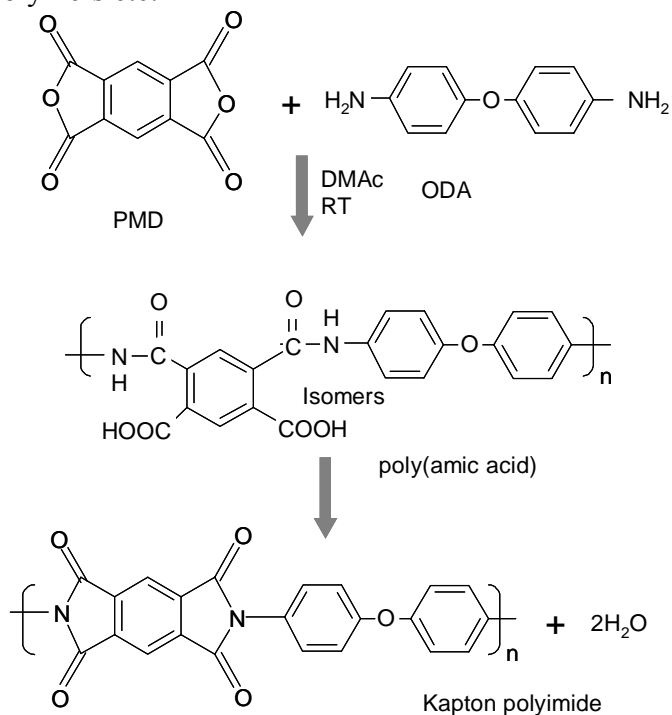


**Figure 2.11** Synthesis Scheme of Kapton polyimide

The most widely practiced procedure in polyimide synthesis is the two-step poly(amic acid) process. It involves reacting a dianhydride and a diamine at ambient conditions in a dipolar aprotic solvent such as N,N-dimethylacetamide (DMAc) or N-methylpyrrolidinone (NMP) to yield the corresponding poly(amic acid), which is then cyclized into the final polyimide. This process involving a soluble polymer precursor was pioneered by workers at Dupont in 1950's, and to this day, continues to be the primary route by which most polyimides are made. Most polyimides are infusible and insoluble due to their planar aromatic and hetero-aromatic structures and thus usually need to be processed from the solvent route. This method provided the first such solvent based route to process these polyimides. The process also enabled the first polyimide of significant commercial importance-'Kapton™', to enter the market. The process for most extensively developed Kapton™ polyimide utilizes the monomer pyromellitic dianhydride (PMDA) and 4,4'-oxydianiline (ODA). This process is illustrated in **Figure 2.11**.



## 2.3 Device Fabrication Process

There were primarily two kind of photovoltaic device structures used for the studies.

1. Two Terminal Device Structures
2. Three Terminal Device Structures

There were also additional structures used, which have been discussed in forthcoming chapters.

### 2.3.1 Two Terminal Device Structures

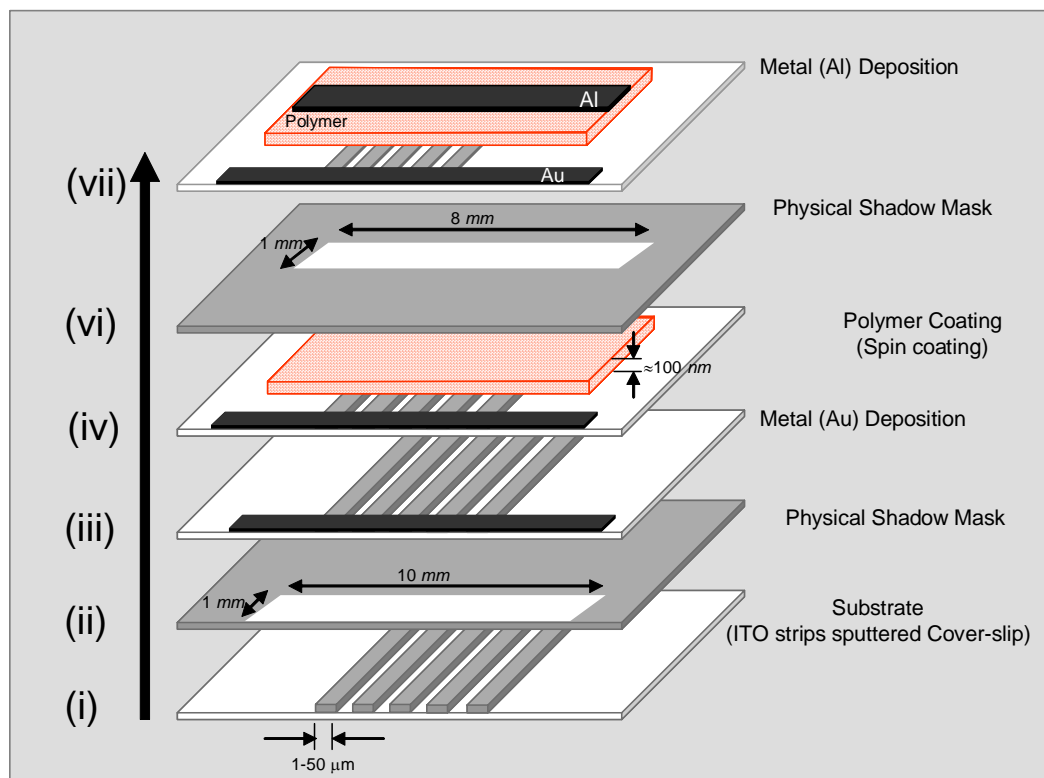


*Figure 2.12 Two terminal device fabrication process on pre-cleaned substrates*

These photovoltaic device structures were used to measure lateral diffusion transport length scales for photogenerated charge carriers. The device fabrication procedure can be divided into seven steps as shown in *Figure 2.12* (i) Substrates: electron beam sputtered patterned ITO strips coated glass cover-slips were used, The widths of ITO strips were

also very small (1 to 50  $\mu\text{m}$ ) with the similar order of spacing in between the strips. A routine wet cleaning procedure was used to clean the substrates. As the substrates were very thin (220  $\mu\text{m}$ ) and width of ITO strips were also small (1 – 50  $\mu\text{m}$ ), so special care was taken while handling these substrates. (ii) Physical shadow mask: As the ITO strips were very thin and it was difficult to access them individually for electrical contact, a common Au contact was made for all these strips. It was done using physical shadow mask technique, where the entire device substrate was covered except a small opening for metal deposition on the bottom part of ITO strips. (iii) Metal (Au) deposition: Samples were transferred into thermal evaporation chamber and Au electrode (1mm  $\times$  10 mm, perpendicular to ITO strips) was deposited under high vacuum conditions ( $\sim 10^{-6}$  mbar). The 99.99 % pure Au metal was procured from local gold refinery (iv) Polymer Coating: Conjugated polymers rr-P3HT ( $M_w \sim 87,000$ ) procured from Sigma-Aldrich Inc., MEHPPV ( $M_w \sim 145,500$ ), and PFO-TT ( $M_w \sim 19,300$ ) were used for device fabrications. These polymers were filtered, purified and dissolved in appropriate solvents (MEHPPV; P3HT, 10 g/L in  $\text{CHCl}_3$  solution and PFO-TT, 10 g/L in tetrahydrofuran solution) prior to spin coating on pre-cleaned substrates in an inert atmosphere (MBraun glove box). Thickness of polymer films obtained was in the range of 40 - 100 nm range. In case of P3HT devices, substrates were treated with Hexamethyldisilazane (Aldrich) to enrich surface quality. These polymer films were annealed at 70<sup>0</sup> C for 12 hours inside the glove box. (v) A physical shadow masking was done using teflon tape in order to coat top Al electrode deposition. (vi) The final Al metal coating was done by thermal evaporation technique using turbo molecular vacuum pump at high vacuum conditions ( $10^{-6}$  mbar). (vii) These devices were encapsulated by two methods; (a) an elastomeric polymer (PDMS) film coating on top of the active area of device. (b) a thin glass slide was used to encapsulate devices. The device encapsulation was done in inert atmosphere, in order to protect them from extrinsic chemical doping from ambient moisture and oxygen.

### 2.3.2 Three Terminal Device Structures

Three terminal device structures (see *Figure 2.1*) were fabricated in order to show the use of polymer semiconductors as an optical position sensitive detector. In this case, there is difference from the two terminal device structures in terms of patterned device substrates, instead of many ITO strips there were only two Cr-Au electrodes ( $Au_L$  &  $Au_R$ : 1 mm  $\times$  10 mm) on glass substrates. The interelectrode distance ( $L_{Au-Au}$ ) was kept in the range from 25  $\mu$ m to 10 mm using appropriate technique either photolithography or physical shadow mask technique. These device structures were made by drop casting of polymer, in order to get thicker polymer films ( $\approx$  700 nm), so that the Au electrodes do not short with top Al electrode, as shown in *Figure 2.13*.

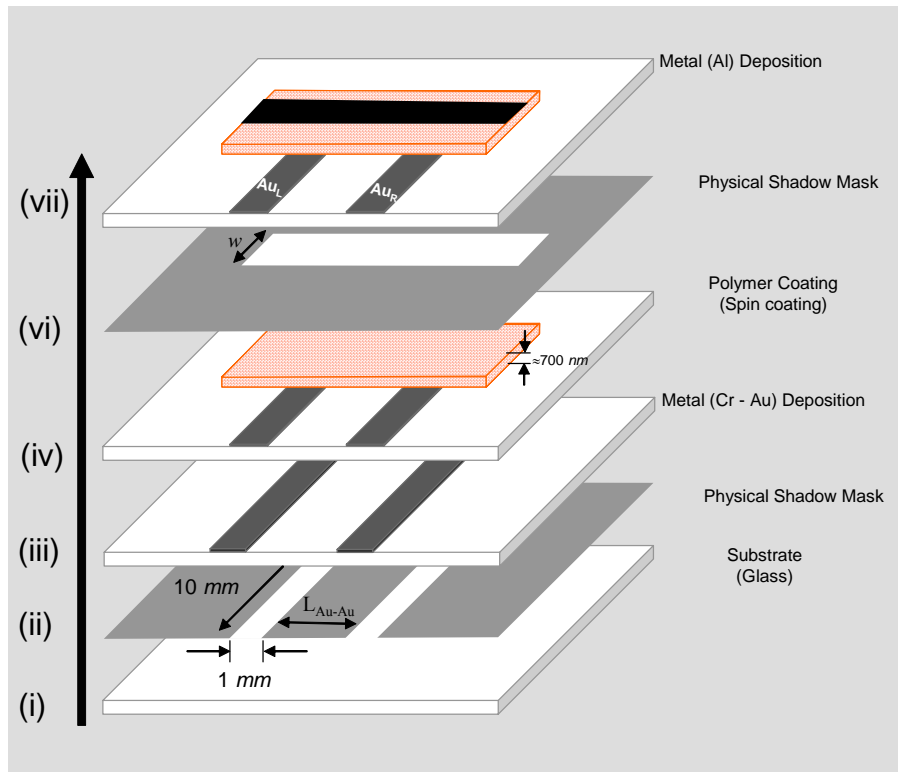


*Figure 2.13* Three terminal device fabrication process on pre-cleaned substrates

## 2.4 Experimental Techniques Used in Conjunction with the Devices

1. Photocurrent Modulation Spectroscopy
2. I-V measurement setup
3. DC Transient Measurement
4. Temperature Dependent Cryo-state setup
5. Scanning Electron Microscope
6. Spatial Photocurrent Profile Setup
7. Optical Scanning Probe Microscopy
  - i). Confocal Microscope
  - ii). Wide Field Optical Microscope

### 2.4.1 Intensity Modulated Photocurrent Spectroscopy

Photocurrent spectroscopy is an important tool to reveal the nature of charge species (whether they are free carriers or from sub bandgap levels) involved in photoconduction. This spectra provides an insight physics of devices such as electric field distribution, diffusion length of charge carriers, wavelength dependent charge generation efficiency. These measurements were carried out on (ITO or Au)/ polymer/ Al based device structures using lock-in technique. A chopped (20 cycles/sec. to 4 kilocycle/sec.) monochromatic light was used as an excitation source and photocurrent was measured using lock-in amplifier (SRS 830) at chopper frequency as reference. This technique gives very high signal– to- noise ratio as it cuts out all stray light and dark conduction from measured photosignal so results in a true wavelength dependent photoresponse of specimen. A standard experimental setup is shown in *Figure 2.14*. In case of liquid crystalline semiconducting polymer, a polarizer was introduced to carryout polarization dependent photocurrent spectroscopy. Irradiated light was polarized parallel and perpendicular to aligned chain direction and photocurrent was measured using lock-in technique.

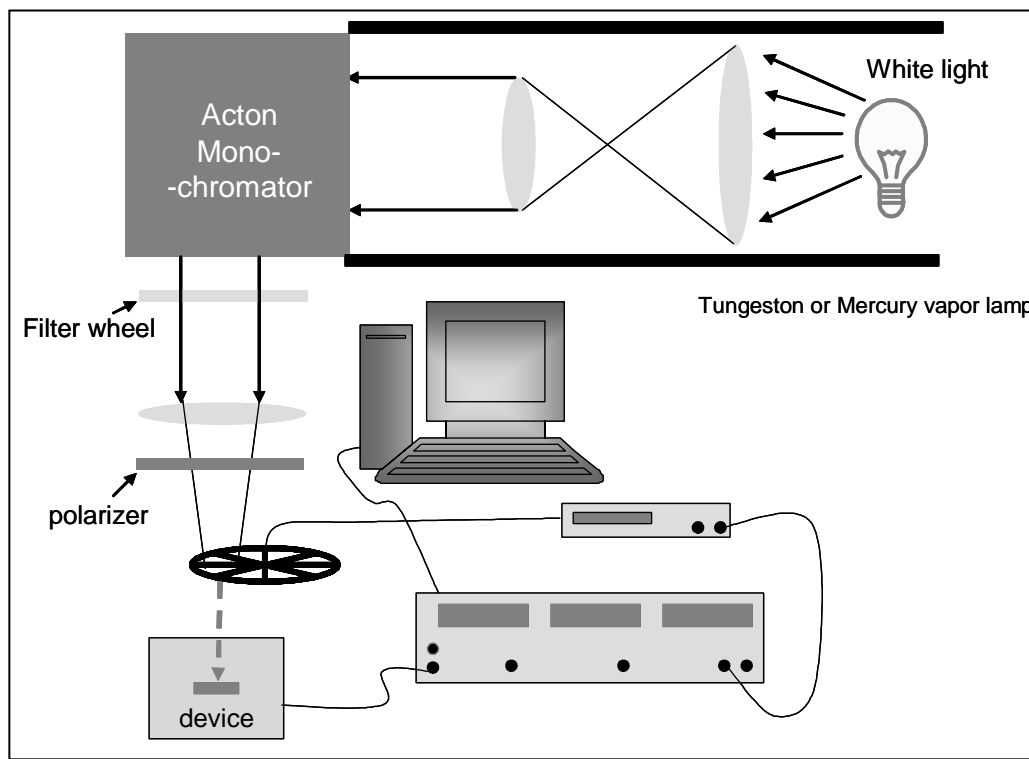


*Figure 2.14 Intensity modulated photocurrent spectroscopy setup*

## 2.4.2 I-V Measurement Setup

Semiconductor/metal interface properties can be determined by I-V measurements. There were different combinations of semiconducting polymers and metals used as follows (i) Au/polymer/Au, (ii) Au or ITO/polymer /Al (iii) Au/ polymer /ITO. The I-V characteristics were carried out using a Keithley source meter and Kiethley electrometer on Ohmic and Schottky type interfaces. A schematic of experimental setup is shown in *Figure 2.15*. Different bias range was used according to surface and sandwich device structures, as discussed in metal/polymer interface section of Chapter 1.

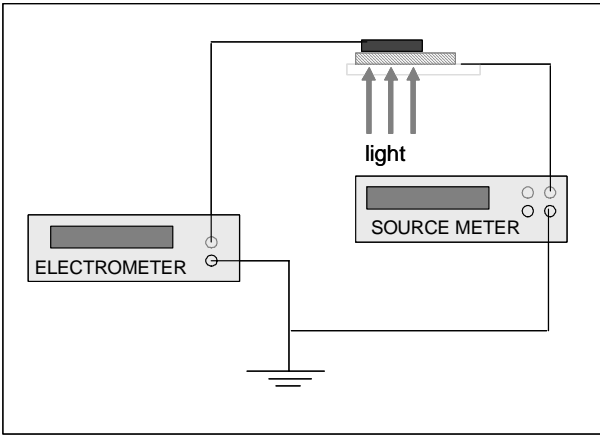


**Figure 2.15** Standard dark and with light I-V measurement setup

### 2.4.3 DC transient Measurement Setup

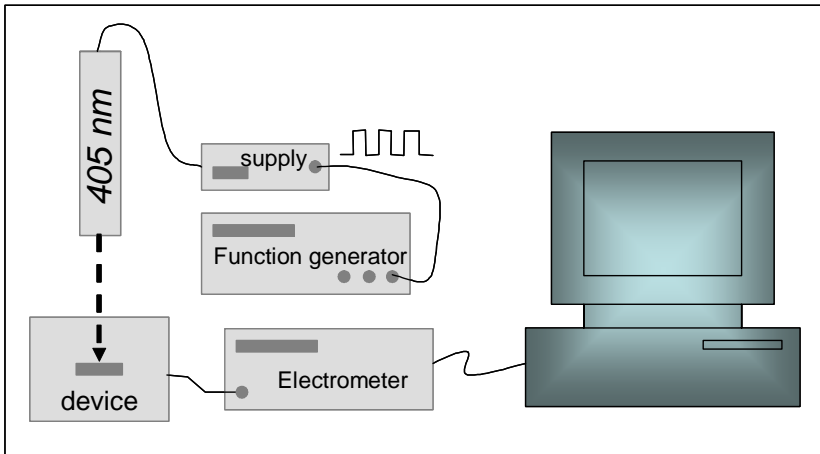


**Figure 2.16** DC transient measurement setup

As the signal levels were small on account of the spatially restricted illumination (optical power  $\sim 40$  nW, GaN diode laser,  $\lambda = 405$  nm, beam spot diameter  $\sim 320$  nm), conventional transient measurements using a large bandwidth CRO to resolve the small transients in the sub-microsecond regime, was not feasible. A high impedance ( $10^{14} \Omega$ ) electrometer (Keithely 6512), which has a large integration time constant was used to carry out the measurements in the low time-resolution range using a pulse laser source. Typical experimental setup is shown in **Figure 2.16**.

### 2.4.4 Temperature Dependent Measurement Setup

Semiconductor physics strongly depends upon temperature, as it has direct implication in charge generation and charge transport. In polymer semiconductors, a single universal model cannot explain temperature dependence on charge generation and transport. A qualitative picture about both these processes exist, however, exact explanation of the experimental data still remains a challenge.

The temperature dependent photocurrent measurements were carried out using cryostate (LakeShore Model 330 auto-tuning temperature controller) in the range of 70 K to 300 K. The sample was mounted on copper cold finger and measurements were taken in  $10^{-3}$  mbar vacuum conditions. The particular chamber was having optical quartz window for optoelectronic measurements. In this case light source (He-Ne laser,  $\lambda = 633$  nm, beam spot  $\approx 100\mu\text{m}$ ) was mounted on a NEWPORT ESP100 piezo-controlled linear translational stage, which has a scan range of 25 mm with a minimum step of 100 nm. It was interfaced through RS232 cable with computer. The  $I_{ph}(x, T)$  measurements were done using lock-in technique (SRS 230 dual channel) at mechanical chopper frequency as reference. These all instruments were controlled by LAB View program using GPIB and RS232 interface with national instrument card.

### 2.4.5 Electron Microscopy

Scanning electron microscopy (SEM) and field emission scanning electron microscopy (FESEM) were used to characterize patterned ITO device substrates prior to use for devices. SEM was used for ITO strips patterned on cover-slip glass to confirm sharp edge of electron beam sputtered ITO strips. Along with SEM image, electron beam diffraction was also carried out on ITO and non-ITO part of substrates to reveal the quality of used substrates. FESEM was used to characterize the ITO substrates, which were used for optical and electrical anisotropy measurements.

### 2.4.6 X-ray Diffraction (XRD) and Grazing Incidence X-ray Diffraction (GIXRD) Measurements

The ordering and self-assembly of pristine P3HT film atop HMDS-treated glass plate was verified using conventional X-ray diffraction (XRD) and grazing incidence X-ray diffraction (GIXRD) techniques. As expected, no significant ordering was observed in XRD technique. But in GIXRD measurement (in plane), a peak at  $2q \gg 5^\circ$  ( $q$  is the angle of incidence), representing the (100) plane, was observed. The GIXRD measurement was conducted in CCMR, Cornell University, USA.

### 2.4.7 Spatial Photocurrent Measurement Setup

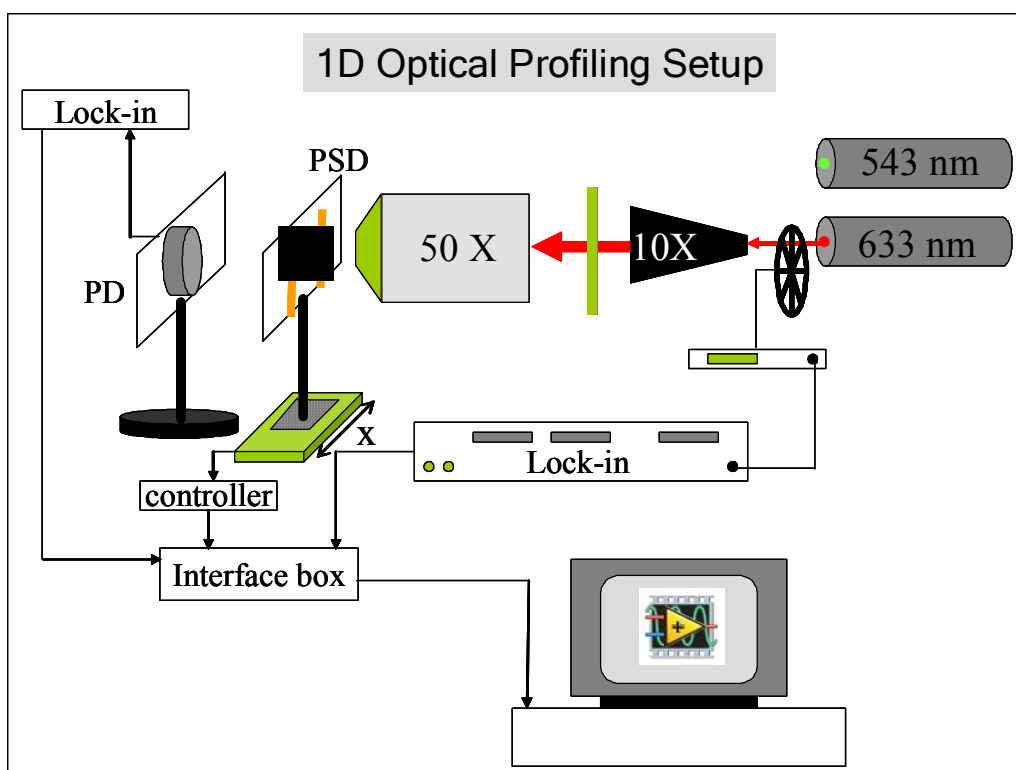


**Figure 2.17** 1D optical profiling setup used for simultaneous transmission and photocurrent measurements using lock-in technique.

A local optical probe was used for linear spatial photocurrent profiling on active conjugated polymer based device structures. This typical experimental setup (see **Figure**



2.17) was designed in our laboratory to understand optoelectronic properties such as metal/ polymer interfacial dynamics, electric field distribution (necessary for efficient exciton dissociation), photoinduced charge carrier transport and optical sectioning of polymer film according to penetration depth of excitation light source ( $1/\text{absorption coefficient } (\alpha(\lambda))$ ).

In these measurements, transmission and photocurrent profiles were recorded simultaneously using lock-in technique with a local chopped optical probe (spot diameter  $\leq 1 \mu\text{m}$ , optical power  $\approx 1 \mu\text{W}$ ,  $\lambda = 405 \text{ nm}, 473 \text{ nm}, 543 \text{ nm}, 633 \text{ nm}$ ). Transmission profiles were recorded using high sensitivity Si photodiode. The polymer device was mounted on a piezocontrolled linear translation stage (NEWPORT ESP100, range = 25 mm, minimum step-size = 100 nm).

#### 2.4.8 Optical Scanning Probe Microscopy

Advances in material research require increasingly powerful analytical techniques with regard to spatial resolution and sensitivity. Optical scanning probe microscopy has several advantages over other existing microscopy techniques. The reasons: (i) it is non-destructive technique. (ii) It is at atmospheric pressure in ambient. (iii) It is a material specific probe (light wavelength). (iv) It has high spatial resolution ( $\sim 10 \text{ nm}$  using aperture less probe in near field regime). (v) There are simultaneously optical and electrical measurements. (vi) The spectroscopy is with very high resolution  $\rightarrow$  (a) to study single quantum structures (i.e., dots, wires, particles) or single molecule chromophores (b) to reduce background emission when studying these small objects (c) to gain access to the selection rules associated with evanescent optical modes. This technique has been used in versatile scientific research laboratories as a very powerful tool to study a wide range of materials. There are three optical scanning microscopy techniques, which are relevant to the present studies:

- I. Near Field Scanning Optical Microscopy
- II. Confocal Scanning Optical Microscopy
- III. Wide field Scanning Optical Microscopy

Even though a conventional NSOM technique was not used, it is instructive to spell out the details and the implication of this method.

**Table 2.1** Commercially available presently achievable resolution in optical microscopes [40]

Microscopy	xy-resolution ( $\mu\text{m}$ )	z resolution ( $\mu\text{m}$ )
Standard microscope	$\sim 0.5$	$\sim 1.6$
Confocal/ two-photon	$\sim 0.25$	$\sim 0.7$
Near-field imaging	$\sim 0.05$	$\sim 0.01$

**Near Field Scanning Optical Microscopy (NSOM)**

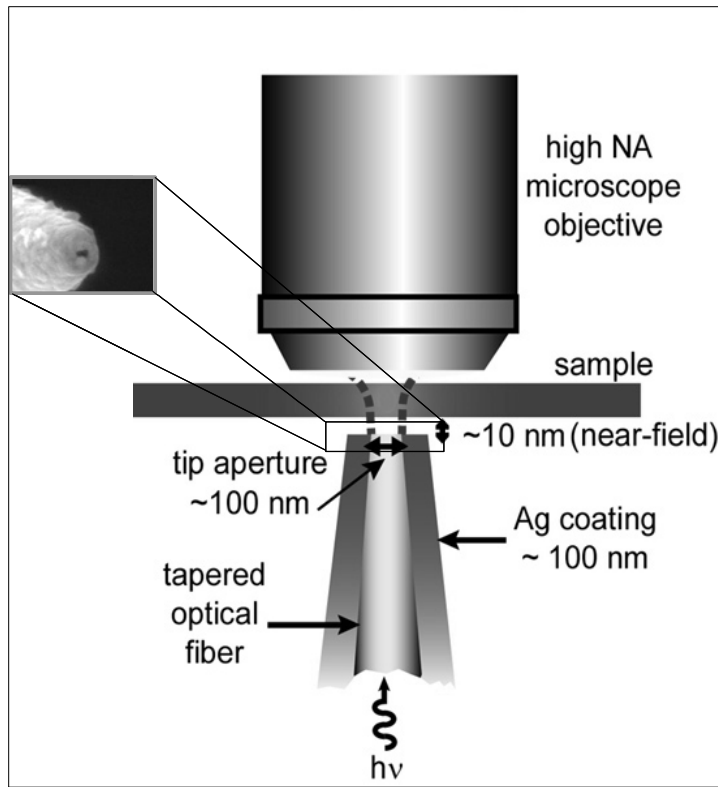


**Figure 2.18** Schematic of near field optical geometry with SEM of cross sectional view of typical tapered optical fiber tip

Edward H. Syngé published a series of articles that first conceptualized the idea of an ultra-high resolution optical microscope in early 1928. Syngé's proposal suggested a new type of optical microscope that would bypass the diffraction limit, but required fabrication of a 10-nanometer aperture (much smaller than the light wavelength) in an

opaque screen. A stained and embedded specimen would be optically flat and scanned in close proximity to the aperture. While scanning, light illuminating one side of the screen and passing through the aperture is confined by the dimensions of the aperture, and used to illuminate the specimen before undergoing diffraction. As long as the specimen remained within a distance less than the aperture diameter, an image with a resolution of 10 nanometers could be generated.

A typical schematic near field geometry is shown in *Figure 2.18*. In addition, Synge accurately outlined a number of the technical difficulties in building a near-field microscope. These included the challenges of fabricating the minute aperture, achieving a sufficiently intense light source, specimen positioning at the nanometer scale, and maintaining the aperture in close proximity to the specimen. The proposal, although visionary and simple in concept, was far beyond the technical capabilities of the time. Experimental verification of the feasibility of Synge's proposals had to wait until 1972 when E. A. Ash and G. Nicholls demonstrated the near-field resolution of a sub-wavelength aperture scanning microscope operating in the microwave region of the electromagnetic spectrum. Utilizing microwaves, with a wavelength of 3 centimeters, passing through a probe-forming aperture of 1.5 millimeters, the probe was scanned over a metal grating having periodic line features. Both the 0.5-millimeter lines and 0.5-millimeter gaps in the grating were easily resolvable, demonstrating sub-wavelength resolution having approximately one-sixtieth (0.017) the period of the imaging wavelength. Extension of Synge's concepts to the shorter wavelengths in the visible spectrum presented significantly greater technological challenges (in aperture fabrication and positioning), which were not overcome until 1984 when a research group at IBM Corporation's Zurich laboratory reported optical measurements at a sub-diffraction resolution level. An independent group working at Cornell University took a somewhat different approach to overcome the technological barriers of near-field imaging at visible wavelengths. The IBM researchers employed a metal-coated quartz crystal probe on which an aperture was fabricated at the tip, and designated the technique scanning near-field optical microscopy (SNOM). The Cornell group used electron-beam lithography to

create apertures, smaller than 50 nanometers, in silicon and metal. The IBM team was able to claim the highest optical resolution (to date) of 25 nanometers, or one-twentieth of the 488-nanometer radiation wavelength, utilizing a test specimen consisting of a fine metal line grating. Although the achievement of non-diffraction-limited imaging at visible light wavelengths had demonstrated the technical feasibility of the near-field aperture scanning approach, it was not until after 1992 that the NSOM began to evolve as a scientifically useful instrument. This advance in utility can be primarily attributed to the development of shear-force feedback systems and to the employment of a single-mode optical fiber as the NSOM probe, both of which were adapted for the near-field technique by Eric Betzig while working at AT&T Bell Laboratories.

### **Laser Confocal Scanning Microscope (LCSM)**

LCSM has a particular advantage over conventional microscopy. In laser scanning optical microscopy, the specimen is scanned by a diffraction-limited spot of laser light. Light transmitted or reflected by the in-focus illuminated volume element of the specimen, or the fluorescence emission excited within it by the incident light, is focused onto a photodetector. In the confocal mode, an aperture, usually smaller in diameter than the Airy disc image, is positioned in the image plane in front of the detector, at a position confocal with the in-focus volume of element. A schematic of confocal setup is shown in *Figure 2.19*. Light emanating from this in-focus volume of element thus passes through the aperture to the detector, while that from any region above or below the focal plane is defocused at the aperture plane and thus largely prevented from reaching the detector, contributing essentially nothing to confocal image. It is this ability to reduce out-of focus blur, and thus permit accurate non-invasive optical sectioning, that makes confocal scanning microscopy so well suited for the imaging and three-dimensional tomography of 3D photonic integrated circuits, polymer blends and stained biological samples. There are currently two alternative methods to confocal microscopy that are in use for producing optical sections: deconvolution and multiphoton

imaging. They differ technically, but like confocal methods, are based on the conventional optical microscope. Deconvolution uses computer-based algorithms to calculate and remove out-of-focus information from fluorescence images. Due to more efficient algorithms and much faster mini computers, this technique has become a practical option for imaging. Multiphoton microscopy uses the same scanning system as the LCSM, but does not require the pinhole aperture at the detector. The pinhole is unnecessary as laser excites the

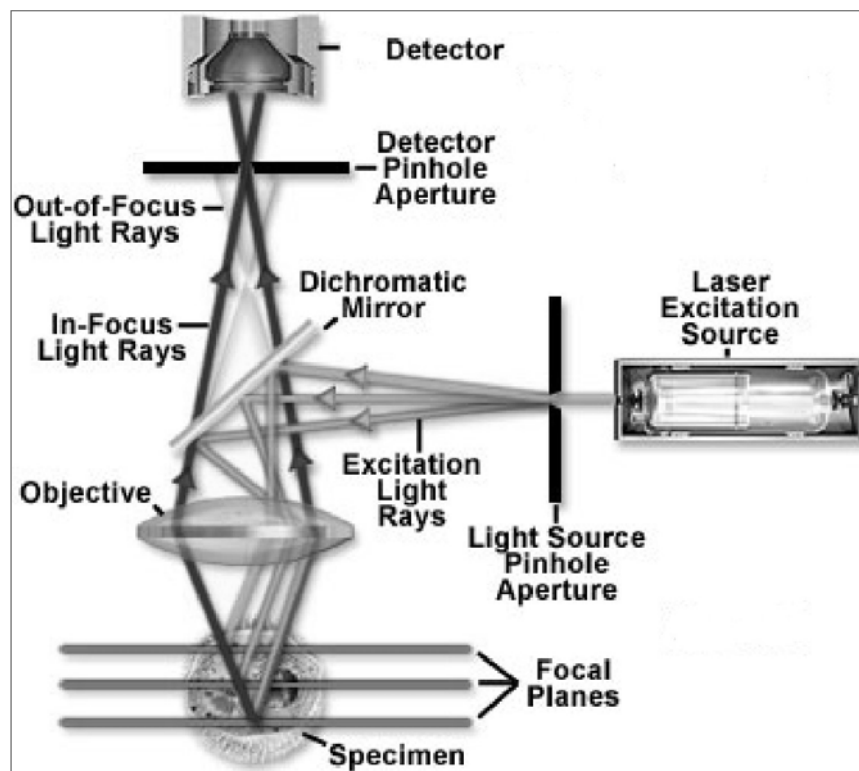


*Figure 2.19 Schematic of Confocal microscope setup*

fluorochrome label only at the point of focus, eliminating the out-of-focus emission. An additional benefit in the imaging of living tissues is that photobleaching is reduced in the specimen due to the reduced energy absorbed from the laser beam.

## Wide (or Far) Field Optical Scanning Microscope

In practice, scanning of the laser beam can be conveniently brought either by

- (i) The lateral movement of the specimen in the focal plane relative to a stationary optical path (scanned stage SOM).
- (ii) The angular movement of the illuminating beam filling the back focal plane of a stationary objective, which causes the focused light beam to move laterally in the focal plane relative to the stationary specimen (scanned beam SOM).

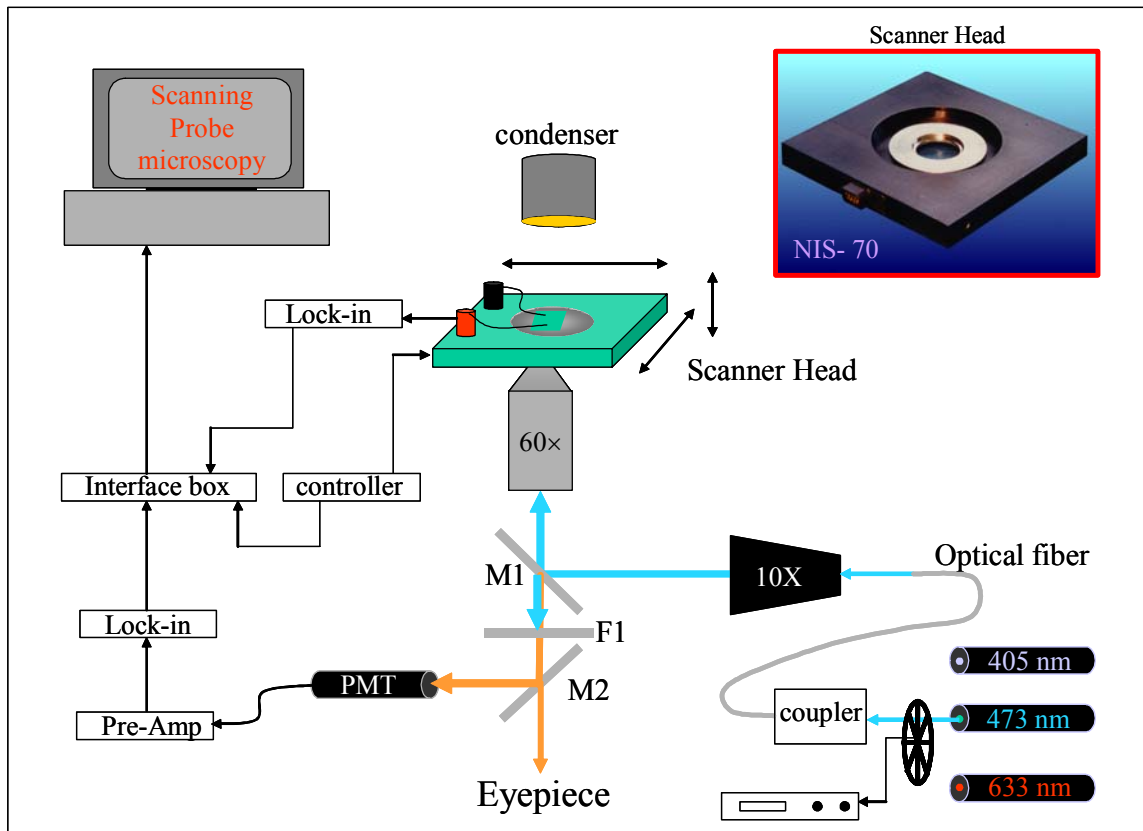


*Figure 2.20 Home built wide-field optical microscope setup*

Scanned stage SOM, first developed by Sheppard and his colleagues [41], has been the method used for most prototype SOMs built in research laboratories [42]. It has an

important advantage of constant axial illumination, thus reducing optical aberrations and ensuring complete evenness of optical response across the entire scanned field (space-invariant imaging), a feature desirable for optimal image quality and ease of subsequent image processing. In addition, it permits scanned fields of view much larger than the static field of view of the objective employed. This allows one to change between very low and very high magnification imaging while maintaining optimal resolution and light-collection, by the simple expedient of altering the stage scan amplitude while using a single high-magnification objective of high numerical aperture.

In order to carryout photocurrent contrast microscopy on conjugated polymer based thin film devices, a wide field optical microscope was assembled around a NIKON TE-2000 inverted microscope during the course of Ph.D., as shown in *Figure 2.20*. Scanner head (NIS-70) was procured from Nanonics along with scanning software (Nanoview 2.2v). This scanner head (dimension 7 cm  $\times$  7 cm  $\times$  0.5 cm, with a circular optical opening) has scanning range 70  $\mu$ m in all the three directions with minimum step size of subnanometer. A piezocontroller (manually (internal mode) or through software (external mode)) and interface box solve the purpose of choice scanning area. This interface box records data corresponds to each x-y position simultaneously from 4-channels. These four scan can be simultaneous photocurrent, transmission, photoluminescence and morphology (it can be changed as per requirement of experiment). In general, there were two channels used to carryout experiments in our laboratory, a simultaneous measurement of photocurrent and reflected excitation light using lock-in technique. The reflected light was collected using camera port where a high sensitivity photomultiplier tube (PMT, Burlie) (for PL in infrared region we procured PdSe based photoconductor from Hamamtsu, Japan, external circuit and detector mount was designed locally) was mounted. Photodetector signal was amplified using pre-amplifier (EG&G) prior to amplify the weak signal and it also helps in protection of lock-in amplifier from high voltage supply used for PMT. A single mode optical fiber (core diameter = 4  $\mu$ m) was used along with 10 $\times$  beam expander to illuminate backside of high N.A. (numerical aperture) microobjective lens (magnification 60 $\times$ , working distance 150

$\mu\text{m}$  with coverslip correction ring). Mercury lamp port was used for guiding the light coming from optical fiber. The motive behind using single mode fiber was use to different excitation wavelength without disturbing the crucial optical alignment, which will not change the position of optical beam on specimen (very useful in case of polymer blends [43]). Laser wavelengths (405 nm, 470 nm, 543 nm, 633 nm), specific dielectric layers coated dichroic mirrors and filters were procured from CHROMA to use this setup for wide range of scientific problems.

## 2.5 Advantage of Photocurrent Microscopy

In photocurrent microscopy a focused laser beam illuminates locally the surface of sample and photogenerated charge carriers give the photocurrent in output circuit as a function of position of light spot in a two dimensional plane. For disordered-semiconducting film studies, there are particular benefits of opto-electric measurements over only optical measurements, such as photocurrent images show the function at electro-active areas, where as the optical images (which depict the surface reflectivity) primarily depicts the topography. Lower wide field optical resolution can be tolerated as low as 10 nm in diameter, cylindrical object down to 2- 5 nm in diameter, and image films with subnanometer resolution. Molecular film imaging and nonlabeled single nano-object detection becomes possible with a technique combining the conviviality of an optical microscope with molecular sensitivity [44]. In particular optoelectronic (organic or inorganic) thin film devices can be characterized with high resolution using this tool to make a connection of material parameters with device performance [45, 46].

In particular polymer bulk hetero-junction solar cells, where donor – acceptor polymers do not mix suitably because of their low entropy and get phase segregate during the spin- coating process into separated coexisting domains, have been studied by many research groups [47,43]. This phase segregation can be controlled by varying spin coating parameters such as speed, atmospheric conditions, solution, and substrate temperature and annealing conditions after spin coating, allowing for device optimization. As mentioned earlier, intimate mixing of these polymers provides a pre-requisite for good



interpenetrating structure, which provides both efficient charge transfer and efficient charge transport. In case of thin film transistors, a local injection of photocarriers at a distance with respect to drain or source electrode can give direct estimate of contact resistance versus bulk resistance contribution. At the same time suitable wavelength selection of probe beam can give charge carrier profiling in transverse plane [48, 49]. The parameters like charge carriers transport lengths, exciton diffusion length, effect of gate bias can lead to an ultimate understanding of device operation and device material characteristics. In our laboratory all these measurements are actively carried out as an effective characterization tool for variety of polymers and devices made up of these polymeric materials. [1, 43, 50].

## References

---

- [1] D. Kabra, K. S. Narayan, *Adv. Mater.* 2007 (in press)
- [2] D. Kabra, Th. B. Singh, K. S. Narayan, *Appl. Phys. Lett.* **85**, 5073 (2004)
- [3] D. Kabra, S. Sriram, N. S. Vidhyadhiraja, K. S. Narayan, *J. Appl. Phys.* **101**, 64510 (2007)
- [4] K. Y. Jen, R. Oboodi, and R. L. Elsenbaumer, *Polym. Mater. Sci. Eng.* **53**, 79 (1985)
- [5] R. D. McCullough, *Adv. Mater.* **10**, 93 (1998)
- [6] R. D. McCullough, R. D. Lowe, *J. Chem. Soc., Chem Commun.* **70**, 1992
- [7] R. D. McCullough, R. D. Lowe, M. Jayaram, D. L. Anderson, *J. Org. Chem.* **58**, 904 (1993)
- [8] P. Bauerle, F. Pfau, H. Schlupp, *J. Chem. Soc. Perkin Trans. II* **489**, 1993
- [9] I. B. Berlman, *J. Phys. Chem.* **74**, 3085 (1970)
- [10] (a) J. K. Herrema, J. Wildeman, F. Vanbolhuis, G. Hadziioannou, *Synth. Met.* **60**, 239, (1993)
- (b) H. Mao, B. Xu, S. Holdcraft, *Macromolecules* **26**, 1163 (1993)
- [11] A. Stabel, J. P. Rabe, *Synth. Met.* **67**, 47 (1994)
- [12] T. A. Chen, X. Xu, R. D. Rieke, *J. Am. Chem. Soc.* **117**, 233 (1995)
- [13] A. Salleo, M. L. Chabinyc, M. S. Yang, R. A. Street, *Appl. Phys. Lett.* **81**, 4383 (2002).
- [14] B. D. Vogt, C. L. Soles, H. J. Lee, E. K. Lin, W. Wu, *Polymer* **46**, 1635 (2005).
- [15] W. Pisula, A. Menon, M. Stepputat, I. Lieberwirth, U. Kolb, A. Tracz, H. Sirringhaus, T. Pakula, and K. Müllen, *Adv. Mat.* **17**, 684 (2005).
- [16] E. M. Conwell, J. Perlstrin, S. Shaik, *Phys. Rev. B* **54**, R2308 (1996)
- [17] Stalmach, U. Dissertation Thesis, University of Mainz, 1996
- [18] F. Wudl, P. M. Allemand, G. Srdanov, Z. Ni, D. McBranch, *ACS Symp. Ser.* **455**, 683 (1991)
- [19] H. Becker, H. Spreitzer, K. Ibrom, W. Kreuder, *Macromolecules* **32**, 4925 (1999)
- [20] (i) B. R. Hsieh, Y. Yu, E. W. Forsythe, G. M. Schaaf, W. A. Feld, *J. Am. Chem. Soc.* **120**, 231 (1998)

- 
- (ii) B. R. Hsieh, Y. Yu, A. C. VanLaeken, H. Lee, *Macromolecules* **30**, 8094 (1997)
- (iii) B. P. Parekh, A. A. Tongonan, S. S. Newaz, S. K. Sanduja, A. Q. Ashraf, R. Krishnamoorti, T. R. Lee, *Macromolecules* **37**, 8883 (2004)
- [21] (i) C. J. Neef, J. P. Ferraris, *Macromolecules* **33**, 2311 (2000)
- (ii) Z. K. Chen, J. Q. Pan, Y. Xiao, N. H. S. Lee, S. J. Chua, W. Huang, *Thin Solid Films* **363**, 98 (2000)
- [22] B. P. Parekh, A. A. Tongonan, S. S. Newaz, S. K. Sanduja, A. Q. Ashraf, R. Krishnamoorti, T. R. Lee, *Macromolecules* **37**, 8883 (2004)
- [23] (i) H. Spreitzer, H. Becker, E. Kluge, W. Kreuder, H. Schenk, R. Demandt, H. Schoo, *Adv. Mater.* **10**, 1340 (1998)
- (ii) H. Becker, H. Spreitzer, W. Kreuder, E. Kluge, H. Schenk, I. Parker, Y. Cao, *Adv. Mater.* **12**, 42 (2000)
- [24] R. Gowri, D. Mandal, B. Shivkumar, S. Ramakrishnan, *Macromolecules* **31**, 1819 (1998)
- [25] G. Padmanaban, S. Ramakrishnan, *J. Am. Chem. Soc.* **122**, 2244 (2000).
- [26] G. Padmanaban, K. Nagesh, S. Ramakrishnan, *J. Poly. Sci. A* **41**, 3929 (2003)
- [27] U. Schref, E. J. W. List, *Adv. Mat.* **14**, 477 (2002)
- (b) L. R. Pattison, A. Hexemer, E. J. Kramer, S. Krishnan, P. M. Petroff, D. A. Fischer, *Macromolecules* **39**, 2225 (2006)
- [28] M. Knaapila, K. Kisko, B. P. Lyons, R. Stepanyan, J. P. Foreman, O. H. Seeck, U. Vanio, L. -O. Palsson, R. Serimaa, M. Torkkeli, A. P. Monkman, *J. Phys. Chem. B* **108**, 10711 (2004)
- [29] H. Sirringhaus, R.J. Wilson, R. H. Friend, M. Inbasekaran, W. Wu, E. P. Woo, M. Grell, D. D. C. Bradley, *Appl. Phys. Lett.* **77**, 406 (2000)
- [30] L. Kinder, J. Kanicki, P. Petroff, *Synth. Met.* **146**, 181 (2004)
- [31] F. C. Grozema, T. J. Savenije, M. J. W. Vermeulen, L. D. A. Siebbeles, J. M. Warman, A. Meisel, D. Neher, H. -G. Nothofer, U. Scherf, *Adv. Mat.* **13**, 1627 (2001)
- [32] M. Fukuda, K. Sawada, K. Yoshino, *J. Polym. Sci. A: Polym. Chem.* **31**, 2465 (1993)
- [33] Q. B. Pei and Y. Yang, *J. Am. Chem. Soc.* **118**, 7416 (1996)

- 
- [34] (i) E. P. Woo, M. Inbasekaran, W. Shiang, G. R. Roof, *International Patent Application WO97/05184*, 1997 [*Chem. Abs.* **126**, 225 700y (1997)]  
(ii) M. T. Bernius, M. Inbasekaran, J. O`Berien, W. S. Wu, *Adv. Mat.* **12**, 1737 (2000)
- [35] M. Ranger and M. Leclerc, *Macromolecules* **30**, 7986 (1997)
- [36] H. –G. Nothofer, A. Meisel, T. Miteva, D. Neher, M. Forster, M. Oda, G. Lieser, D. Sainova, A. Yasuda, D. Lupo, W. Knoll, U. Scerf, *Macromol. Symp.* **154**, 139 (2000)
- [37] A. J. Cadby, P. A. Lane, H. Mellor, S. J. Martin, M. Grell, C. Giebeler, D.D.C. Bradley, M. Wohlgenannt, C. An, Z. V. Vardeny *Phys. Rev. B* **62**, 15604 (2000)
- [38] M. Grell, D. D. C. Bradley, X. Long, T. Chamberlain, M. Inbasekaran, E. Woo, M. Soliman, *Acta. Polym.* **49**, 439 (1998)
- [39] H. G. Nothofer, Ph.D. thesis, University Potsdam, Germany 2001, Logos Verlag, Berlin, 2001, ISBN 3-89722-668-5
- [40] A. Lewis, H. Taha, A. Strinkovski, A. Manevitch, A. Khatchatouriants, R. Dekhter, E. Ammann, *Nature Bio. Tech.* **21**, 1378 (2003)
- [41] (i) C. J. R. Sheppard, A. Choudhury, *Optica Acta* **24**, 1051 (1977)  
(ii) C. J. R. Sheppard, T. Wilson, *Optica Acta* **25**, 315 (1978)  
(iii) T. Wilson, *Appl. Phys.* **22**, 119 (1980)  
(iv) T. Wilson, *Scanning* **7**, 79 (1985)  
(v) C. J. R. Sheppard, *Adv. Opt. Electron Microsc.* **10**, 1 (1987)
- [42] R. W. Wijnaendts van Resandt, H. J. B. Marsman, R. Kaplan, J. Davoust, E. H. K. Stelzer, R. Stricker, *J. Microsc.* **138**, 29 (1985)
- [43] D. Gupta, D. Kabra, K. Nagesh, S. Ramakrishanan, K. S. Narayan, *Adv. Func. Mat.* **17**, 226 (2007)
- [44] D. Ausserre, M.-P. Valignat, *Nanoletters* **6**, 1384 (2006)
- [45] (i) Y. Ahn, J. Dunning, J. Park, *Nanoletters* **5**, 1367 (2005)  
(ii) K. Balasubramanian, M. Burghard, K. Kern, M. Scolari, A. Mews, *Nanoletters* **5**, 507 (2005)
- [46] K. Karrai, G. kolb, G. Abstreiter, A. Schmeller, *Ultramicroscopy* **61**, 299 (1995)

- [47] A. C. Arias, J. D. MacKenzie, R. Stevenson, J. J. M. Halls, M. Inbasekaran, E. P. Woo, D. Richards, R. H. Friend, *Macromolecules* **34**, 6005 (2001)
- (ii) C. R. McNeill, H. Frohne, J. L. Holdsworth, P. C. Dastoor, *Nanoletters* **4**, 2503 (2004)
- [48] S. Dutta, K. S. Narayan, *Appl. Phys. Lett.* **87**, 193505 (2005)
- [49] M. Breban, D. B. Romero, S. Mezheny, V. W. Ballarotto, E. D. Williams, *Appl. Phys. Lett.* **87**, 203503 (2005)
- [50] D. Kabra, S. Sriram, N. S. Vidhyadhiraja, K. S. Narayan, *J. Appl. Phys.* **101**, 64510 (2007)



# CHAPTER 3

## Length Scales of Photo-generated Charge Carriers in Semiconducting Polymers

---

---

### 3.1 Introduction

Length scales involved in transport of charge carriers has many important implications in optimizing the device performance along with better understanding of material transport parameters. The process of charge carrier generation upon photo-excitation of the polymer semiconductor films is reasonably well documented. The results have been largely interpreted in terms of a primary process such as excitonic mechanisms [1, 2] and subsequent processes involving charge generation and transport [3]. Photocarrier transport studies of the polymer semiconductors are normally carried out using steady state photoconductivity and transient photoconductivity in sandwich or surface cell configuration. The analysis and interpretation of these results is complicated by the simultaneous presence of both electrons and holes in the same region resulting in recombination processes, trap kinetics and interfacial processes. The coexistence of drift and diffusion process, especially in ambipolar systems and the non-validity of Einstein's relation in the large field regime makes the extraction of the diffusivity from mobility measurements difficult from standard experimental techniques [4, 5]. Even though the standard well-developed methods have yielded accurate quantitative estimates of parameters such as mobility and carrier lifetime distribution, the method implemented in this chapter will complement these measurements with an additional insight such as the degree of ambipolarity, and correlation between lateral and longitudinal transport processes. This chapter presents the experimental results for the determination of length scales for both positive and negative photo-induced charge carrier species in two model

polymer systems P3HT and MEHPPV. A necessary theoretical explanation is provided based on classical drift- diffusion transport model in intrinsic semiconductors.

Semiconducting polymers were found to have different mobilities in the plane and perpendicular to substrates. This ratio is of the order of  $10^{-4} - 10^{-5}$ , particularly in the case of P3HT [6]. The studies of electrical conductivity in organic semiconductor crystals with coplanar contacts and sandwiched between two contacts revealed a strong effect of the surface states on charge carrier transport in these materials. These surface states were found to control conductivity in coplanar contacts, while in sandwich device configurations interfacial localized states strongly affect the rate of charge injection across the metal-organic interface [7]. These studies indicate the possibility of different length scales involved for these two types lateral and transverse transport of charge carriers.

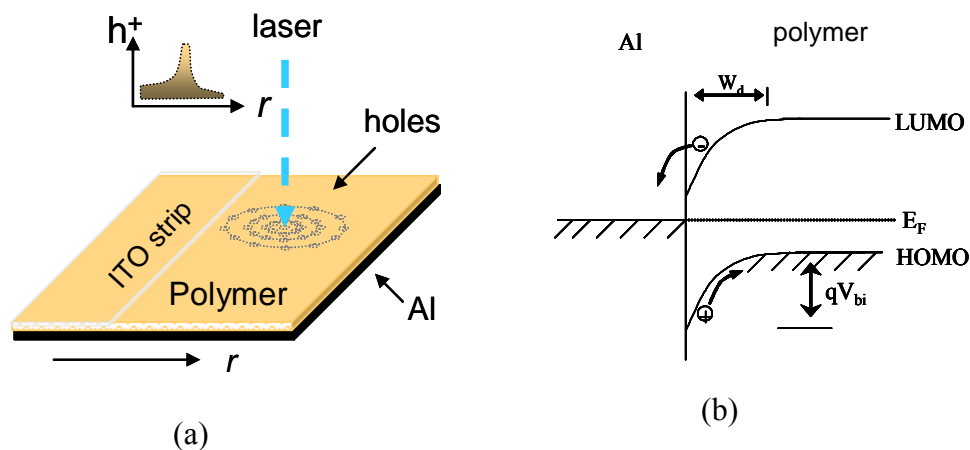


**Figure 3.1** Schematic of spatial photocurrent ( $I_{ph}(r)$ ) decay profile for holes as (a) light beam moves away from overlap region, i.e., edge of ITO strip along Al electrode. (b) Band bending at polymer/Al interface and built-in field separates electron and holes. Electrons are transferred to Al and holes spread in polymer matrix from illumination position.

## 3.2 Strategy

Semiconductor device physics is already well developed in the case of inorganic semiconductors. It has provided a better understanding to explain organic semiconductor device operation [8, 9]. In polymer semiconductors, it has been elucidated that thermally



assisted tunneling (hopping) transport mechanism follow drift-diffusion model, as discussed below:

$$\frac{d}{dr} E = -\frac{q}{\epsilon_r \epsilon_0} n(r) \quad (3.1)$$

$$J = qn\mu E + qD \frac{\partial}{\partial r} n \quad (3.2)$$

$$\frac{\partial}{\partial t} n(r, t) = \frac{1}{q} \frac{\partial}{\partial r} J = \frac{\partial}{\partial r} \left[ D \frac{\partial}{\partial r} n(r, t) + \mu n(r, t) E(r, t) \right] \quad (3.3)$$

where equation (3.1) is the Poisson equation ( $E$  = electric field,  $n$  = charge carrier density,  $\epsilon_r$ = dielectric constant), equation (3.2) is the current equation ( $J$  = current density,  $\mu$  = mobility,  $D$  = diffusion coefficient) and equation (3.3) is the current continuity equation. These equations can model, provided knowledge about the dependence of  $D$  and  $\mu$  on device/ material parameters and specifically on the temperature, electric field, and charge density are known. These equations have been shown to describe OLEDs, solar-cells and 2D (or 3D) version of these for FETs [10].

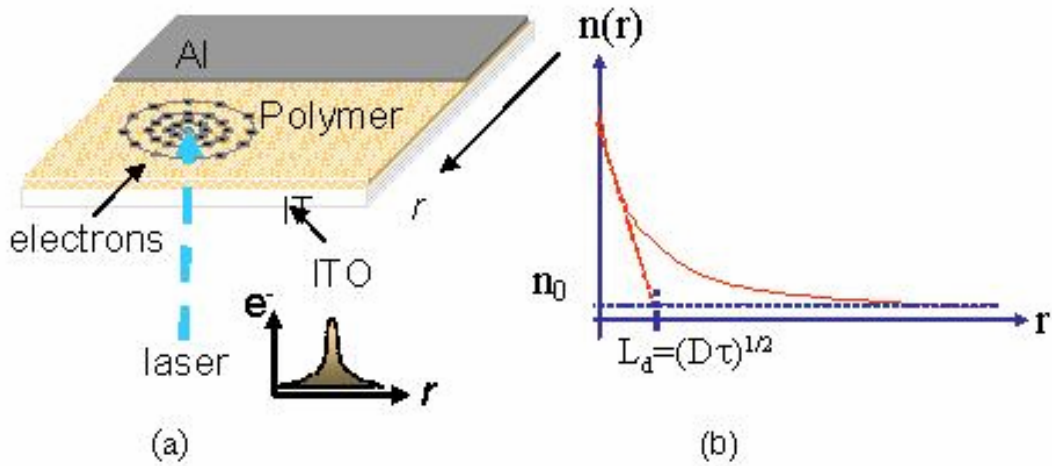


**Figure 3.2** Schematic of spatial photocurrent ( $I_{le}(r)$ ) decay profile for electrons as (a) light beam moves away from overlap region, i.e., edge of Al strip along ITO electrode and (b) typical diffusion assisted carrier density  $n(r)$  decay profile (solid red line).

These set of equations were used to study length scales for electrons and holes in semi-conducting polymers. The transport **Eq. 3.3** can be modified for excess photogenerated charge carriers in the following form

$$\frac{\partial n}{\partial t} - \mu E_x \frac{\partial n}{\partial x} - n\mu \frac{\partial E_x}{\partial x} - D \frac{\partial^2 n}{\partial x^2} = G - \frac{\Delta n}{\tau} \quad (3.4)$$

where,  $G$  -charge generation rate,  $\mu$  - mobility for carriers,  $E_x$  - electric field in  $x$  - direction,  $\Delta n$  ( $= n - n_0$ ) is the excess carriers concentration and  $\tau$  is the relaxation time constant. In steady state and in absence of an external field  $E$  ( $E_x = 0$ ), at low level injection the above expression gives an exponential decaying solution form,

$$n(x) = n_0 \exp(-x/L_d) \quad (3.5)$$

where  $L_d$  is diffusion length.

In case of organic semiconductors, the Einstein relation gets modified because of the amorphous nature. Einstein relation relates two important parameter  $D/\mu$  for any semiconducting materials. In case of crystalline semiconductors it is simply  $V_T$  ( $= k_B T/e$ ). Nevertheless, for conjugated polymers it has one extra term because of a particular shape of DOS, in case of Gaussian DOS the modified form[11] is as follows (discussed in chapter 1 Einstein relation for disordered semiconductors).

$$\frac{D}{\mu} = \frac{kT}{q} \frac{\int_{-\infty}^{\infty} \exp\left[-\left(\frac{E-E_0}{\sqrt{2}\sigma}\right)^2\right] \frac{1}{1 + \exp\left(\frac{E-E_F}{kT}\right)} dE}{\int_{-\infty}^{\infty} \exp\left[-\left(\frac{E-E_0}{\sqrt{2}\sigma}\right)^2\right] \frac{\exp\left(\frac{E-E_F}{kT}\right)}{\left[1 + \exp\left(\frac{E-E_F}{kT}\right)\right]^2} dE} \quad (3.6)$$

For simplicity, a normal form of Einstein relation was used to describe the significance of this relation in extracting the transport length scales for semi-conducting polymers used for studies.

$$D = \frac{k_B T}{e} \mu \quad (3.7)$$

$$\langle r \rangle = \sqrt{(D * t)} \quad (3.8)$$

if 't' becomes carrier recombination lifetime ( $\tau$ ) then distance  $\langle r \rangle$  will become a characteristic length of that specific material, called diffusion length ( $L_d$ ) of charge carrier species. So in the case  $t = \tau$ , combined **Eq. 3.7 & 3.8** gives an expression for  $L_d$  as following

$$L_d^2 = \left( \frac{k_B T}{e} \right) \times \mu \tau \quad (3.9)$$

However, in case of conjugated polymers this analogy may not be directly applicable since the defect concentration and energetics along with the interfacial properties decide the characteristics of the carrier transport. Polymer semiconductors are known to be positional and energetically disordered system, resulting in a broad carrier lifetime distribution. In spite of the absence of a detailed formalism, it is reasonable to relate the decay lengths observed in these *p*-type semiconducting materials to an effective diffusion length, representative of the long-lived carrier tail distribution [see section 1.6]. Nevertheless, **Eq.3 8** also reveals an important fact that experimentally observed  $L_d$  has direct connection with semiconductor quality parameter “mobility-lifetime product ( $\mu\tau$ )”. This parameter determines the degree of ambipolar conduction ( $= (\mu\tau)_h/(\mu\tau)_e$ ) in a polymer semiconductor.

### 3.3 Experimental Studies

Before introducing the central methodology prerequisite experimental results are presented such as I-V characteristics, photocurrent spectroscopy, and substrate characterization.

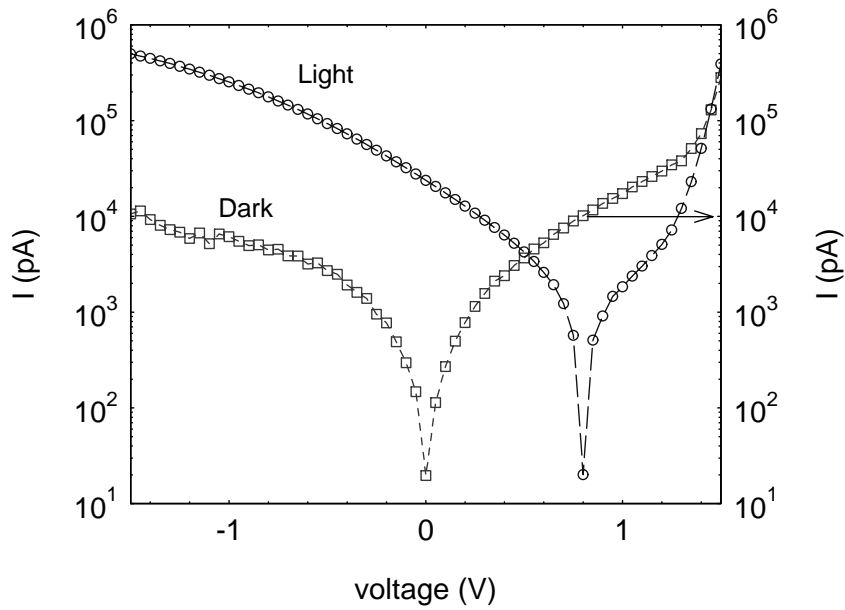


**Figure 3.3** I-V characteristics in dark ( $\square$ ) and broad illumination ( $\circ$ ) conditions for ITO/MEHPPV/Al sandwich device structure. Collimated laser beam ( $\lambda = 532 \text{ nm}$ , optical power  $\approx 2 \text{ mW}$ ) was used to illuminate device from glass side

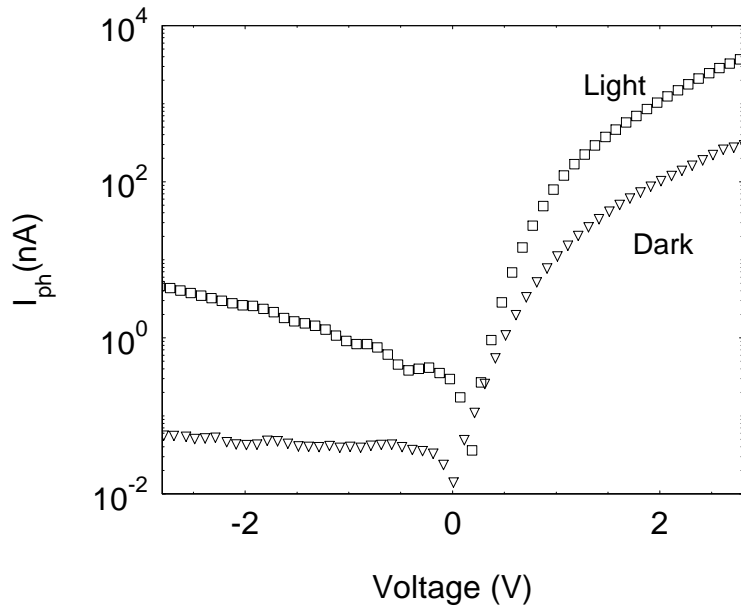


**Figure 3.4** I-V characteristics in dark ( $\nabla$ ) and broad illumination ( $\square$ ) conditions for ITO/P3HT/Al sandwich device structure. Collimated He-Ne laser beam ( $\lambda = 633 \text{ nm}$ , optical power  $\approx 60 \mu\text{W}$ ) was used to illuminate device from glass side

Metal-semiconductor contacts play an important role in device engineering. In these studies, two metal contacts were used, one was Ohmic (ITO-polymer interface) in nature and the top contact was Schottky type (polymer-Al interface). These contact electrode work functions and HOMO – LUMO levels of the polymers manifest whether it will be Ohmic or Schottky interface. I-V characteristic of ITO/ polymer/Al device configuration is shown in **Figure 3.3** and **Figure 3.4** for MEHPPV and P3HT, respectively. The typical experimental setup is shown in **Figure 2.12**. It was found that P3HT and MEHPPV both the polymers form Schottky type interface with Al and Ohmic with ITO as reported in literature [12].

### 3.3.1 Photocurrent Modulation Spectroscopy

Photocurrent spectra for both polymer systems, using an experimental setup (see **Figure 2.11**) as discussed in chapter 2, are shown in **Figure 3.5 (a & b)**. Photocurrent spectra were found to be symbatic (similar to absorption spectra), for the polymer film thickness in the range of  $\sim 100$  nm. Photocurrent spectrum results can be modeled using Beer- Lambert's law ( $I=I_0 \exp(-t/\alpha(\lambda))$ ), where  $I$  = light intensity,  $t$  = thickness of polymer film,  $\alpha(\lambda)$ = absorption coefficient at  $\lambda$ . Polymer film thickness play important role in photocurrent spectrum. At higher  $t$ , it results in antibatic photocurrent spectrum if the device is illuminated from glass side (away from high field region of polymer/ Al Schottky interface) [12]. The band-edge & photocurrent peak for P3HT and MEHPPV were obtained at 650 nm & 540 nm and 600 nm & 500 nm, respectively. Devices were illuminated with a monochromatic collimated rectangular spot (1 mm  $\times$  3 mm). These results were used to select excitation wavelength for photocurrent microscopy.

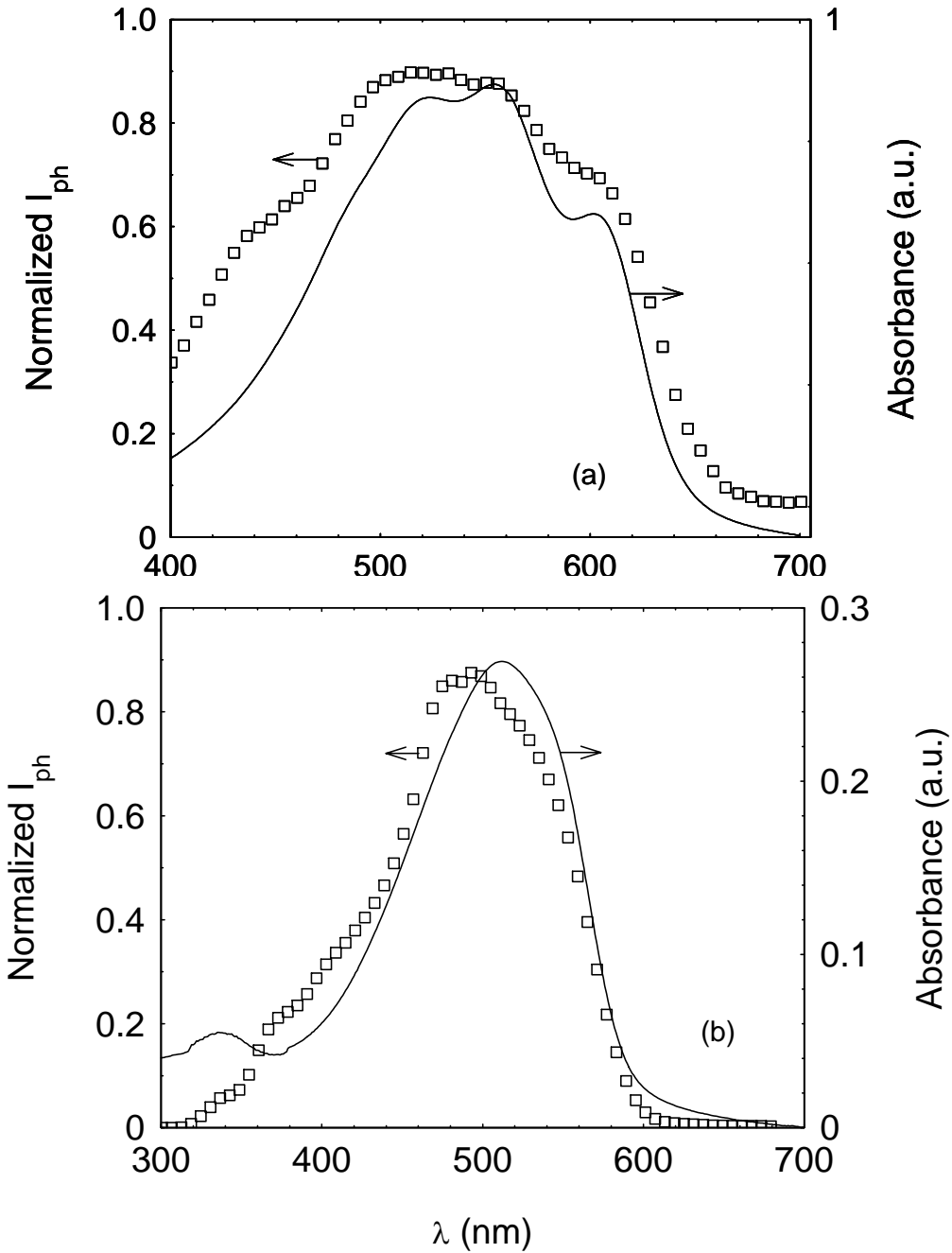


**Figure 3.5** Intensity modulated normalized short circuit photocurrent  $I_{ph}(\lambda)$  spectrum for (a) P3HT and (b) MEHPPV photovoltaics, ITO/Polymer/Al using lock-in technique with broad illumination of collimated monochromatic light from glass side. Solid line is absorbance of polymers.

### 3.3.2 Scanning Electron Microscopy

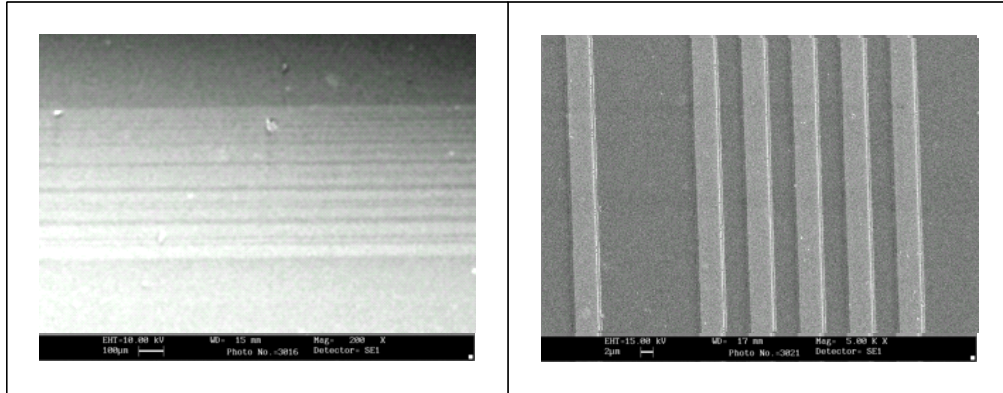


**Figure 3.6** Scanning electron micrographs for electron beam sputtered ITO strips with widths and spacing in the range of 1-50  $\mu\text{m}$ . Darker region of image represent device substrate glass cover-slip and brighter strips are ITO.

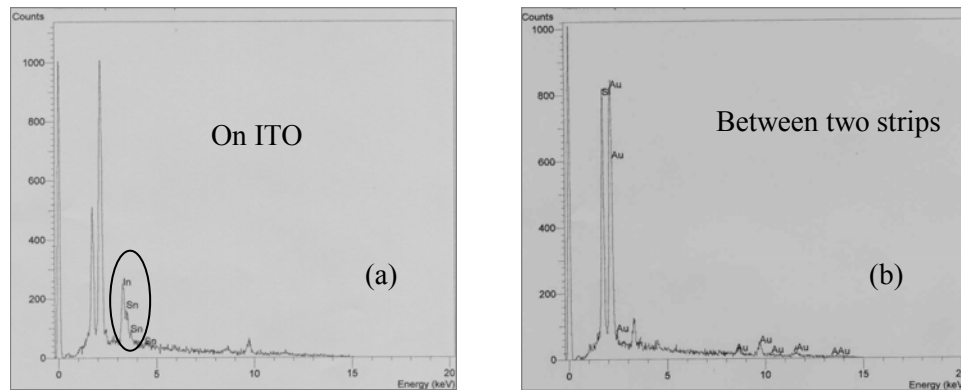


**Figure 3.7** Electron beam diffraction from (a) ITO strip and (b) non -ITO, i.e., gap between two strips.

The electron beam sputtered patterned ITO substrates were scanned by electron beam (see **Figure 3.6**) prior to use for devices. Electron beam diffraction was carried out on ITO strips (**Figure 3.7a**) and in between the strips (**Figure 3.7b**) to ensure that, there is no residue of ITO on non-ITO regions. This was an important verification to make it certain that there are no conductive pathways in between the strips, as those can modify lateral photocurrent scanning results. The ITO strips were spread in the range of 6mm

width with the height of strips being 8 mm. The widths of ITO strips and gap in between were in range of 1  $\mu\text{m}$  to 50  $\mu\text{m}$ .

### 3.3.3 Scanning Photocurrent Contrast Microscopy

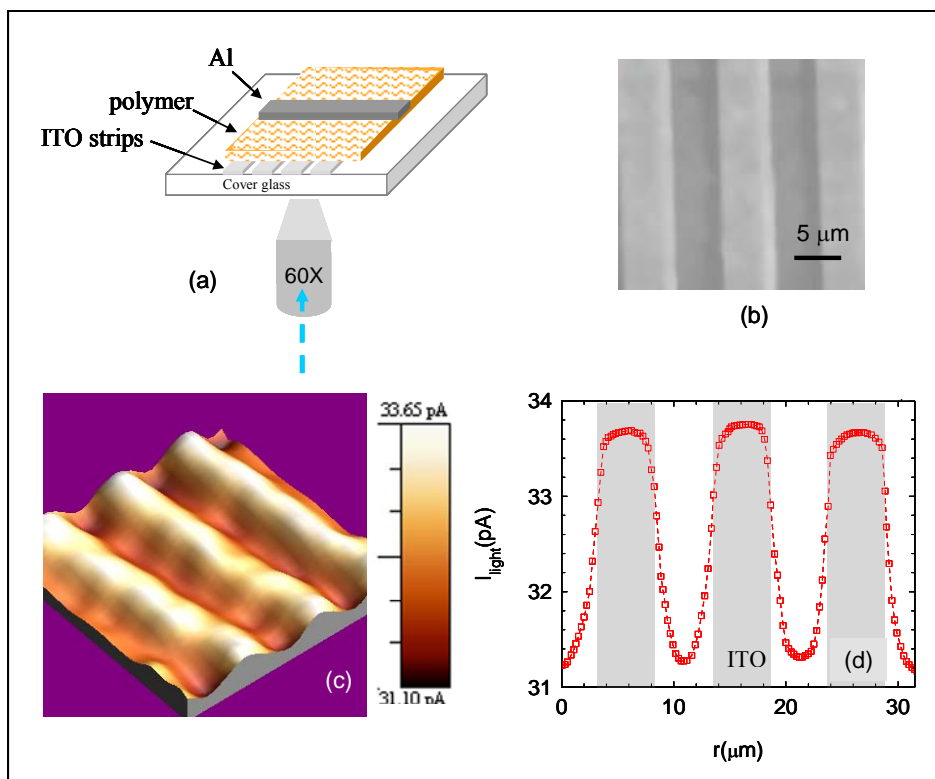


**Figure 3.8** High resolution scanning photocurrent contrast image ( $32 \times 32 \mu\text{m}^2$ ) (a) along patterned ITO strips using laser beam-spot diameter of  $\sim 0.4 \mu\text{m}$ . ( $\lambda = 473 \text{ nm}$ , power  $\sim 100 \text{ nW}$ ) (b) SEM image of an ITO patterned cover-slip substrate revealing sharp boundaries (c) and (d): short-circuit photocurrent 1-D profile from a P3HT film coated on the patterned  $5 \mu\text{m}$  ITO strips, with a top coated orthogonal Al strip, and the focused light incident from the transparent thin cover-slip side using high magnification objective lens (see text) indicating the level of resolution ( $\sim 400 \text{ nm}$ ) in the measurements.

A home-built wide-field photocurrent microscopy setup (see **Figure 2.17**) was used to carry out the lateral photocurrent scans on asymmetric device structures, shown in **Figure 3.8a**. This approach essentially utilizes a photocurrent-contrast imaging of a polymer film sandwiched between patterned substrate and top electrode, where the



incident light beam scans beyond the uniform electric field region of the overlapping electrodes.

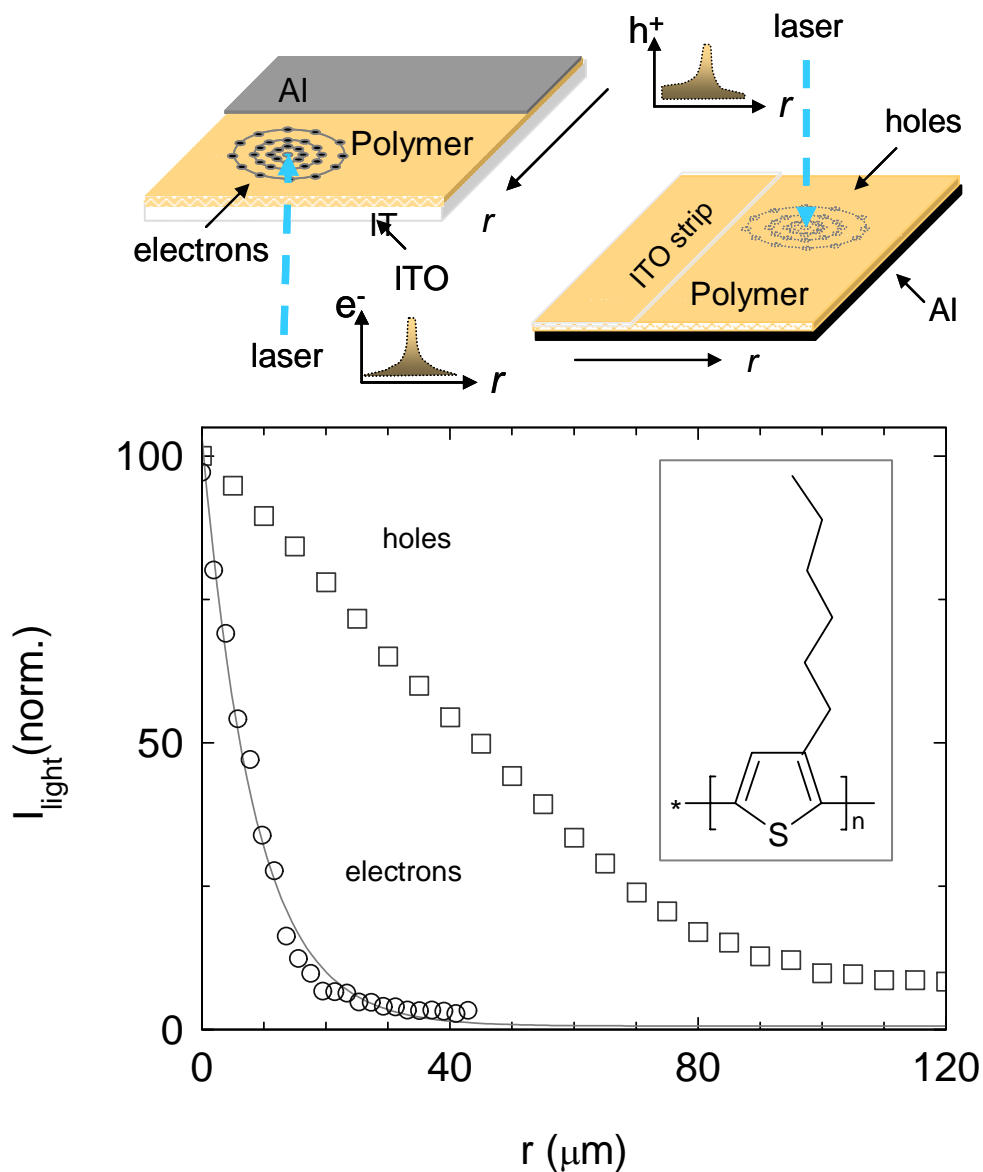


**Figure 3.9** Spatial photocurrents ( $I_{\text{th}}(r_x)$  &  $I_{\text{te}}(r_y)$ ) decay profiles for holes and electrons when light beam scans away from ITO & Al edge on non-overlapping region of electrodes, respectively, for HMDS treated P3HT based device structures using wide field photocurrent microscopy with diode laser (spot of size  $\sim 440$  nm,  $\lambda = 473$  nm, power  $\sim 100$  nW) incident on the centre of the desired electrode strip from glass side. Solid line is exponential fit to  $I_{\text{te}}(r)$ .

The electron/hole transport processes can be independently evaluated by positioning the narrow-light beam selectively over the anode/cathode regions, enabling the estimation of the efficacy of hole transport vis-à-vis electron transport. The key procedure in our studies are the  $I_{\text{light}}(r)$  scans carried out with the beam focused on the overlapping electrode-region of the semiconducting film, the scans are then extended to the non-overlapping regions, as shown in **Figure 3.8c**.

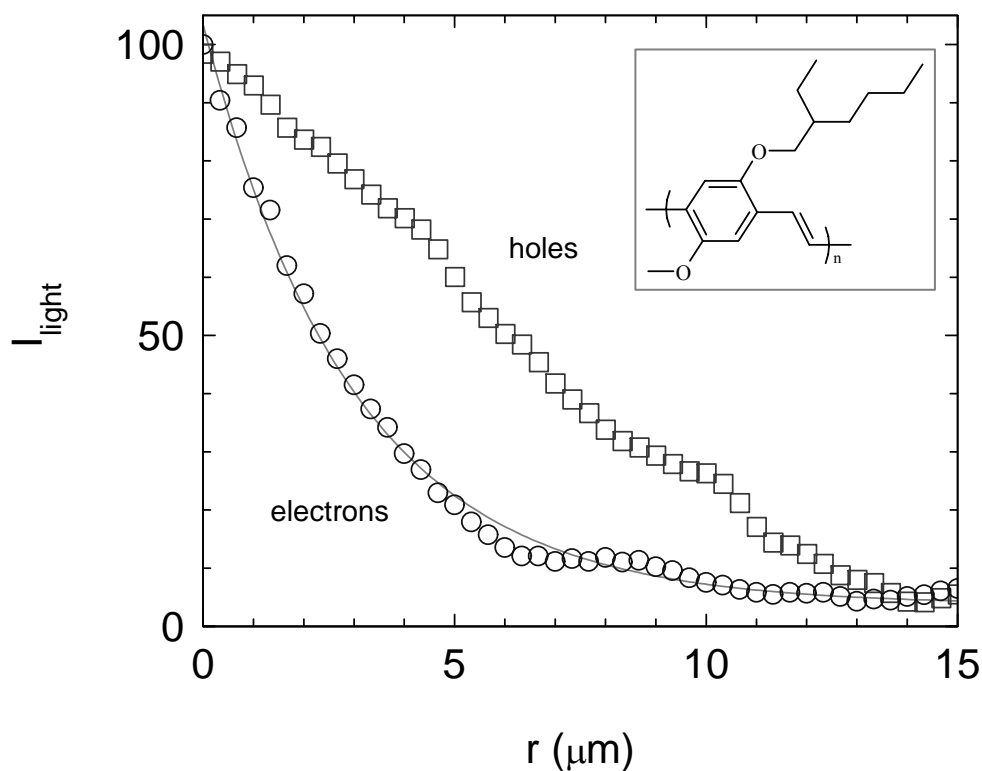


**Figure 3.10** Spatial photocurrents ( $I_h(r_x)$  &  $I_e(r_y)$ ) decay profiles for holes and electrons when light beam scans away from ITO & Al edge on non-overlapping region of electrodes, respectively, for MEHPPV based device structures. using wide field photocurrent microscopy by diode laser- spot of size  $\sim 440$  nm ( $\lambda = 473$  nm, power  $\sim 100$  nW) incident on the centre of the desired electrode strip. Solid line is exponential fit to  $I_e(r)$ .

The 1-D scan in **Figure 3.8c** shows the spatially resolved short-circuit photocurrent profile on the  $5 \mu\text{m}$  wide patterned ITO strip and the light-beam scanned across the orthogonal Al strip. The main feature is the asymmetric response around the sharp ITO-electrode boundary with a nearly constant photocurrent in the overlapping electrode

region and a spatially varying characteristic decay profile outside the ITO coverage. Resolution of these scanning experiments by nature are limited by the beam size and further limited by contributions from scattering and local heating effect. Precautions such as low beam power, high chopper frequency (3 KHz), restrict the measurements to be within the linear range of photocurrent-intensity response (see **Figure 3.13**) and independent wave-guiding experiments and modeling data ensured spatial resolution down to 400 nm. It was found that the response  $I_{ph} \sim (\text{intensity})^\gamma$  was linear at low intensity  $\gamma \sim 1$  and sublinear with  $\gamma = 0.75$  in the higher range as shown in **Figure 3.13**. The short-circuit photocurrent arising from the non-overlapping regions is denoted by  $I_{ie}(r)$ , for contributions arising from the light incident on the ITO region of the polymer films, which is outside the Al electrode boundary signifying largely an electron-current. The short-circuit photocurrent denoted as  $I_{ih}(r)$  signifies hole-current and denotes contributions from regions in front of the Al layer and outside the ITO region (**Figure 3.1** & **Figure 3.2**). The reflected beam intensity is monitored along with  $I_{light}$  in these scans, as shown in **Figure 3.11**. The reflected beam intensity image provides a guideline for coordinates of edge of electrodes while plotting the profiles of photocurrent decay curves. Varieties of device electrodes overlap / non-overlap areas were selected for both kinds of polymers to check the consistency of results. Photocurrent magnitudes were found to be  $\sim 4$  times smaller for MEHPPV than P3HT polymer based devices, as shown in **Figure 3.8** & **Figure 3.12**. The electric field profiles arising at these boundaries can be simulated by solving Poisson's equation using finite-element numerical methods. The estimated decay lengths for the electric field to decay to strength of  $\sim 10 - 100$  V/cm are quite small ( $< 100$  nm) in comparison to the range of scan, as shown in **Figure 3.16**. The general feature in these scans is the presence of  $I_{ie}$  and  $I_{ih}$  beyond the electric field decay lengths, extending over a distance of few microns. In case of  $I_{ih}(r)$ , the hole carrier transport dominates, with the photogenerated electrons getting transferred to the adjacent Al electrode, while in case of  $I_{ie}(r)$  the electron transport dominates the decay kinetics with the holes getting transferred to the ITO electrode.

The magnitude of the current essentially reflects the collection efficiency of these carriers at the counter electrode (non-illuminated) and is a direct measure of the efficiency of charge carrier transport of the system. The photocurrent image analysis was done using WS×M 8.0 software available online [13]. This software also provides option for wavelet analysis for data to enhance the quality of image.

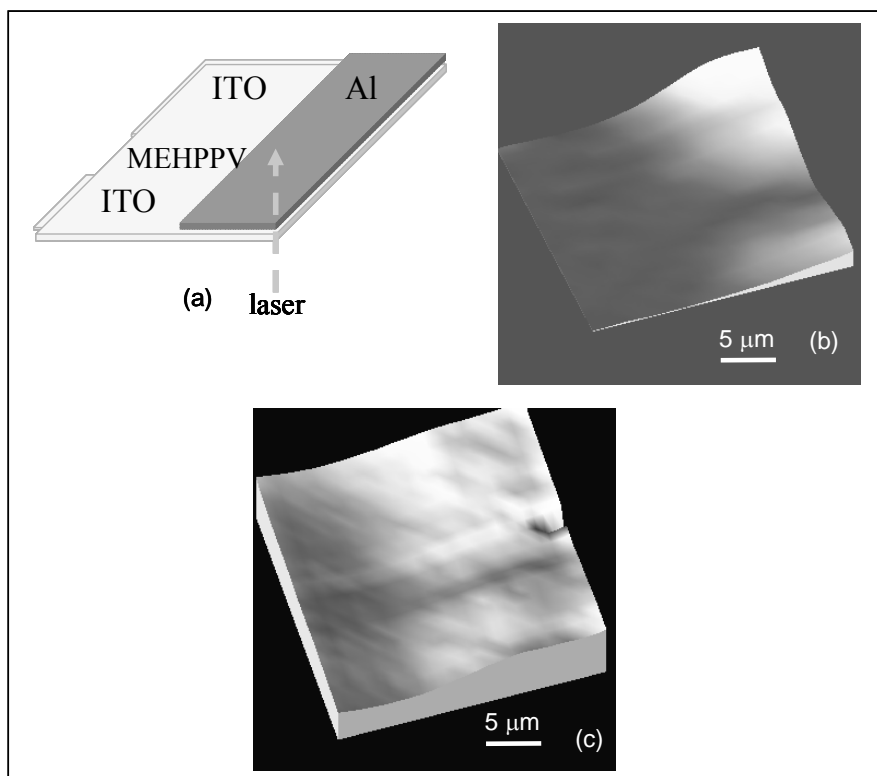


**Figure 3.11** Normalized photoinduced current contrast image (b) for MEHPPV based device structure (a) within the overlapping electrode region and outside the region, simultaneously reflected beam was monitored (c) to set the origin for decay curves of  $I_{le}(r_x)$  and  $I_{lh}(r_y)$ .

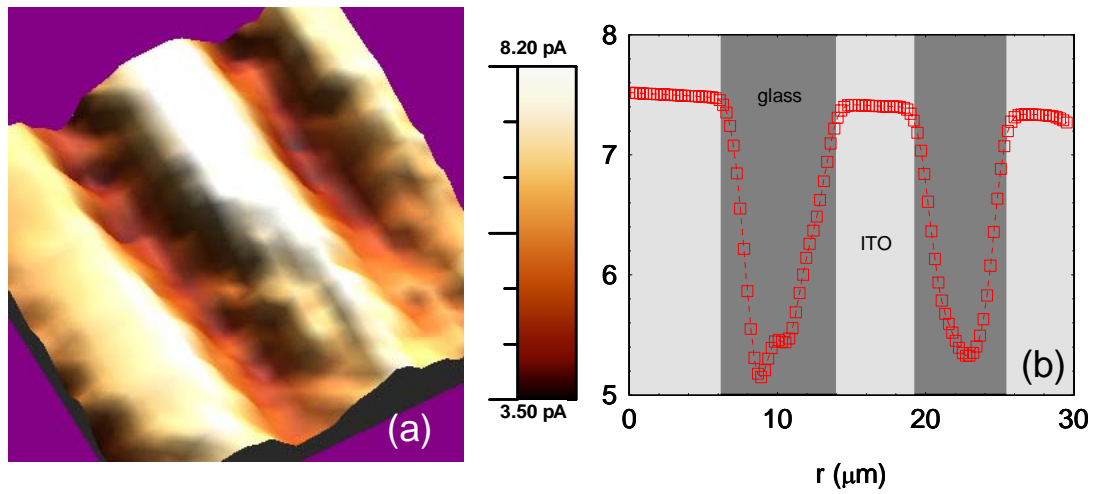


**Figure 3.12** Scanning photocurrent contrast imaging ( $I_{ph}(x,y)$ ) for MEHPPV based device structure on patterned ITO structure ( $30 \mu\text{m} \times 30 \mu\text{m}$ ) within Al electrode. (a) Photocurrent image obtained in short circuit mode using lock-in technique on excitation with diode laser (470 nm) (b) photocurrent,  $I_{ph}$ , profiles obtained from photocurrent image data.

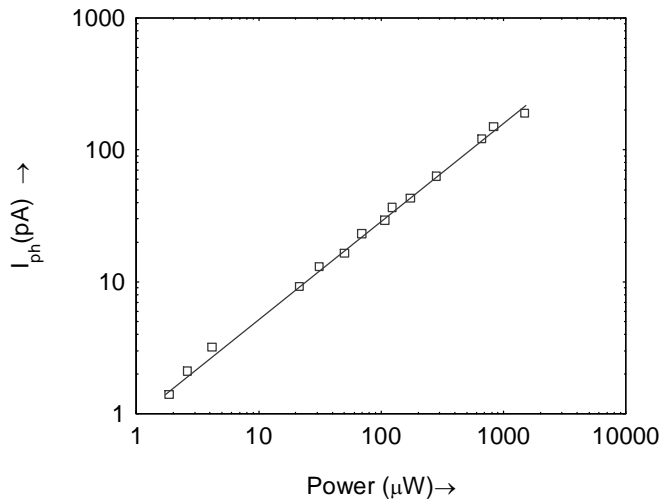


**Figure 3.13** Light intensity versus photocurrent for P3HT based photovoltaic structure using lock-in technique at chopper frequency of 1.2 KHz.

In transient experiment the polarity of the current is checked by an electrometer (at  $t \sim 0$  upon photoexcitation) indicates that there is electron transfer to the Al electrode and hole

transfer to the ITO. The temporal decay profile is governed by the energetics and the kinetics of the bulk carriers. These measurements were done on P3HT based devices with a GaN diode laser ( $\lambda = 405 \text{ nm}$ ) in pulse mode, beam spot was  $\sim 350 \text{ nm}$  with optical power  $40 \text{ nW}$ . First, these measurements were tried with oscilloscope but signal was found very weak due to very small excitation volume and low intensity. However, transient measurements were carried out using a Keithley electrometer, which has its own in-built RC limitation; the minimum integration time for this meter is in the range of  $0.5 \text{ second}$ , which restricts true lifetime measurements. The relaxation time was found to increase with point of illumination away from ITO strip. Transient profiles on sandwich configuration revealed carrier lifetime in range of submillisecond with broad uniform illumination by passive Q-Switch second harmonic Nd:YAG laser.

### 3.4 Simulations

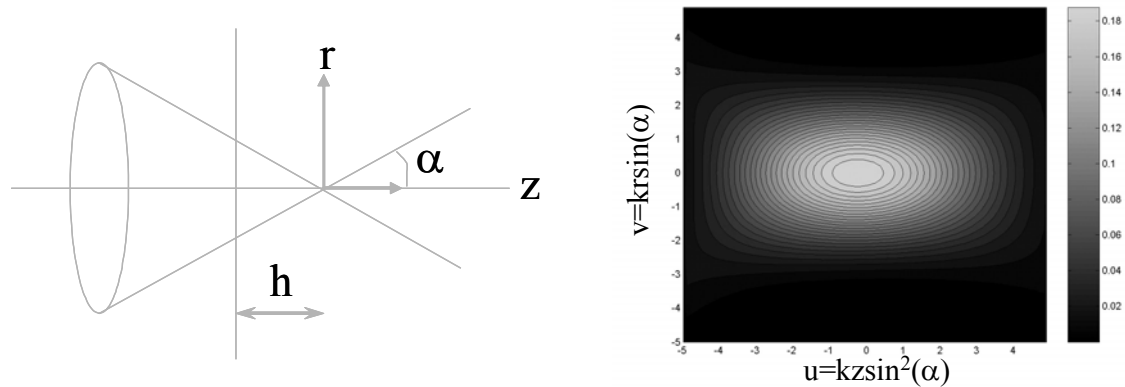


**Figure 3.14** Optical beam simulation inside polymer matrix using Fourier optics formalism. Laser beam coming from  $60\times$  micro-objective lens (with cover-slip correction ring, working distance =  $150 \mu\text{m}$ , numerical aperture ( $= \sin(\alpha)$ ) =  $0.95$ ,  $\lambda = 470 \text{ nm}$ ) focused on patterned ITO substrate.

Light distribution inside the polymer medium was simulated using Fourier optics numerical simulations (see **Figure 3.14**). Due to high absorption coefficients of polymer medium the light gets absorbed at the illumination position without any radial spread, (one single spot). A radial spread of the contour in polymer film was found up to few

microns on neglecting highly absorbed peak region. The light intensity spread contour is plotted ( *Figure 3.14*) with unit-less quantity, as discussed by Wilson et al [14].

$$I(u, v) = A^2 \exp(-2k\alpha_{\text{abs}}(h+z)) \left| \int_0^1 J_0(v\rho) \times \exp(-0.5ju\rho^2) \exp(-0.5\alpha(u+u_0)\rho^2) \rho d\rho \right|^2$$

The estimate of 400 nm is not an observed value but is the calculated value from Fourier optics formulation. Optical scanning was done in diffraction free regime of beam spot, which was ~ 400 nm on sample, but the spot size may vary only due to scattering or fringing at the sharp edges. The spot size, when the micro-objective lens aperture is fulfilled with a collimated light beam, can be given by:

$$spotsize = \frac{0.88 \times \lambda}{N.A.}$$

where

$\lambda$ = wavelength of irradiated light beam

N.A. = numerical aperture of micro – objective lens

While focusing the beam spot near the edge (electrode lines) small scattering was observed, due to edge effect. Due to this fringing, the light spot which is supposed to be of the size of ~ 400 nm, is actually slightly higher in these regions. However, the measured extent of variation in the current around this region of polymer systems is much higher than the spread of beam due to this optical fringing at the edges. Once the beam is away from the edge, a clean diffraction free beam was observed. These optical features were numerically studied to estimate the spread of light beam inside material with input parameters (i) numerical aperture of lens, (ii) wave-vector of irradiated light, (iii) sample thickness, (iv) working distance of micro-objective lens, (v) absorption coefficient of polymer from literature.

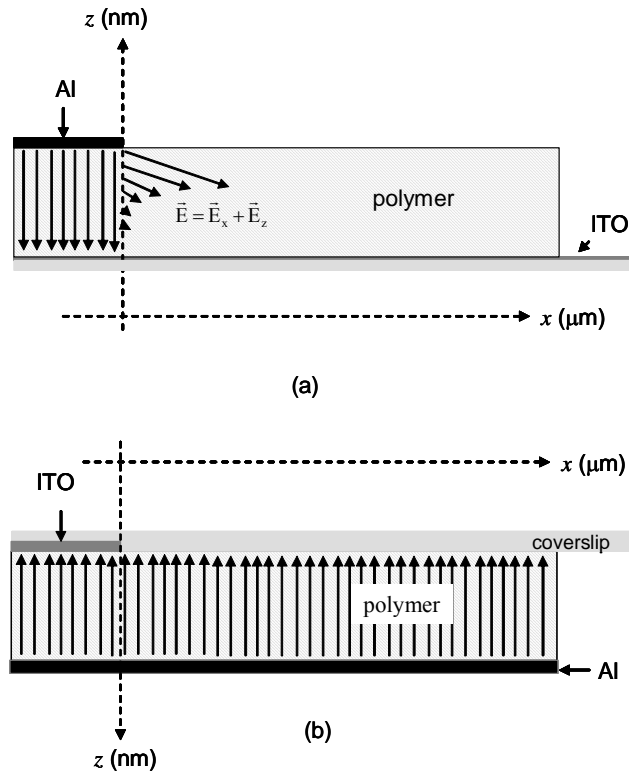


**Figure 3.15** Schematic of electric field distribution inside polymer due to internal field at polymer/Al interface. (a) fringing of electric field is shown at the edge of Al electrode by arrows, arrow head and size represent direction and field magnitude, respectively. (b) in case of longer Al/polymer interface no fringing electric field appears at the edge of ITO electrode.

Matlab partial differential equation (PDE) toolbox was utilized to determine the electric field profiles arising at the electrodes (ITO and Al) boundaries. The electric field profiles were simulated by solving Poisson's equation using finite-element numerical methods. The estimated decay lengths for the electric field to decay to strength of  $\sim 10 - 100$  V/cm are quite small ( $< 50$  nm) in comparison to the range of scan. Matlab simulations were carried out for both cases to simulate electric field distribution inside the polymer, schematic is shown in. The electric field distribution lines are shown in the forms of arrows, direction and amplitudes of field are represented by arrow-head and length of arrow, respectively.

These simulations were carried out to ensure that the decay lengths observed for photo-induced carriers are not result of fringing electric field from the edges of



asymmetric electrode structures. In the calculations, Polymer film thickness was taken as 100nm and dielectric constant was taken as 3.5. When a light beam scans along ITO electrode, there is very high fringing electric field on the edge of Al electrode (see . **a**), but this fringing field also found to decay rapidly. An analytical simulations was carried out to find fringing field distribution outside overlapping region, shown in **Figure 3.17**. An observation was made from these simulation is that electric field is not constant in the transverse direction, i.e., along z-axis. The field responsible for charge carriers to move towards Al electrode is vector addition of  $E_x$  and  $E_z$ . These simulation results assure that photo-generated charge carriers for the illumination position away from Al electrode  $\sim 50$  nm, reaches through diffusion – recombination processes. The field decay profiles ( $E_x$  and  $E_z$ ) with respect to x and z are shown in **Figure 3.17**. In case of the optical beam scans along Al strip away from ITO edge, there was constant electric field through out the polymer/Al interface in dark conditions. When a local light beam spot irradiate this Schottky interface it develops an electric field in the lateral plane [15]. Due to built-in potential charge carriers get separated, electrons transferred to Al electrode and holes remain in polymer, which diffuses towards ITO electrode in the presence of a lateral field. Holes diffusion in such cases was found to have longer decay length scales due to field-assisted diffusion.

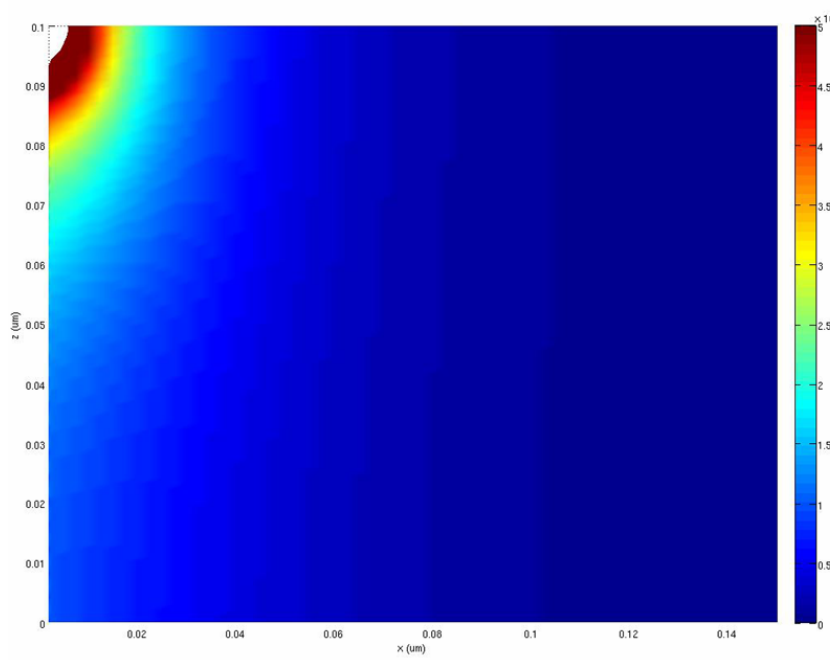


**Figure 3.16** Fringing electric field distribution inside polymer matrix for polymer film thickness of 100 nm.

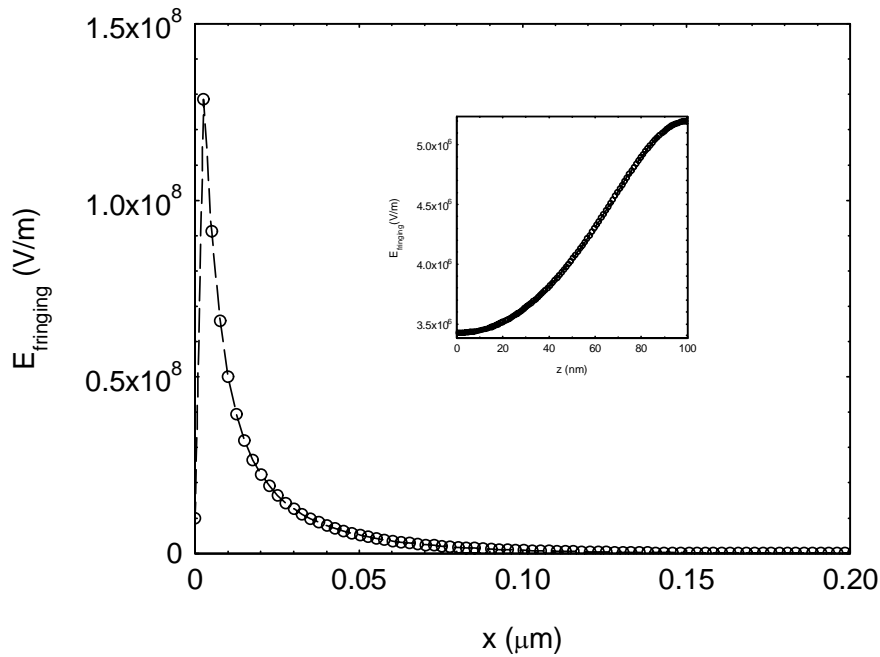


**Figure 3.17** Fringing electric field decay profile along  $x$  (optical beam scanning) direction at  $z=90$  nm, inset shows transverse ( $z$ - direction) fringing field profile at  $x = 50$  nm.

### 3.5 Discussion

There is a subtle difference in the charge carrier generation mechanism and transport leading to  $I_{le}$  and  $I_{lh}$ . In case of  $I_{lh}$ , the photogenerated excitons dissociate in the vicinity of polymer-Al interface under the influence of the built-in Schottky type barrier potential within the depletion zone. Subsequently, electrons are transferred to the equipotential Al electrode, leaving the holes in active polymer network. The separated holes at the interface distort the built-in potential locally, which in the steady state sets up a non-local lateral electric field that further induces a lateral flow of the separated holes. This lateral charge flow, which is ohmic in nature, produces a potential drop between the locus of illumination and the electrode (**Figure 3.1** schematic) [15, 16, 17].

**Table 3.1** Decay lengths for electrons ( $L_{de}$ ) and holes ( $L_{dh}$ ) extracted from exponential fits to  $I(r)$  shown in **Figure 3.9** and **Figure 3.10**. and  $(\mu\tau)_{hole}/(\mu\tau)_{electron}$  ratio estimated from  $(L_{dh}/L_{de})^2$

Polymer	decay length ( $L_{de}$ ) from $I_{le}(r)$	decay length ( $L_{dh}$ ) from $I_{lh}(r)$	$\mu_h\tau_h/\mu_e\tau_e$
P3HT	8.3 $\mu\text{m}$	51.1 $\mu\text{m}$	37.54
MEHPPV	2.8 $\mu\text{m}$	6.8 $\mu\text{m}$	5.96

It can be interpreted as field assisted diffusion in such structures, which have been discussed in transport studies of conjugated polymer based devices. These anomalously higher transport lengths can be explained on the basis of inherently disordered induced broadening of the waiting time distribution. It is accompanied with a field-induced increase of the Einstein  $\mu/D$  ratio whose value in a discrete system is  $e/kT$  [18]. In case of  $I_{le}$ , the absence of a significant presence of a Schottky character results in a poor charge generation along with smaller magnitude of charge (holes) transfer to the ITO electrode which ultimately lead to a limited range of the active region. In general,  $I_{le}$  is primarily a diffusion-recombination process while the hole current  $I_{lh}$  has a sizable drift component or field assisted diffusion for the systems studied here in this chapter. Additional experimental features observed from temperature dependence of the spatial variation, external bias dependence, and results from different electrode combinations are

consistent with this interpretation (see Chapter 5). Hence, even though the  $I_{lh}(r)$  fits to simple exponential decay fits is not entirely appropriate, the analysis brings about the differences in the length scales when comparing with  $I_{le}(r)$  profiles.

A significant presence of  $I_{light}$  was observed in the non-overlapping region for all the three systems studied. The direction of the light induced dc current from these regions indicated a polarity corresponding to an electron transfer to Al and holes transfer to ITO. A general feature for all the systems studied indicated that  $I_{le} < I_{lh}$  and  $L_{de} < L_{dh}$ . These measurements were carried out on five device structures of each system. At least four different regions were studied and scanned along the two directions in each device to minimize features arising from local in-homogeneities. The statistical variations in the devices were not significant. The analysis of the measurements yielded a set of decay lengths, which had a deviation for each system of less than 15 %. The substrate treatment and annealing conditions play a significant role in the chain organization resulting in a 2D lateral network in P3HT films [19, 20]. Measurements were carried out on films processed through a route where reasonable FET characteristics have been earlier observed in our laboratory [20, 21]. *Figure 3.9* indicates the spatial profile of  $I_{lh}$  for an ordered P3HT film from which one can extract the decay parameters (**Table 3.1**). The large decay length of both  $L_{de}$  &  $L_{dh}$  (*Figure 3.9* and **Table 3.1**) can be directly attributed to the same set of factors, which promote the FET mobility that arise from the formation of ordered regions on HMDS-treated glass substrate. Another direct experimental evidence for the large decay length scales is also observed when the inter-electrode (ITO strip-spacing) gets closer, the  $I_{lh}(r)$  gets modified due to the presence of the adjacent electrode strip held at the same potential. The large decay lengths in the range of 50  $\mu\text{m}$  can also be inferred from a set of complementary experiments. Measurements on patterned ITO electrodes spaced apart by 5  $\mu\text{m}$  (**Figure 3.8c**) indicate that the spatial dependence  $I_{lh}(r)$  is altered with an appearance of a plateau region corresponding to the central region between the ITO strips, instead of an uninterrupted-complete decay shown in *Figure 3.9*. The ITO electrode spacing can be then also used as a parameter to verify the length scale of the decay characteristics. It was also found that the estimate of  $L_d$  was

reproducible by scanning over different segments of the films. The measurements of the decay lengths on a set of devices fabricated under different processing conditions (ex.: thermal treatment conditions) also follow the trend of improved structural order through different processing parameters. Therefore, these results demonstrate a correlation between the molecular 2-D nanostructure and the optoelectronic process length scales [22].

In a simplistic sense, if the decay lengths from these experiments are construed as conventional diffusion lengths derived from Einstein's relations  $L_n^2 = (k_B T/e)\mu_n \tau_n$ , then one can take these  $L_d$  values as a measure of  $\mu\tau$  product [23]. Realistic situation prevailing in these systems are complex since the Einstein relations are known to be violated, apart from the observed field assisted diffusion process [24] and the field dependent mobility [25] behavior in these systems. Nevertheless, a correspondence between the observed decay lengths and the  $\mu\tau$  products was observed in these polymer systems. Assumption of Einstein's equation leads to a mobility-lifetime product ratio  $\mu_h\tau_h/\mu_e\tau_e$ , is  $\sim 40$ , and is comparable to the observed field effect mobility ratio of  $\mu_h/\mu_e \sim 10$  observed in P3HT transistors recently [26]. The additional factors of the carrier lifetime ratios and corrections originating from the anisotropic diffusion constants (lateral and longitudinal) can lead to a closer comparison [24]. The values of reported  $\mu\tau$  for P3HT arrived from bulk measurements in the sandwich geometry are significantly different from the present measurements [27]. This deviation can be explained on the basis of interpreting the observed  $L_d$  in our case as contributions arising largely from the slowest recombination processes under steady state condition (deeper traps level) and the lateral character of the diffusion as opposed to the bulk-transverse diffusion [24]. The results from this approach where  $r_{x,y} \gg$  thickness of the polymer film, is largely a characterization of dominant lateral charge transport processes.

MEHPPV is a representative for disordered system from both the bulk and lateral transport perspective. Conformational flexibility of the chains leading to random coiled structure provides the bulk disorder and the phenyl rings which are expected to be parallel to surface of substrates [28] with decreased overlap of  $\pi$ -  $\pi^*$  wave-functions

contribute to the lower lateral transport features. The results reveal lower values for  $L_{de}$  and  $L_{dh}$  compared to region-regular P3HT films (**Figure 3.10 & Table 3.1**), indicating an inefficient 2D lateral transport characteristics.  $\mu_h\tau_h$  of  $\approx 1.9 \times 10^{-7} \text{ V}^{-1}\text{cm}^2$  from these measurements is consistent within the range of reported values for  $\mu_h\tau_h$  for MEHPPV [29], implying an equivalence of lateral transport and bulk transport  $\mu\tau$ . The ratio of mobility life time product,  $\mu_h\tau_h/\mu_e\tau_e$  is  $\approx 6$ , and is consistent with the reported values arrived from space charge limited current measurements of MEHPPV films [30].

### 3.6 Conclusions

In summary, a new scanning-probe method has been introduced using asymmetric device structures to study photocarrier generation and transport in two distinct model systems represented by 2-D ordered P3HT and disordered MEHPPV [31]. The method provides a measure of the relative degree of order for charge transport, introduced by varying film processing conditions and yields length scales for  $p$ -type and  $n$ -type transport in these systems. The generality of the approach to simultaneously probe both  $p$ -type and  $n$ -type can provide valuable insight in the design of high-efficient solar cells and ambipolar devices.

## References

---

- [1] R. Kersting, U. Lemmer, R. F. Mahrt, K. Leo, H. Kurz, H. Bassler, E. O. Gobel, *Phys. Rev. Lett.* **70**, 3820 (1993)
- [2] U. Rauscher, H. Bassler, D. D. C. Bradley, M. Hennecke, *Phys. Rev. B* **42**, 9830 (1990)
- [3] G. Lanzani *Photophysics of Molecular Materials From Single Molecule to Single Crystal* (Wiley VCH, Weinheim, **2006**)
- [4] R. Richert, L. Pautmeier, H. Bässler, *Phys. Rev. Lett.* **63**, 547 (1989)
- [5] A. Hirao, H. Nishizawa, M. Sugiuchi, *Phys. Rev. Lett.* **75**, 1787 (1995)
- [6] C. Tanase, E. J. Meijer, P.W.M. Blom, D. M. de Leeuw, *Phys. Rev. Lett.* **91**, 216601 (2003)
- [7] J. Reynaert, K. Poot, V. Arkhipov, G. Borghs, P. Heremans, *J. Appl. Phys.* **97**, 063711 (2005)
- [8] (i) N. Tessler, Y. Roichman, *Appl. Phys. Lett.* **79**, 2987 (2001)  
(ii) Y. Roichman, N. Tessler, *Appl. Phys. Lett.* **80**, 2987 (2002)  
(iii) N. Rappaport, Y. Bar, O. Solomeshch, N. Tessler, *Appl. Phys. Lett.* **89**, 252117 (2006)
- [9] D. Basu, L. Wang, L. Dunn, B. Yoo, S. Nadkarni, A. Dodabalapur, M. Heeny, I. McCulloch, *Appl. Phys. Lett.* **89**, 24210 (2007)
- [10] (i) A. A. Muhammad, A. Dodabalapur, M. R. Pinto, *IEEE Trans. Elec. Dev.* **44**, 1332 (1997)  
(ii) T. Li, J. W. Balk, P. P. Ruden, I. H. Campbell, D. L. Smith, *J. Appl. Phys.* **91**, 4312 (2002)  
(iii) P. V. Necliudov, M. S. Shur, D. J. Gundlach, T. N. Jackson, *J. Appl. Phys.* **88**, 6594 (2000)
- [11] Y. Roichman, N. Tessler, *Appl. Phys. Lett.* **80**, 1948 (2002)
- [12] (i) S. Nagamatsu, S. S. Pandey, W. Takashima, T. Endo, M. Rikukawa, K. Kaneto, *Synth. Met.* **121**, 1563 (2001)  
(ii) W. Bantikassegn, O. Inganas, *Synth. Met.* **87**, 5 (1997)

- 
- (iii) M. G. Harrison, J. Gruner, G. C. W. Spencer, *Phys. Rev. B* **55**, 7831 (1997)
- [13] Link for WSxM scanning probe microscopy software: <http://www.nanotec.es>
- [14] Wilson, *J. Appl. Phys.* **61**, 191 (1987)
- [15] D. Kabra, Th. B. Singh, K. S. Narayan, *Appl. Phys. Lett.* **85**, 5073 (2004)
- [16] J. Henry, J. Livingstone, *Adv. Mat.* **13**, 1023 (2001)
- [17] G. Lucovsky, *J. Appl. Phys.* **31**, 1088 (1960)
- [18] A. Hirao, H. Nishizawa, M. Sugiuchi, *Phys. Rev. Lett.* **75**, 1787 (1995)
- [19] H. Siringhaus, P. J. Brown, R. H. Friend, M. M. Nielsen, K. Bechgaard, B. M. W. L-Voss, A. J. H. Spiering, R. A. J. Janssen, E. W. Meijer, P. Herwig, D. M. de Leeuw, *Nature* **401**, 685 (1999)
- [20] S. Dutta, K. S. Narayan, *Adv. Mat.* **16**, 2151 (2004)
- [21] S. Dutta, K. S. Narayan, *Phys. Rev. B* **68**, 125208 (2003)
- [22] (i) R. J. Kline, M. D. McGehee, M. F. Toney, *Nat. Mat.* **5**, 222 (2006)
- (ii) Y. Kim, S. Cook, S. M. Tuladhar, S. A. Choulis, J. Nelson, J. R. Durrant, D. D. C. Bradley, M. Giles, I. McCulloch, C-S Ha, M. Ree, *Nat. Mat.* **5**, 197 (2006)
- (iii) C.Y. Yang, C. Soci, D. Moses and A. J. Heeger, *Synth. Met.* **155**, 639 (2005).
- [23] Y. Gu, J. P. Romankiewicz, J. K. David, J. L. Lensch and L. J. Lauhon, *Nano Lett.* **6**, 948 (2006)
- [24] S. V. Novikov, G. G. Malliaras, *Phys. Stat. Sol. (b)* **243**, 391 (2006)
- [25] D. Hertel, H. Bassler, U. Schref, H. H. Horhold, *J. Chem. Phys.* **110**, 9214 (1999)
- [26] L.-L. Chua, J. Zaumseil, J.-F. Chang, E. C.-W. Ou, P. K.-H. Ho, H. Siringhaus, R. H. Friend, *Nature* **434**, 194 (2005)
- [27] G. Juska, K. Genevicius, R. O. Sterbacka, K. Arlauskas, T. Kreouzis, D.D.C. Bradley, H. Stubb, *Phys. Rev. B* **67**, 081201 (2003)
- [28] L. Kunardi, C. Troadec, N. Chandrasekhar *J. Chem. Phys.* **122**, 204702 (2005)
- [29] V. Duzhko, Th. Dittrich, B. Kamenev, V. Yu Timoshenko, W. Brutting, *J. Appl. Phys.* **89**, 4410 (2001)
- [30] L. Bozano, S. Carter, G. Malliaras, P. Brock, *Appl. Phys. Lett.* **74**, 1132 (1999)
- [31] D. kabra, K. S. Narayan, *Adv. Mat.* 2007 (DOI: 10.1002/adma.200602405)



# CHAPTER 4

## Enhancement in Electrical Transport and Ambipolar Conduction

### 4.1 Introduction

Conjugated polymer chains form typically disordered network in solid state, which leads to meager electrical characteristics. A strong correlation between ordered structure and electrical properties has been established. Recent report on an ordered polymer has shown the field effect mobility as high as  $\sim 0.6 \text{ cm}^2\text{V}^{-1}\text{S}^{-1}$  [1]. These ordered polymer chains can be achieved by (i) stretching the polymer film [2] (ii) using a physical template (iii) chemical treatment of dielectric with self-assembled monolayer (SAM) [3,4]. There are reports of enhanced charge carriers mobility in poly(3-hexylthiophene) (P3HT), ladder-poly(paraphenylene) (LPPP), stretched PPV, poly(diacetylene), poly(dioctylfluorene) (PFO) by alignment of the polymer chains. There are different ways to align polymer chains in 2D- plane or linearly (1D), which depends upon molecular structure of the polymer. In particular, for 1D orientation liquid crystalline polymers offer higher degree of ordered mesophase domain structure [1].

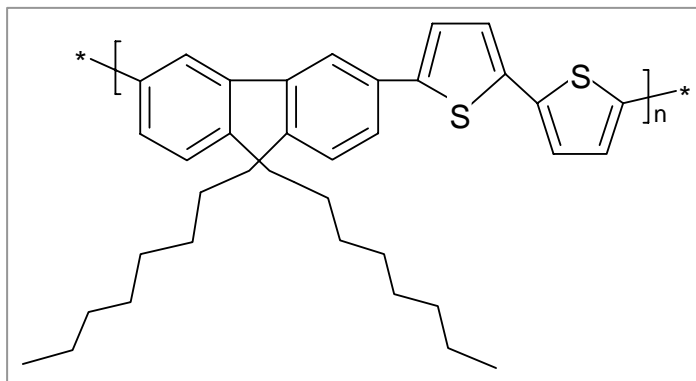


**Figure 4.1** Chemical structure for poly (dioctylfluorene-co-bithiophene) (PFO-TT or PF8T2)

Recently, alkyl substituted polydioctylfluorene (PFO) polymers have shown many attractive material features such as (i) laser emission [5, 6] (ii) polarized light emission [7] (iii) structural conformation [8, 9] (iv) structurally induced electrical transport [10, 11, 12] (v) relative air stability [13]. PFO has been found to have unique features of solid state ordering and morphology, the structures of alkyl side chains at position-9 of fluorenes moieties (see *Figure 4.1*) strongly influences the solid state packing of polymer chains upon temperature treatment [14], upon exposing the film to solvent vapors [15], or treating the polymer with solvent/non-solvent mixture with increasing quantity of non-solvent [16, 17]. Here, this chapter will focus on copolymers of fluorene. Polyfluorenes display a 'blue' bandgap that is almost indifferent to the type of side-chain attached. Note that side-chains are attached pair wise at a position which itself is not part of the conjugated backbone, and these pairs are widely spaced, so that there is neither steric nor electronic impact of the side-chains on the backbone properties. However, strictly alternating copolymers of fluorenes with co-monomers with different electronic properties have been prepared, such as F8BT (alternating copolymer between dioctyl fluorene with benzothiadiazole) and F8T2 (alternating copolymer of dioctyl fluorene with two thiophenes). For both F8BT and F8T2, the resulting bandgap is reduced, and they both emit in the green- yellow region. The reduction of the bandgap has different reasons: In the case of F8BT, the benzothiadiazole co-monomer has a higher electron affinity (EA) than fluorene, thus resulting a polymer with higher EA. In the case of F8T2, the two thiophene groups have a lower ionization potential (IP) than fluorene, thus resulting a polymer with lower IP. Copolymerization thus does not only allow control of the bandgap, but of both IP and EA in a predictable manner, and a large number of fluorene copolymers have been synthesized and studied [18]. Both the polymers have found interesting applications: Some of the most efficient organic EL devices have been built from blends of a minority amount of F8BT as electron injecting / transporting material in hole injecting / transporting polyfluorene host material. F8T2, on the other hand, is an excellent material for *p*-type OFETs where an enhanced mobility have been observed along the align direction of polymer chains. Photocurrent studies on these aligned

structures have not been studied upto the level of dark electrical conduction in oriented and unoriented polymer films. However, microwave photoconductivity measurements were carried out and charge transport in the direction of alignment of the polymer chains was found to be 7 times higher than in perpendicular direction [19]. This chapter comprise of studies of photogenerated charge carrier transport on oriented and unoriented polymer films. The results obtained from these studies reveal the connection between electrical & optical anisotropy along with the degree of ambipolar conduction parallel & perpendicular to oriented chains direction. Spatial anisotropic property has been utilized to fabricate high mobility polymer FETs. Higher degree of optical anisotropy elucidates the potential use of PFO-TT film based devices as an optical polarization sensor.

## 4.2 Optical and Electrical Anisotropy

The results obtained on liquid crystalline polymer shown a direct evidence of birefringence in solid film, which influence electrical transport. The order of orientation ( $s$ ) in polymer film was calculated from dichroic ratio ( $D_{\text{abs}}$ ) obtained by polarized absorption spectra. The order of orientation can be calculated from the following formula:

$$s = (D_{\text{abs}} - 1)/(D_{\text{abs}} + 2) \quad (4.1)$$

where

$$D_{\text{abs}} = \text{Abs}_{\parallel} / \text{Abs}_{\perp} \quad (4.2)$$

$\text{Abs}_{\parallel}$  and  $\text{Abs}_{\perp}$  are the absorbance of aligned polymer chains for incident light parallel and perpendicular polarized with respect to rubbed PI channels direction, respectively. Photoluminescence has a direct connection with molecular ordering, i.e., an effective dipole moment of a molecule. Polarized PL spectra have been used to determine order of orientation in case of aligned polymer chains. Photocurrent spectra also provide an insight of microscopic picture of a specimen. Hence, polarized photocurrent spectra manifest a macroscopic ordering of polymer chains from their microscopic conformational packing.

Charge transport along the conjugated segments of the polymer backbone is faster than interchain hopping between adjacent chains. However, the typical persistence length  $L_p$  of polymer chains, that is, the characteristic length of a straight chain segment, is much smaller than the length scales observed. For structurally similar F8T2 a value of  $L_p \approx 8.5$  nm [20] has been determined. Therefore, even in devices in which the polymer chains are aligned parallel to the transport direction, the rate-limiting step is the interchain hopping process between adjacent chains. The observation of similar activation energies for parallel and perpendicular TFT channels suggest that at the low in-plane electric field strengths of long-channel TFTs ( $E = V_{sd} / L = 10^3 - 10^4$  V/cm), the interchain hopping rate  $\nu$  is independent of the direction of electric field with respect to direction of the chain alignment ( $\nu_{\parallel} = \nu_{\perp}$ ) [21]. This implies that the anisotropy may be interpreted in terms of the differences in average distance that charge carriers diffuse per interchain hopping step. Using the Einstein relationship between mobility and diffusion coefficient  $D$  the mobility is proportional to the average square distance  $\langle r^2 \rangle$  traveled per time interval in the direction of the applied field.

$$\frac{(\mu)_{\parallel}}{(\mu)_{\perp}} = \frac{D_{\parallel}}{D_{\perp}} = \frac{L_{d,\parallel}}{L_{d,\perp}} \quad (4.3)$$

### 4.2.1 Polarized Absorption Spectroscopy

The intrinsic bulk optical properties such as absorption and fluorescence are highly anisotropic since the macroscopic tensor is determined by the single molecule tensor and the orientational transformation matrix that relates the molecular and macroscopic axes. Their elements are linked with orientational order parameters characterizing the orientation distribution function in the PFO-TT chains. Optical transmission and polarized EL measurements [22] of these polymer devices indicate the anisotropic properties. Oriented polymer films were excited with polarized monochromatic light for absorption spectrum measurements. Absorption spectrum were taken for two polarization axis of light, parallel and perpendicular to rubbed direction of

polyimide layer. Absorption of light excitation parallel to chain was found to be 3.5 times higher than the perpendicular excitation, as shown in *Figure 4.2*. These spectrums provide a vital aspect about the macroscopic order of orientation of PFO-TT polymer chains.

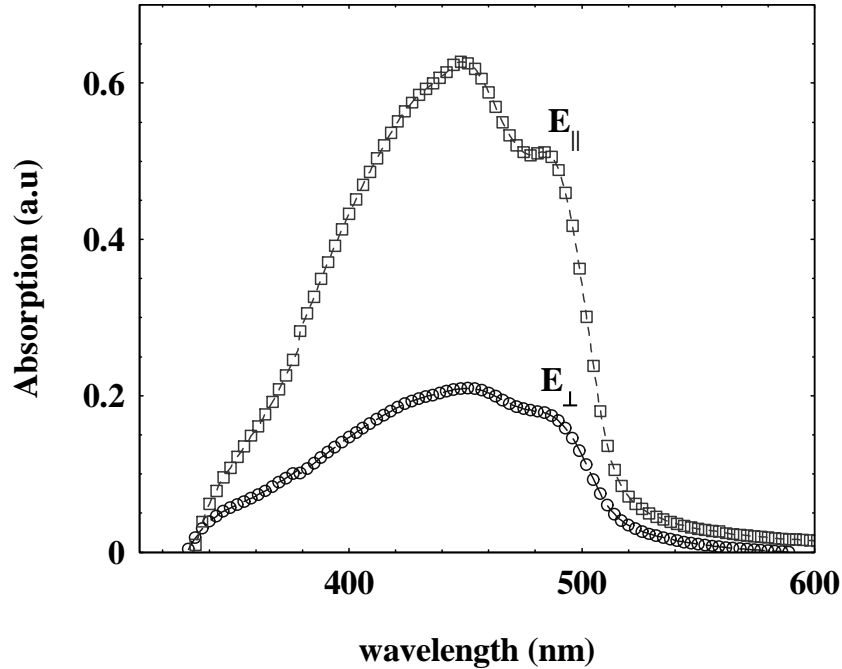


*Figure 4.2* Absorption spectrum of oriented PFO-TT chains on rubbed PI alignment layer for excitation optical beam polarization parallel ( $\square$ ) and perpendicular ( $\circ$ ) to alignment direction.

#### 4.2.2 Polarized Photocurrent Spectroscopy

The anisotropic feature also appears in the photocurrent measurements.  $I_{\text{light}}$  is a bulk process with the total efficiency governed by the carrier generation process and the subsequent transport of the charge carriers. The polarization dependence of  $I_{\text{light}}$  is essentially an indicator of the charge carrier generation processes with the latter processes of transport independent of polarization of the incident light.  $I_{\text{light}}$  with light incident on a typical solar cell type sandwich structure (in the overlapping, uniform electric field region) reveals a charge collection efficiency ratio  $I_{\text{light}\parallel}/I_{\text{light}\perp} \approx 3.5$  at  $\lambda = 470$  nm, as shown in *Figure 4.3*.

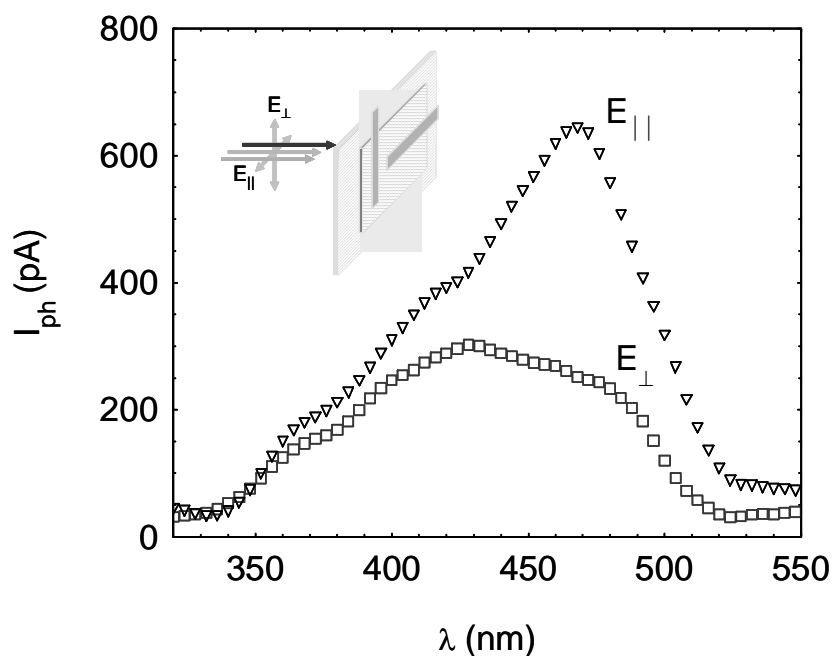


**Figure 4.3** Intensity modulated polarized photocurrent spectroscopy for collimated monochromatic optical beam excitation parallel ( $\nabla$ ) and perpendicular ( $\square$ ) to oriented polymer chains direction.

### 4.2.3 Field Emission Scanning Electron Microscope

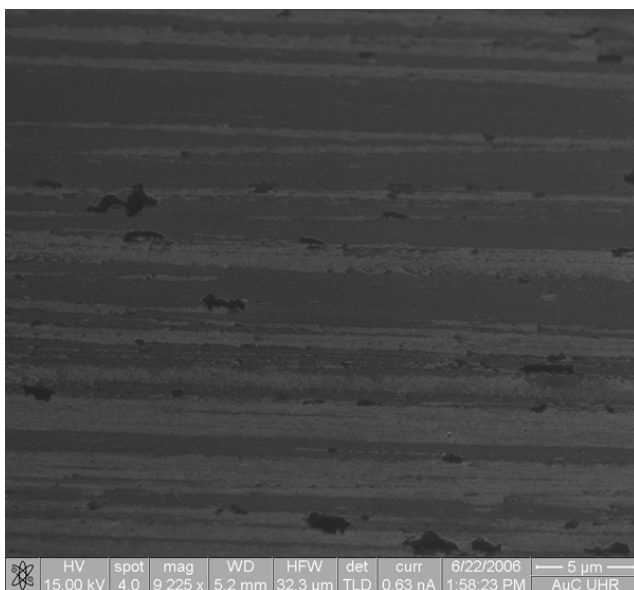


**Figure 4.4** Field emission SEM image of rubbed polyimide layer on glass substrate with patterned ITO on top of polyimide layer.

Substrates were characterized using scanning electron microscopy. A patterned ITO was coated on rubbed polyimide layers and rubbed channels were observable in field

emission scanning electron micrograph, as shown in *Figure 4.4*. The polyimide was spin coated on glass substrates and annealed at temperature 280 °C for 10 minutes. These PI layers were rubbed with soft cloths to make aligned channels for polymer chains. These channels were found to be in the range of submicrometer to 2-3  $\mu\text{m}$  in width. Substrates were cleaned using methanol in ultra-sonicator for 10 minutes prior to PF8T2 coating.

### 4.3 Scanning Photocurrent Contrast Microscopy

Photocurrent decay profiles were carried out on un-oriented and oriented polymer films using scanning photocurrent contrast microscopy setup (see *Figure 2.17*) with high spatial resolution (spot diameter  $\approx 400$  nm, optical power  $\approx 100$  nW, excitation wavelength = 473 nm, chopper frequency  $\approx 1$  kHz). Un-oriented polymer chains were found to show photocurrent decay rapidly with distance between edge of electrode and illumination position. Decay lengths for holes photocurrent ( $I_{\text{h}}$ ) and electrons photocurrent ( $I_{\text{e}}$ ) were obtained using exponential fit to experimental data as  $L_{\text{dh}} \approx 14.1$   $\mu\text{m}$  and  $L_{\text{de}} \approx 3.9$   $\mu\text{m}$ , respectively (see *Figure 4.5*). Similar to P3HT and MEHPPV, interaction between the Al atoms and polymer backbone likely leads to the formation of Al-carbon complexes at the interface, disrupting the  $\pi$ -conjugation along the backbone [23, 24]. This disrupted region provides high-field region which help in exciton dissociation and charge carriers separation.

In the case of oriented samples, decay lengths were found to be higher ( $> 70$   $\mu\text{m}$ , i.e., maximum scan range of Nanonics scanner head). Oriented samples were investigated using a larger span of optical profiling setup (see *Figure 4.6*).

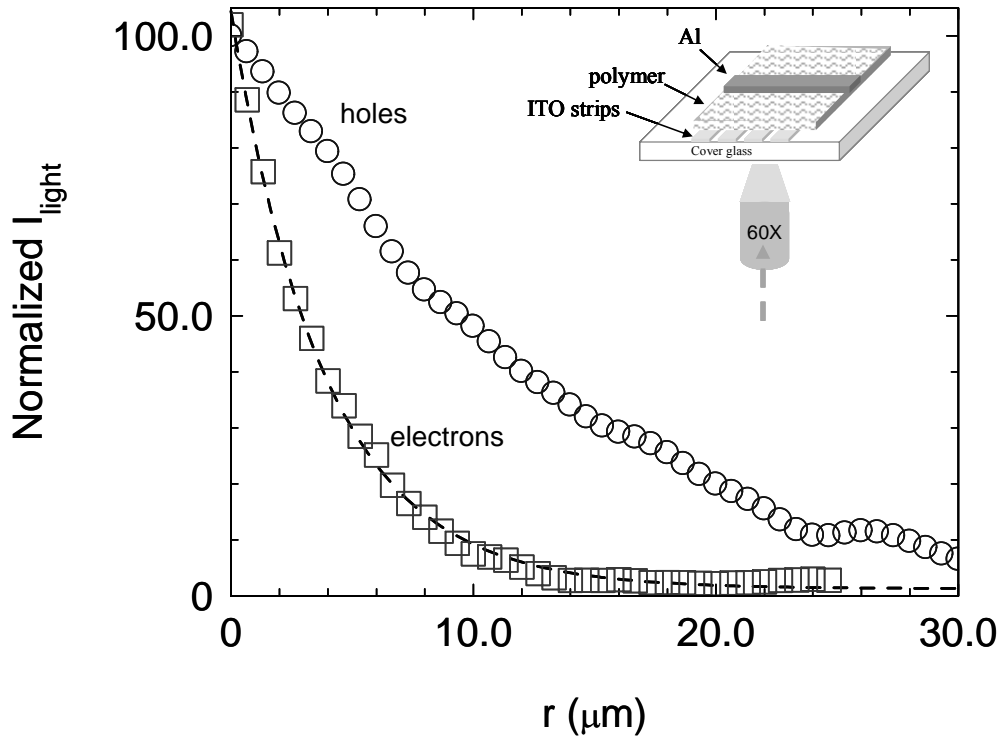


**Figure 4.5** Spatial photocurrent decay profiles for  $I_{\text{th}}(r)$  (o) and  $I_{\text{te}}(r)$  ( $\square$ ) on unoriented polymer chains. Excitation beam spot diameter  $\approx 400$  nm, wavelength = 470 nm, optical power  $\approx 100$  nW. Dashed line is an exponential fit to experimental data

These measurements required very crucial optical alignments in order to avoid wave - guiding at glass/air or glass/polymer interfaces and scattering process. While assembling this setup special care was taken in terms of retrace optical path of laser beam, normal incidence and monocular was used to position the focused optical beam on patterned device structures.



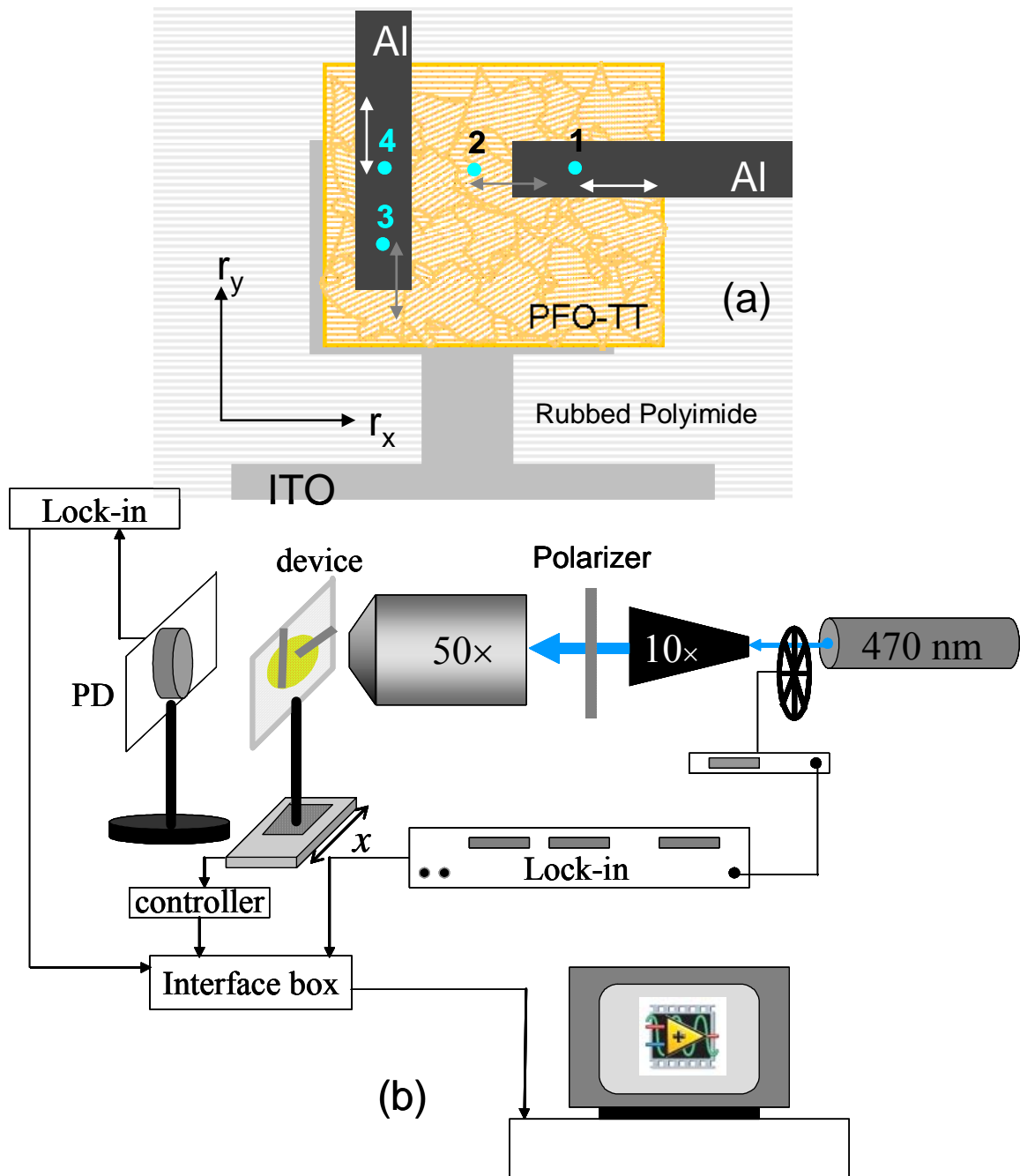


**Figure 4.6** (a) A typical device structure design for determination of transport length scales: 1 for  $L_{dh}(r_x)$ , 2 for  $L_{de}(r_x)$ , 3 for  $L_{de}(r_y)$  and 4<sup>th</sup> for  $L_{dh}(r_y)$  for oriented PFO–TT chains on rubbed PI alignment layer in  $r_x$  direction (b) A modified 1D spatial photocurrent profile setup with an addition of polarizer to investigate an optical anisotropic system.

The device structure used to study the spatial anisotropic behavior for electrons and holes is shown in **Figure 4.6**. The short circuit photocurrent profiles were obtained for the optical beam scanning directions (i) in  $r_x$  along center of horizontal Al strip for  $L_{dh}(r_x)$  as indicated by 1, (ii) in  $r_x$  along ITO moving away from edge of horizontal Al strip for  $L_{de}(r_x)$  as indicated by 2, (iii) in  $r_y$  along ITO moving away from edge of vertical Al strip for  $L_{de}(r_y)$  as indicated by 3 and (iv) in  $r_y$  along center of vertical Al strip for  $L_{dh}(r_y)$  as indicated by 4, in **Figure 4.6**. These scans were carried out for light polarization axis along orientation direction ( $r_x$ ) of polymer chains. Light polarized perpendicular to oriented polymer chains direction was found to provide similar photocurrent decay profiles with photocurrent magnitudes  $\sim 4$  times lesser than parallel-polarized light excitation. These measurements revealed that optical beam polarization primarily enhance the charge carrier generation due to corresponding absorbance and of lesser consequence in photogenerated charge carrier transport process. This magnitude difference can be entirely attributed to high absorption coefficient for parallel-polarized photo-excitation. Normalized spatial short circuit photocurrent decay profiles for holes ( $I_{lh}(r)$ ) and electrons ( $I_{le}(r)$ ) in  $r_x$  and  $r_y$  directions are shown in **Figure 4.7(a & b)**. These decay profiles not only represent the asymmetric transport behavior for electrons and holes ( $L_{dh} > L_{de}$ ) but also provides a clear evidence of the electrical anisotropy for electrons and holes in terms of enhanced transport lengths in the direction of polymer chains orientation ( $L_d(r_x) > L_d(r_y)$ ). In aligned polymer chains devices, observed decay lengths were found to be high as compare to unaligned polymer chains. This enhanced transport character along with comparable decay lengths of both photogenerated charge carriers are main results of these studies.

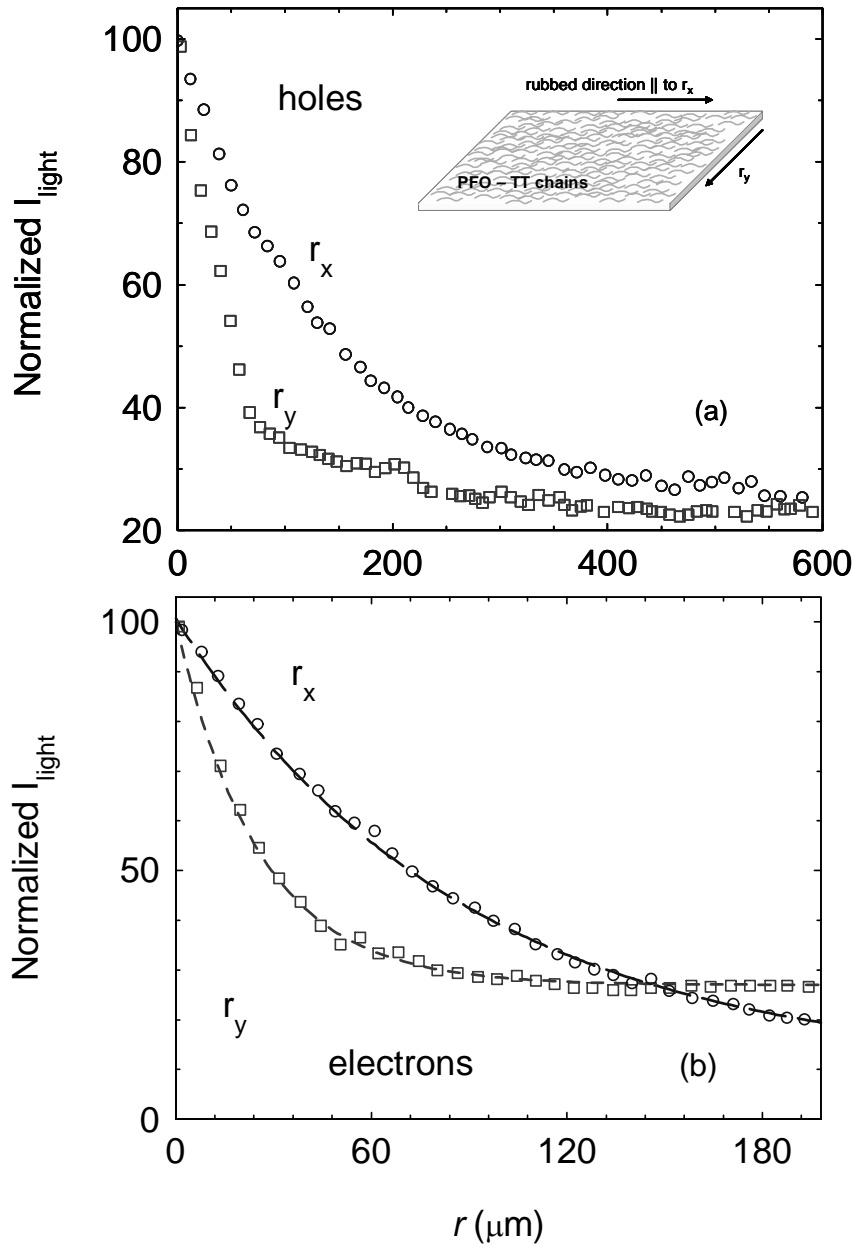


**Figure 4.7** Spatially anisotropic electrical transport in PFO – TT. (a) Schematic depicting orientation of PFO-TT polymer chains on ITO coated rubbed polyimide substrates. Spatial dependence of  $I_{\text{th}}(r_x)$  parallel and  $I_{\text{th}}(r_y)$  perpendicular, to rubbed directions, when light (laser beam diameter  $\sim 2 \mu\text{m}$ ,  $\lambda = 473 \text{ nm}$ , power =  $16 \mu\text{W}$ , polarization  $\parallel$  to rubbed direction) is incident on non-overlapping Al segment of the polymer film. (b) set of  $I_{\text{e}}$  measurements with light incident on non-overlapping ITO segment of the polymer film. The origin ( $r_{x,y} = 0$ ) for the region is determined from simultaneous-transmission measurements.

Dark electrical conductivity on aligned PFO-TT chains based planar device structures revealed anisotropic electrical transport induced from conformational packing of polymer chains on macroscopic scale. The device structure used for measurements consisted of two pair of Au electrodes - one perpendicular to rubbed direction for parallel charge transport and other parallel to rubbed direction for perpendicular charge transport measurements, as shown in inset of **Figure 4.8**. A schematic of preferred direction ( $r_x$ ) of alignment of polymer chains on rubbed polyimide alignment layer is shown in **Figure 4.8** along with I-V plots for charge transport parallel and perpendicular to orientation direction. These measurements were carried out under dark condition using typical I-V measurements experimental setup.

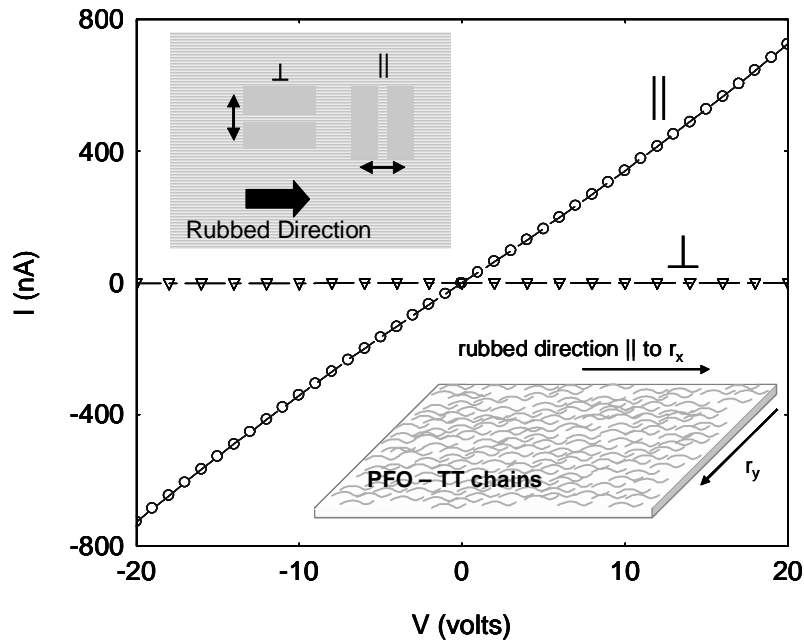


**Figure 4.8** I-V measurements for oriented PFO-TT film on rubbed polyimide layer along with a schematic of aligned hairy rods like PFO-TT chains and typical device structure. The channel gap and width of electrodes was  $40 \mu\text{m}$  and  $1 \text{mm}$ , respectively.

These results did not match with photoconductivity anisotropy measurements for similar device structure on irradiating with GaN diode laser ( $I_{\text{light, } \parallel} / I_{\text{light, } \perp} \neq I_{\text{dark, } \parallel} / I_{\text{dark, } \perp}$ ). This discrepancy can be explained based on different injection efficiency under dark conditions for polymer chains parallel and perpendicular to electric field direction. On the

other hand, in case of excitation with an unpolarized light source photo-injection is independent of chain directions.

## 4.4 Discussion

The advantages and the utility of our scanning  $I_{\text{light}}$  approach are particularly evident in case of anisotropic systems such as PFO-TT. This rod-like polymer system consists of a rigid backbone, which can result in a nematic liquid crystalline film on rubbed ( $r_x$ -direction) polyimide surfaces [9]. The intrinsic bulk optical properties such as absorption and fluorescence are highly anisotropic since the single molecule tensor and the orientational transformation matrix, which relates the molecular and macroscopic axes, determine the macroscopic tensor. Their elements are linked with oriented order parameters characterizing the orientation distribution function of the PFO-TT chains. The anisotropic feature appears in the photocurrent measurements.  $I_{\text{light}}$  is a bulk process with the total efficiency governed by the carrier generation process and the subsequent transport of the charge carriers. The polarization dependence of  $I_{\text{light}}$  is essentially an indicator of the charge carrier generation processes with the latter processes of transport independent of polarization of the incident light.  $I_{\text{light}}$  with light incident on a typical solar cell type sandwich structure (in the overlapping, uniform electric field region) reveals a charge collection efficiency ratio  $I_{\text{light}\parallel}/I_{\text{light}\perp} \approx 5$ .

**Table 4.1** Decay lengths for electrons ( $L_{de}$ ) and holes ( $L_{dh}$ ) extracted from exponential fits to  $I_{\text{light}}(r)$  ( $\tau\mu$ )<sub>hole</sub>/ $(\tau\mu)$ <sub>electron</sub> ratio estimated from  $(L_{dh}/L_{de})^2$

Polymer	decay length ( $L_{de}$ ) from $I_{\text{le}}(r)$	decay length ( $L_{dh}$ ) from $I_{\text{lh}}(r)$	$\mu_h\tau_h/\mu_e\tau_e$
unoriented PFO –	3.9 $\mu\text{m}$	14.1 $\mu\text{m}$	3.6
PFO – TT ( $r_x$ ) polarization $\parallel$ to $r_x$	87.3 $\mu\text{m}$	134 $\mu\text{m}$	2.4
PFO – TT ( $r_y$ ) polarization $\parallel$ to $r_x$	25.5 $\mu\text{m}$	50.3 $\mu\text{m}$	3.9

On the other hand, the anisotropy in the charge transport processes measured by scanning the beam along two different directions with the asymmetrically positioned electrodes identifies the electrical anisotropy prevailing in this oriented system. For light parallel to the oriented direction, the scanning probe  $I_{\text{light}}$  measurements for  $I_{\text{lh}}(r_x)$  and  $I_{\text{lh}}(r_y)$  indicate a spatial anisotropy  $L_{\text{dh}(rx)}/L_{\text{dh}(ry)}$  for holes transport  $\approx 2.6$ . The spatial anisotropy for electrons  $L_{\text{de}(rx)}/L_{\text{de}(ry)}$  is higher,  $\approx 3.5$ , implying a larger confinement for the electrons along the chain direction or a higher interchain hopping probability for the holes. The results obtained for the polarization perpendicular to the oriented direction indicate lower magnitude for  $I_{\text{lh}}$  and  $I_{\text{le}}$  along with differences in the spectral features as shown in **Figure 4.3**, but the spatial anisotropy is maintained with similar values.

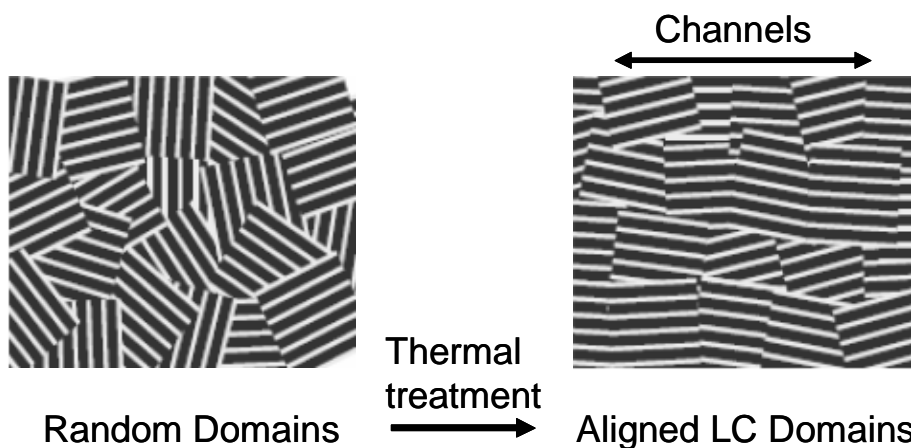


**Figure 4.9** A schematic of conformational change due to thermal treatment in PFO-TT film spin coated on aligned PI layer

**Table 4.2** Electrical anisotropy in oriented polymer film

Material → Parameter	(Oriented PFO-TT) <sub>∥</sub>	(Oriented PFO-TT) <sub>⊥</sub>	Anisotropy {(μτ) <sub>∥</sub> /(μτ) <sub>⊥</sub> }
$L_{\text{de}}$ (μm)	87.3	25.5	11.7
$L_{\text{dh}}$ (μm)	134.0	50.3	15.4

In essence,  $I_{\text{light}}$  measurements in the sandwich cell reflect the trend in the absorption, PL and EL with  $I_{\text{light}\parallel} > I_{\text{light}\perp}$  in these oriented films. A fundamental question in these systems is related to the extent of interchain interactions and the reduced recombination probability in a higher dimensional organization compared to a 1-D intrachain process. This is partly answered by the spatial variation of the  $I_{\text{light}}$  in the non-overlapping electrode regions. The larger  $L_{\text{dh}}$  for either polarization directly arises from the order-induced higher  $\mu\tau$  product in the orientation direction, i.e.;  $L_{\text{d}(\text{rx})} > L_{\text{d}(\text{ry})} \Rightarrow (\mu\tau)_{\text{rx}} > (\mu\tau)_{\text{ry}}$  for these devices (**Figure 4.7 & Table 4.2**), which is also found in case of FET structures [10, 12] and in photoconductivity measurements [19] of polyfluorene film.

## 4.5 Summary

In summary, structural ordering of polymer chains improves the photogenerated charge carriers transport processes in nematic liquid crystalline oriented polymer films. The results obtained from these studies give an insight of interchain and intrachain hopping processes occur in these materials. Mobility-lifetime product was found to be an order higher, for both electrons and holes, in the case of intrachain transport (transport along aligned chains direction). Decay length ratios for electron and holes were found to be an evidence for higher degree of ambipolar conduction. Enhanced transport in aligned direction and higher degree of ambipolar conduction compliment this material for good performance optoelectronic devices. These studies envision the use of this polymer for polarization photo-sensor, polarized light emitting diodes and light-emitting transistors.

## References

---

- [1] I. McCulloch, M. Heeney, C. Bailey, K. Genevicius, I. MacDonald, M. Shkunov, D. Sparrowe, S. Tierney, R. Wagner, W. Zhang, M. L. Chabiny, R. J. Kline, M. D. McGehee, M. F. Toney, *Nat. Mat.* **5**, 328 (2006)
- [2] S. Kuroda, T. Nogachi, T. Ohnishi, *Phys. Rev. Lett.* **72**, 286 (1994)
- [3] D. H. Kim, Y. D. Park, Y. Jang, H. Yang, Y. H. Kim, J. I. Han, D. G. Moon, S. Park, T. Chang, C. Chang, M. Joo, C. Y. Ryu, K. Cho *Adv. Funct. Mater.* **15**, 77 (2005).
- [4] D. H. Kim, Y. Jang, Y. D. Park, K. Cho, *Macromolecules* **39**, 5843 (2006).
- [5] X. Long, A. Malinowski, D. D. C. Bradley, M. Inbasekaran, E. P. Woo, *Chem. Phys. Lett.* **272**, 6 (1997)
- [6] M. N. Shkunov, R. Osterbacka, A. Fuji, K. Yoshino, Z. V. Vardeny, *Appl. Phys. Lett.* **74**, 1648 (1999)
- [7] M. Grell, D. D. C. Bradley, *Adv. Mater.* **11**, 895 (1999)
- [8] M. Knaapila, K. Kisko, B. P. Lyons, R. Stepanyan, J. P. Foreman, O. H. Seeck, U. Vanio, L. -O. Palsson, R. Serimaa, M. Torkkeli, A. P. Monkman, *J. Phys. Chem. B* **108**, 10711 (2004)
- [9] L. R. Pattison, A. Hexemer, E. J. Kramer, S. Krishnan, P. M. Petroff, D. A. Fischer, *Macromolecules* **39**, 2225 (2006)
- [10] H. Sirringhaus, R.J. Wilson, R. H. Friend, M. Inbasekaran, W. Wu, E. P. Woo, M. Grell, D. D. C. Bradley, *Appl. Phys. Lett.* **77**, 406 (2000)
- [11] F. Yan, Y. Hong, P. Migiliorato, *J. Appl. Phys.* **101**, 64501 (2007)
- [12] L. Kinder, J. Kanicki, P. Petroff, *Synth. Met.* **146**, 181 (2004)
- [13] U. Scherf, E. J. W. List, *Adv. Mat.* **14**, 477 (2002)
- [14] A. J. Cadby, P. A. Lane, H. Mellor, S. J. Martin, M. Grell, C. Giebeler, D.D.C. Bradley, M. Wohlgenannt, C. An, Z. V. Vardeny, *Phys. Rev. B* **62**, 15604, (2000)
- [15] M. Grell, D. D. C. Bradley, X. Long, T. Chamberlain, M. Inbasekaran, E. Woo, M. Soliman, *Acta. Polym.* **49**, 439 (1998)
- [16] H. G. Nothofer, Ph.D. thesis, University Potsdam, Germany 2001
- [17] Logos Verlag, Berlin, 2001, ISBN 3-89722-668-5



- 
- [18] M Bernius, M Inbasekaran, E Woo, W Wu, L Wujkowski, *J. Mater. Sci. Mater. El* **11**, 111 (2000)
- [19] F. C. Grozema, T. J. Savenije, M. J. W. Vermeulen, L. D. A. Siebbeles, J. M. Warman, A. Meisel, D. Neher, H. -G. Nothofer, U. Scherf, *Adv. Mat.* **13**, 1627 (2001)
- [20] M. Grell, D. D. C. Bradley, X. Long, T. Chamberlain, M. Inbasekaran, E. P. Woo, M. Soliman, *Acta Polym.* **49**, 439 (1998)
- [21] M. N. Bussac and L. Zuppiroli, *Phys. Rev. B* **54**, 4674 (1996)
- [22] M. Grell, D. D. C. Bradley, *Adv. Mater.* **11**, 895 (1999)
- [23] G. Greczynski, M. Fahlman, W. R. Salaneck, *J. Chem. Phys.* **113**, 2407 (2000)
- [24] M. Grell, D. D. C. Bradley, *Adv. Mater.* **11**, 895 (1999)



# CHAPTER 5

## Studies of Charge Carrier Dynamics using Lateral Photovoltaic Effect: Position Sensitive Detectors

### 5.1 Introduction

Conjugated polymer based semiconductors have been explored for their utility in optoelectronic applications. A comprehensive understanding of the dynamics involving the energy dependent diffusion and drift processes of the photogenerated carriers in these materials is essential for development of optoelectronic devices. The phenomenon of lateral photovoltaic effect (LPE) has proved to be an effective probe for photogenerated charge carrier dynamics in conventional inorganic semiconductors [1, 2]. The LPE primarily arises due to non-uniform illumination of Schottky or  $p-n$  junction diodes, a phenomenon first reported by Schottky [3].

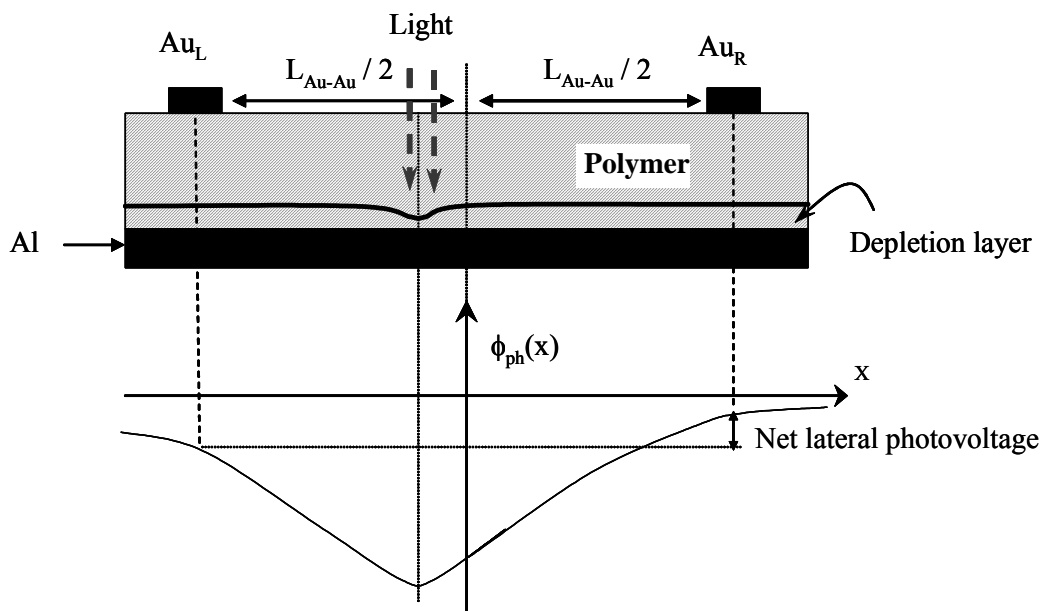


**Figure 5.1** A non-uniform illumination results in lateral photovoltaic effect and steady state transverse potential profile in polymer film, when the light spot is closer to Au<sub>L</sub>.

Although well established in the case of inorganic semiconductor devices, LPE has not been exploited hitherto for organic semiconductor based systems. This is surprising considering the ubiquity of this phenomena (LPV is observed in almost every semiconducting polymer system in our laboratory). The relevance and impact of these studies in the organic systems is quite significant, since the magnitude of this effect turns out to be a direct measure of the electrical characteristics.

This effect has been used for investigating charge carrier dynamics in organic systems besides using it for other applications such as position sensing. In this chapter, a comprehensive experimental and modeling aspect of this lateral photovoltage effect (LPV) is presented, which has temperature dependence, frequency response, wavelength dependence, in a wide variety of device structures. In order to correlate the spatiotemporal dependence of the LPV with the microscopic processes involved, a spreading impedance (SI) approach was employed in the context of a discrete circuit element model [4, 5]. It is known that the SI profiling is directly related to the carrier profile in traditional semiconductors [6,7]. Carrier density profile is a much sought-after quantity to understand various phenomena in organic systems including field effect transport and transient photoconductivity. An excellent quantitative agreement between theory and experiment is demonstrated for positional dependence and frequency response of the lateral photovoltage. These results lend further support to the essential veracity of the underlying theoretical framework. The resultant potential profile was used to infer the steady state charge carrier distribution in the polymeric semiconducting films, which is subsequently used to form a consistent picture of charge carrier transport in these systems. Furthermore, these LPV measurements directly indicate the utility of such device structures as large area, flexible position sensors. This chapter includes the experimental procedure and details discussions on the underlying physics of the Schottky contact and charge carrier transport in polymer films. A parallel approach developed around a discrete circuit element model [4] is also included.

The lateral photoeffect is widely applied in applications related to robotic vision, machine tool alignment, and guidance systems. The advantage of PSDs over those fabricated from photodetector arrays is in their inherent simplicity for measuring beam position without the resolution being limited by detector size. Additionally, a thin film linear PSD consists of two line electrodes separated by a distance  $L_{\text{Au-Au}}$ , and a common back electrode, whereas detector arrays require a complex multiplexing architecture such as used in charge coupled arrays. A typical one-dimensional (1D) PSD operation involves a variation of the difference in the short-circuit current from the two arms as a function of the beam position with a minima located at the center of the inter electrode region [8].

## 5.2 Photophysics of LPV and Discrete Circuit Element Model

Upon photoexcitation of semiconducting polymers, the primary source for generating the charge carriers arises from the loosely bound electron-hole pairs [9]. These excitons dissociate in the vicinity of polymer-Al metal interface under the influence of the built-in Schottky type barrier potential within the depletion zone. Subsequently, the electrons are transferred to the equipotential Al electrode, leaving the excess photogenerated holes in active polymer network. The photoactivity can be primarily restricted to the interface region by selecting the wavelength corresponding to the band-edge region. The separated holes at the interface distort the built-in potential locally, which in the steady state sets up a non-local lateral electric field that self consistently induces a lateral flow of the separated holes. This lateral charge flow, which is ohmic in nature ( $\text{Au}_L/\text{P3HT}/\text{Au}_R$  I-V plot was found to be straight line), produces a potential drop between the locus of illumination and the electrodes. If the locus is asymmetrically located between the electrodes, a non-zero lateral photovoltage is developed, as shown schematically in *Figure 5.1*.

There is a variation in the potential along the transverse direction. However, to build a model with minimum complexities transverse potential profile has been assumed uniform, as this model primarily seeks to explain the large lateral effect involving lateral lengths ( $L_{\text{Au-Au}}$ )  $\gg$  thickness of sample ( $t$ ). On the other hand, the region outside the

barrier width is assumed to have a homogeneous transverse potential profile, as  $t \gg$  depletion barrier width ( $w_d$ ), which is the photoactive region. The lateral potential profile  $\phi_{ph}(r)$  is then discretized onto a square lattice of nodes, each node element  $m$  represented by a potential  $\phi_m$ . The current through each node has a transverse and a lateral component as described below.

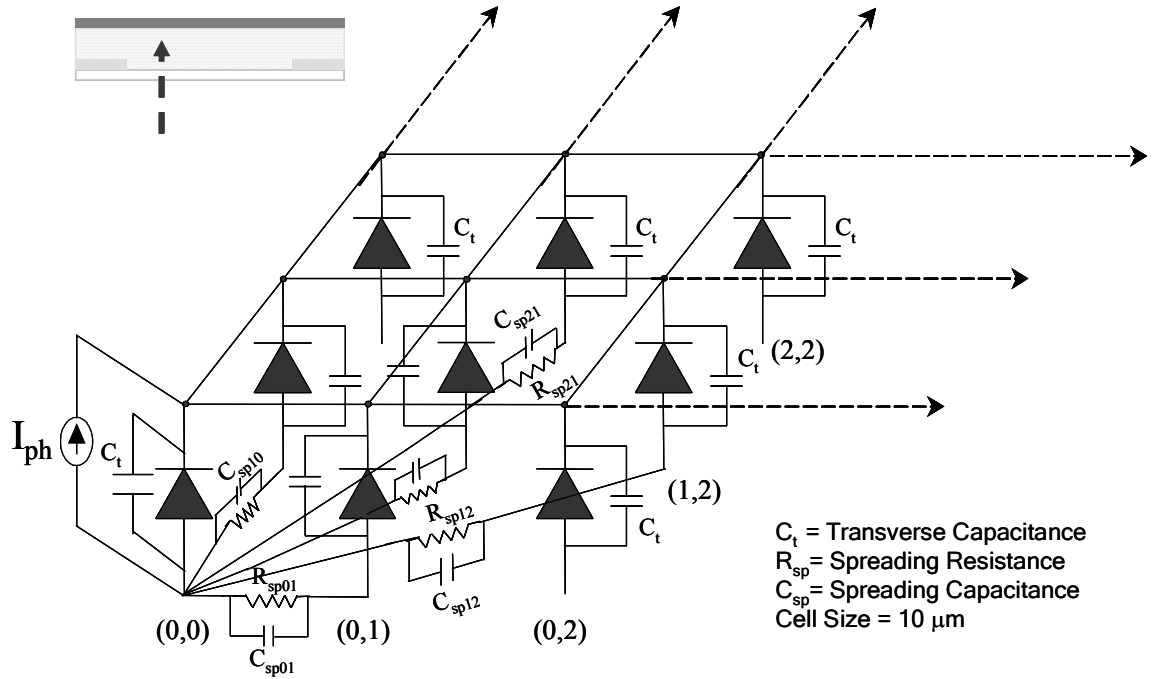


**Figure 5.2** Discretization of the device structure using circuit elements where  $I_{ph}$  represents current source at the location where light is incident. Diodes with  $C_t$  represents polymer/Al Schottky interface and lateral network  $R_{sp}$  &  $C_{sp}$  parallel combination represents polymer matrix.

(A) The transverse currents through the node,  $m$ , comprises the reinjection of electrons made possible by the reduction in the barrier potential of the Schottky type junction. This is modeled as a combination of a diode and capacitive current (**Figure 5.2**).

The diode current is given by

$$I_{D,m}^T = I_s (\exp(q\phi_m / k_B T) - 1) \quad (5.1)$$

where  $I_s$  = reverse saturation current for Schottky diode.

The current through the transverse capacitance ( $C_t$ ), associated with Schottky interface, is given by

$$I_{C,m}^T = C_t \frac{d\phi_m}{dt} \quad (5.2)$$

For the illuminated nodes, the photogenerated holes add to the transverse incoming current and represented by a current source  $I_{ph,m}$ , the magnitude of which would naturally depend on the locus and the beam profile in the medium and the quantum efficiency. Constant beam intensity within a radius  $r_{beam}$  from the centre of the beam is used.

(B) The lateral charge flow is modeled using a spreading impedance approach. Within this approach, the holes generated in the illuminated region (IR) drift outward and this charge-flow in the steady state constitutes the lateral current between the illuminated and the dark regions [4]. The lateral current has two components as well: a resistive part arising due to the disorder scattering of charge carriers and a capacitive component attributable to trap states, which affect the traversal times of charge carriers and hence the response time of device.

The resistive component of the current from node  $m$  to  $n$  is given by

$$I_R^L = \frac{\phi_m - \phi_n}{R_{sp}(m,n)} \quad (5.3)$$

while the capacitive component is given by

$$I_C^L = C_{sp}(m,n) \frac{d(\phi_m - \phi_n)}{dt} \quad (5.4)$$

where  $R_{sp}$  and  $C_{sp}$  are the inter-node spreading resistance and capacitance respectively. Modeling of these quantities is one of the central aspects of the spreading impedance approach, as follow.

For highly disordered systems like the organic polymers considered here, the number of scattering centers between any two nodes is expected to increase much more rapidly with the internode distance  $r_{mn} \equiv |\vec{r}_m - \vec{r}_n|$  than for their crystalline counterparts. This can be taken into account in a mean field manner by defining a spreading function (SF) denoted as  $g(r_{mn})$ , that in its dependence on  $r_{mn}$  would reflect the connectivity and microscopic structure of the underlying polymer matrix; and interpreted as an effective internode distance. While a specific form of the SF is discussed later in simulation

section, the general definition of  $g(r)$  allows us to model the spreading impedances used in equations (5.3) and (5.4) as:

$$\left. \begin{aligned} R_{sp}(m, n) &= R_s g(r_{mn}) \\ C_{sp}(m, n) &= \frac{C_s}{g(r_{mn})} \end{aligned} \right\} \quad (5.5)$$

where  $R_s$  and  $C_s$  are the sheet resistance and sheet capacitance, respectively and  $r_{mn}$  is the distance between nodes  $m$  and  $n$ . These terms are largely borrowed from inorganic semiconductor literature as in [4], where polycrystalline based Schottky diode has been used to demonstrate spreading impedance in a comprehensive way.

A set of equations governing the charge flow in the device can be described as follows. For convenience, the set of all nodes are divided, denoted by ' $S_N$ ', into four mutually exclusive subsets depending on whether the specific node is illuminated or not, and whether it is a part of an electrode or not:

- (i)  $S_{IL}$ : set of nodes those are illuminated
- (ii)  $S_{NIL}$ : set of non-illuminated nodes and non-electrode nodes
- (iii)  $S_{LE}$ : set of nodes coincident with the left electrode
- (iv)  $S_{RE}$  represents the nodes that are coincident with the right electrode.

The system of equations determining the two dimensional potential profile  $\phi(r, t)$ , are obtained by a simple application of Kirchoff's law balancing the lateral and transverse currents at each node of this spreading impedance network. Each of the sets defined above are separately.

For the dark or non-illuminated electrode node,  $m \in S_{NIL}$ , the total incoming transverse current is the sum of currents through diode and  $C_t$ :

$$I_{dark, m}^T = -I_s \left[ \exp\left(\frac{q\phi_m}{k_B T}\right) - 1 \right] - C_t \frac{d\phi_m}{dt} \quad (5.6)$$

while the total incoming lateral current at  $m$  is the sum of currents from each of the illuminated nodes:

$$I_{dark, m}^L = \sum_{l \in S_{IL}} \left[ \frac{\phi_l - \phi_m}{R_{sp}(l, m)} + C_{sp}(l, m) \frac{d(\phi_l - \phi_m)}{dt} \right] \quad (5.7)$$



Since the total incoming current at a dark node should vanish due to the absence of a source, the final equation for any  $m \in S_{NIL}$  is

$$I_{dark,m}^T + I_{dark,m}^L = 0 \quad (5.8)$$

For an illuminated node,  $l \in S_{IL}$ , the transverse component would have an additional current source,  $I_{ph,l}$  representing the charge carriers per unit time produced by the incident light beam at node  $l$ :

$$I_{ill,l}^T = -I_s \left[ \exp\left(\frac{q\phi_l}{k_B T}\right) - 1 \right] - C_t \frac{d\phi_l}{dt} + I_{ph,l} \quad (5.9)$$

The lateral current comprises of the current flow to all the other nodes through the spreading impedances:

$$I_{ill}^L = - \sum_{m \in S_N, m \neq l} \left[ \frac{\phi_m - \phi_l}{R_{sp}(m,l)} + C_{sp}(m,l) \frac{d(\phi_m - \phi_l)}{dt} \right] \quad (5.10)$$

Thus the current balance at node  $l \in S_{IL}$  gives

$$I_{ill,l}^T = I_{ill,l}^L \quad (5.11)$$

The sum over all nodes  $\sum_{m \in S_N}$  appearing in Eq. (5.10) above may be split into four parts corresponding to the four sets defined above:

$$\sum_{m \in S_N} = \sum_{m \in S_{IL}} + \sum_{m \in S_{NIL}} + \sum_{m \in S_{LE}} + \sum_{m \in S_{RE}} \quad (5.12)$$

The electrodes are equipotential; hence, all the nodes falling on the left electrode would have the same potential,  $\Phi_L$ , while those on the right electrode would have the potential  $\Phi_R$ . the expression determining  $\Phi_L$ , may be obtained in a similar way as Eqs. (5.6 – 5.11) and is given by:

$$\sum_{m \in S_{LE}, l \in S_{IL}} \left[ \frac{\Phi_L - \phi_l}{R_{sp}(m,l)} + C_{sp}(m,l) \frac{d(\Phi_L - \phi_l)}{dt} \right] = N_L \left[ I_s \left\{ \exp\left(\frac{q\Phi_L}{k_B T}\right) - 1 \right\} + C_t \frac{d\Phi_L}{dt} \right] \quad (5.13)$$

where  $N_L$  = number of nodes on the left electrode.

The equation for  $\Phi_R$  is obtained by replacing  $\Phi_L$  with  $\Phi_R$  in Eq. (5.13) above. Thus, Eqs. (5.8, 5.11, 5.13) along with the equation for  $\Phi_R$  is a complete system of linear coupled

differential equations, which upon solving would determine not only the LPV ( $\Delta V_{ph}$ ) defined by

$$\Delta V_{ph} = |\Phi_L - \Phi_R| \quad (5.14)$$

but also the two dimensional potential profile  $\phi(r,t)$ . The differential equation in time may be converted into non-linear algebraic equations using the Fourier transform for  $\phi(r,t)$  and  $I_{ph}(r,t)$ . Additionally, in small signal limit ( $q\phi \ll k_B T$ ), the diode current may be linearized into following linear complex-system of equations:

$$S_{NIL} : \quad \left[ \frac{I_s q}{k_B T} + i\omega C_t \right] \phi_m + \sum_{l \in S_{IL}} \frac{\phi_m - \phi_l}{Z_{sp}(m,l)} = 0 \quad (5.15)$$

$$S_{IL} : \quad \left[ \frac{I_s q}{k_B T} + i\omega C_t \right] \phi_l + \sum_{m \in S_N, m \neq l} \frac{\phi_l - \phi_m}{Z_{sp}(m,l)} = I_{ph,l} \quad (5.16)$$

$$S_{LE} : \quad N_L \left[ \frac{I_s q}{k_B T} + i\omega C_t \right] \Phi_L + \sum_{m \in S_{LE}, l \in S_{IL}} \frac{\Phi_L - \phi_l}{Z_{sp}(m,l)} = 0 \quad (5.17)$$

$$S_{RE} : \quad N_R \left[ \frac{I_s q}{k_B T} + i\omega C_t \right] \Phi_R + \sum_{m \in S_{RE}, l \in S_{IL}} \frac{\Phi_R - \phi_l}{Z_{sp}(m,l)} = 0 \quad (5.18)$$

where  $i = \sqrt{-1}$  and the spreading impedance  $Z_{sp}(l,m) = (1/R_{sp}(l,m) + i\omega C_{sp}(l,m))^{-1}$ .

The full two-dimensional potential profile is obtained as the real part of the solution of a linear system of equations (Eq. 5.15 – 5.18) with complex coefficients. An efficient numerical implementation is carried out by eliminating the dark region potentials analytically (from Eq. 5.15) in favor of the illuminated node potentials in the following way

$$\phi_m = \left[ \frac{I_s q}{k_B T} + i\omega C_t + \sum_{l \in S_{IL}} \frac{1}{Z_{sp}(m,l)} \right]^{-1} \sum_{l \in S_{IL}} \frac{\phi_l}{Z_{sp}(m,l)} \quad (5.19)$$

and then substituting these in equations for the nodes in the illuminated region (Eq. 5.16). In the model presented above, no assumptions are made about the specific shape or position of the electrodes and the polymer-metal interface; hence, it is applicable to

arbitrary sample geometries. This approach can easily be extended to 2-D device configurations, which has been realized experimentally.

### 5.3 Route to LPV Observations

The LPV phenomena was initially arrived and understood from an experimental measurement approach. The sequence of measurements commenced from two probe DC conductivity and photoconductivity measurements of the polymer film coated on a pair of underlying Au electrodes separated by a distance  $L_{\text{Au-Au}}$ . It was noticed that the measurements radically altered on introducing an Al electrode coating in between the Au electrodes. It was expected that an introduction of Al layer would alter the dark conductivity and photoconductivity of polymer film. An increase in the  $I_{\text{photocurrent}} / I_{\text{dark}}$  was observed as compared to pristine Au–polymer–Au structures. This trend indicated the barrier formation at interface with the low workfunction metals such as Al or Mg [10]. The origin of the barrier in terms of oxide formation or the degree of the Schottky character is difficult to quantify exactly due to the combinations of physical and chemical processes which come into play upon the formation of the interface. These Schottky gated three terminal planar device structures are analogous to metal-semiconductor field effect transistor (MESFETs) structures. However, gate bias dependent conductivity change was not observed. A characteristic of a Schottky-type contact is the presence of a thin depletion layer where the thickness depends on diffusion potential:  $\sqrt{(2\epsilon\epsilon_0 V_d / eN_d)}$  where,  $V_d$  is the diffusion potential and all other symbols have their usual meaning [11]. In the polymer MESFET type structures, band bending modulation was not observed with an external bias and can be possibly ascribed to interfacial defects states. P3HT polymer HOMO ( $\sim -2.9$  eV) – LUMO ( $\sim -5.0$  eV) level positions and work function of Al metal ( $-4.2$  eV) in ideal conditions should make Schottky interface but chemical interaction of polymer chain with metal and unintentional oxide layer formation results in an imperfect Schottky type interface [12]. At the interface formed by Al and polythiophene, Al can react with both sulphur atoms and carbon atoms in the backbone of thiophene units [13], which forms a disruptive interface. However, an external bias

(reverse bias, i.e., positive bias to Al) was found to promote exciton dissociation leading to a larger fraction of photogenerated charge carriers. A set of experiments were carried out to obtain a comprehensive understanding of photo-physical processes involved to generate LPV in polymer systems. P3HT polymer was used for most of the studies due to its good lateral transport properties in 2D plane [14]. However, MEHPPV was also used for PSD studies. The comparison of the two polymers in the same geometry yields useful information (for example HOMO-LUMO level gap  $\sim 2.2$  eV, dielectric constant  $\sim 3.5$ , film thickness, similar device structure). A complete list of experiments is as follows:

- I. Photocurrent Spectroscopy
- II. Wavelength dependence
- III. I-V measurements
- IV. Channel Length Dependence
- V. Chopper Frequency Dependence
- VI. Temperature Dependence
- VII. External Bias Dependence
- VIII. 2D optical scanning

### 5.3.1 Photocurrent Spectroscopy

Light intensity modulated photocurrent spectroscopy measurements were carried out on photovoltaic structures for illumination from glass side and from semitransparent Al electrode side. In this case, light was irradiated uniformly throughout the device, a short circuit photocurrent was obtained using lock-in technique with experimental setup shown in *Figure 2.14*.

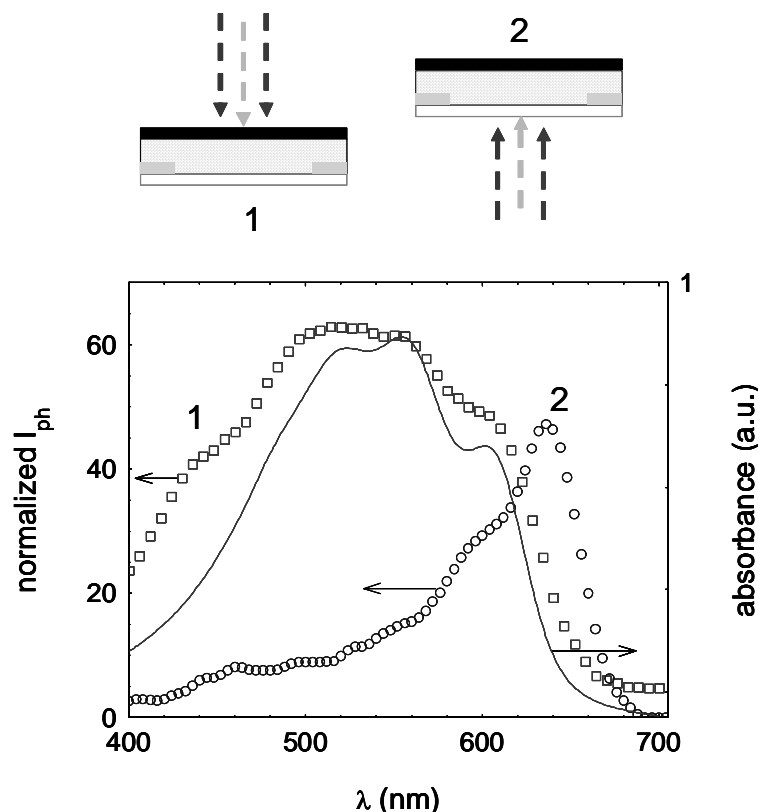


**Figure 5.3** Intensity modulated photocurrent spectrum,  $I_{ph}(\lambda)$ , for P3HT based three terminal device structure when light was irradiated from (1) glass side ( $\square$ ) and from (2) semitransparent Al side (o)

The  $I_{ph}(\lambda)$  for P3HT devices as shown in **Figure 5.3**, reveals a maximum in the band-edge region for illumination, from the glass side, suggesting predominant interfacial activity for charge carrier generation. This feature indicates the necessity of an efficient electron transfer to Al for generating large  $V_{ph}$ . The interfacial features and spectral dependence is indicative of small diffusion length of the excitons ( $\sim 10$  nm) [15]. These sets of measurements can be interpreted on the basis of the photoactivity and the electron transfer at the Al-polymer interface ( $I(z) = I_0 \exp(-\alpha(\lambda)z)$ , where  $I_0$  is intensity at the surface (either glass/polymer or Al/ polymer interface),  $z$  is transverse direction,  $\alpha(\lambda)$  is absorption coefficient and  $I(z)$  is light intensity profile in the  $z$  direction). A similar photocurrent behavior was observed for MEHPPV device with respect to excitation wavelength, which matched well with published reports [16].

### 5.3.2 Wavelength Dependence

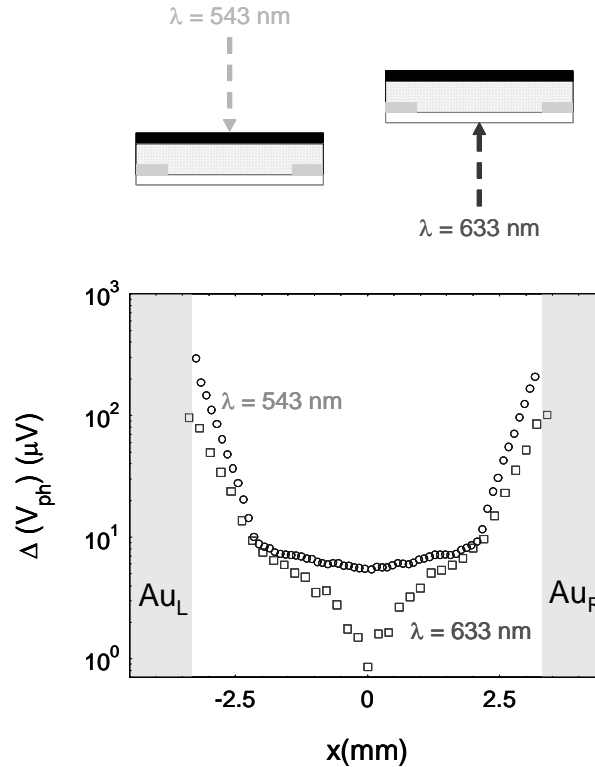


**Figure 5.4** Spatial profile of differential photovoltage  $\Delta V_{ph}$  ( $= |\phi_L - \phi_R|$ ) for illumination from glass side ( $\square$ ) and from semitransparent Al side ( $\circ$ ) with laser beam (spot diameter  $10 \mu\text{m}$ ) wavelength was  $633 \text{ nm}$  and  $543 \text{ nm}$ , respectively. Measurements were done using dual phase dual channel lock-in amplifier in photovoltaic mode.

For the 1-D P3HT based PSD (**Figure 5.1**), the measured  $\Delta V_{ph}(x)$  was found to be a smooth function with a minimum at  $x = 0$  and maximum at the two Au electrodes (**Figure 5.4**). The wavelength  $\lambda$  and the direction of incident-light also come into play in the  $\Delta V_{ph}(x)$  response. Conversely, for  $\lambda = 543 \text{ nm}$  corresponding to high absorption region for thick samples,  $t > 1/\alpha_{abs}(\lambda_{max})$ , with light incident from the glass side, the magnitude and the spatial dependence of  $\Delta V_{ph}(x)$  was relatively insignificant. However, upon having the  $532 \text{ nm}$  light source incident from the partially transparent Al side, reasonable  $\Delta V_{ph}(x)$  was observed. The model primarily explained the LPV results for  $\lambda = 633 \text{ nm}$ , where  $\alpha_{abs} \approx 10^3 \text{ cm}^{-1}$  and charge carrier generation, which is restricted to regions near the interface. The polymer film thickness ( $t$ ) was  $\sim 700 \text{ nm}$  and is  $> 1/\alpha_{abs}$

[where  $\alpha_{\text{abs}}$  (at  $\alpha_{\text{abs}}(\lambda_{\text{max}}) \approx 10^5 \text{ cm}^{-1}$ ]. Hence, charge carrier generation in the absorbing region does not represent interfacial charge carrier generation while illuminating from glass side.

### 5.3.3 I-V Characteristics

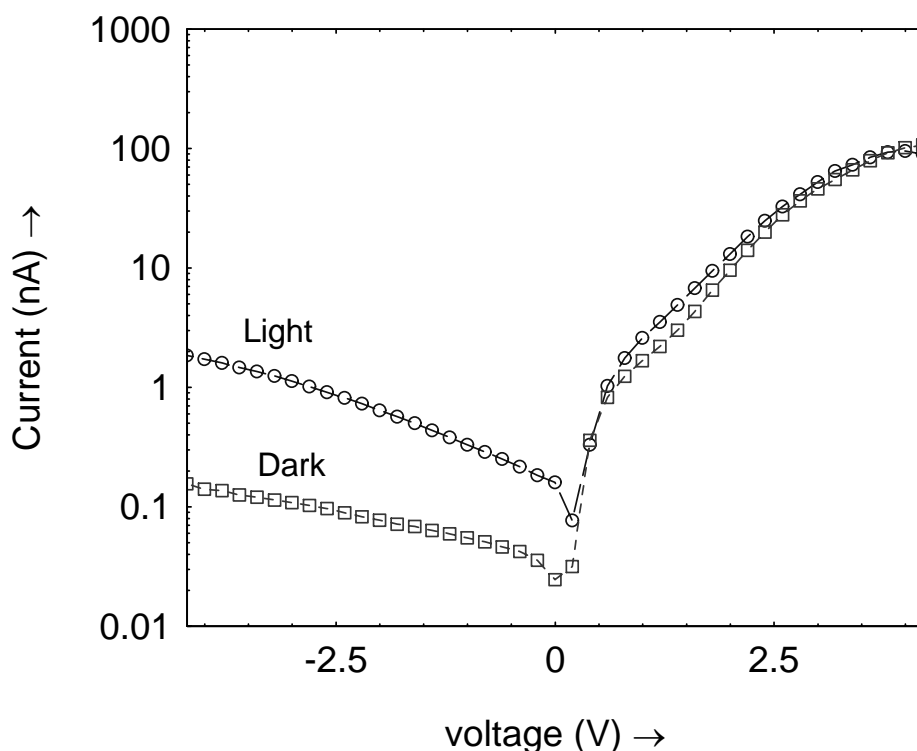


**Figure 5.5**  
Typical I-V characteristics for Au/P3HT/Al in dark and illumination condition (red He-Ne  $\lambda = 633 \text{ nm}$ , optical power  $32 \mu\text{W}$ ) for a PSD with  $L_{\text{Au-Au}} = 3 \text{ mm}$  &  $w = 1.5 \text{ mm}$ .

Current- voltage characteristics were carried out using experimental set up shown in **Figure 2.15** on  $\text{Au}_L/\text{P3HT}/\text{Au}_R$  planar structure. A linear response was observed (see **Figure 5.6**) which reveal Au/P3HT forms an ohmic contact. It can be further explained with the knowledge of work-function of Au (inert metal) and HOMO – LUMO levels of semiconducting polymer. The current that flows through polymer matrix between two Au electrodes is supposed to be relaxation time limited Ohmic in nature due to energetically disordered localized defects and traps sites. I-V measurements on shorted ( $\text{Au}_L\text{-Au}_R$ )/P3HT/ Al were also carried out which showed a rectifying character (see

Figure 5.5) in this device structure. These results indicate a Schottky type interface at P3HT/Al interface and Ohmic interface at Au/ P3HT interface.

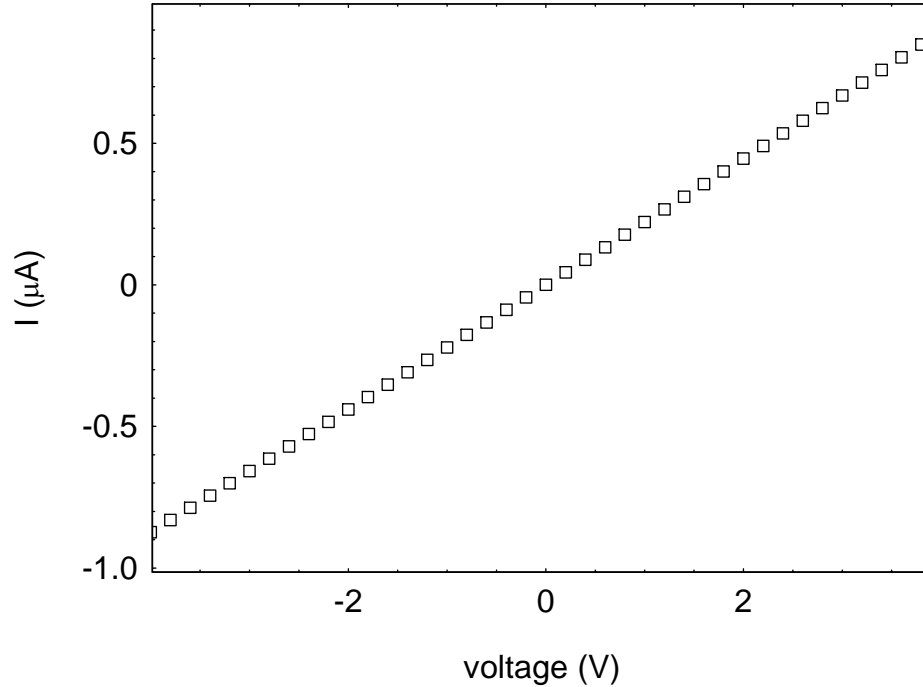


**Figure 5.6** Typical  $I$ - $V$  characteristics for  $Au_L/P3HT/Au_R$  in dark for a PSD with  $L_{Au-Au} = 3$  mm &  $w = 1.5$  mm, Al electrode was floating.

### 5.3.4 Channel Length Dependence of LPV

The length of active channel aspects of PSD structures, play decisive roles in the magnitude and the lineshape of LPV. It was observed that a linear lineshape of  $\Delta V_{ph}(x)$ , desirable for applications to PSD devices, can be obtained by having the geometrical parameters  $L_{Au-Au} \sim w$ , for a sizable range of  $L_{Au-Au}$  and  $w$  (25  $\mu$ m to 2 mm). For  $L_{Au-Au} > w$ , substantial nonlinearity in  $\Delta V_{ph}(x)$  was observed. These features are highlighted in **Figure 5.7a** where one clearly observes the linear dependence when  $L_{Au-Au} \sim w$ . Upon varying the  $L_{Au-Au}$ , for example by a factor of two for the same  $w$ , the  $\Delta V_{ph}(x)$  crossed over to a non-linear lineshape, as shown in **Figure 5.7b**. This model clearly accounts for the crossover from linear to non-linear lineshape, with an increase in the  $L_{Au-Au} / w$  ratio as mentioned above. It is to be noted that the magnitude of  $\Delta V_{ph}(x)$  decreases with an



increase in the interfacial-contact area, which is a direct consequence of the radial distribution of holes. Nevertheless, this trend can be exploited to design an efficient two-dimensional PSD.

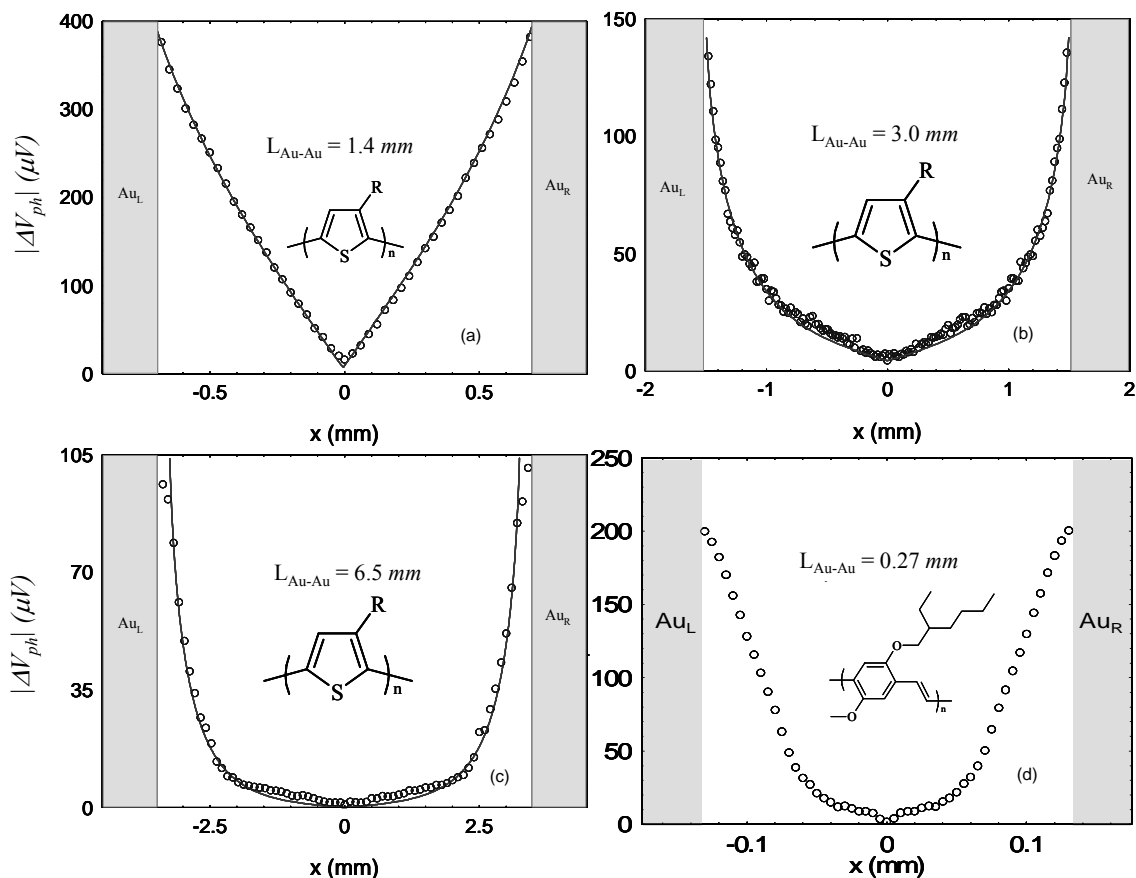


**Figure 5.7** Differential photovoltage  $\Delta V_{ph}$  ( $=|\Phi_L - \Phi_R|$ ) measured as a function of spatial position of laser beam spot of diameter  $10 \mu m$  for different inter-electrode separation; (a)  $L_{Au-Au} = 1.4$  mm, (b)  $L_{Au-Au} = 3$  mm and (c)  $L_{Au-Au} = 6.5$  mm for a constant  $w = 1.5$  mm for P3HT based 1D-PSDs while (d)  $L_{Au-Au} = 0.27$  mm for same  $w = 1.5$  mm MEHPPV based PSD. Solid line in (a), (b) and (c) is simulated profile and chemical structure of polymers in insets.

### 5.3.5 Chopper Frequency Dependence of LPV

Semiconducting polymers have distribution of spatially and energetically disordered traps, which severely affects the charge transport in these materials. In terms of circuit model, capacitors are best representatives of these trap centers, where carriers produce relaxation, limited output current. In order to estimate these lateral and

transverse capacitance values, chopper frequency dependent LPV measurements were carried out.  $\Delta V_{ph}(\omega)$  varies as  $1/\omega$  in the range  $20 \text{ Hz} < \omega < 3.5 \text{ KHz}$  indicating the importance of the capacitive elements [17, 18] in the model. These steady state measurements were carried out on P3HT based sample with  $L_{\text{Au-Au}} = 6.5 \text{ mm}$  &  $w = 1.5 \text{ mm}$ , as shown in inset of *Figure 5.8*.

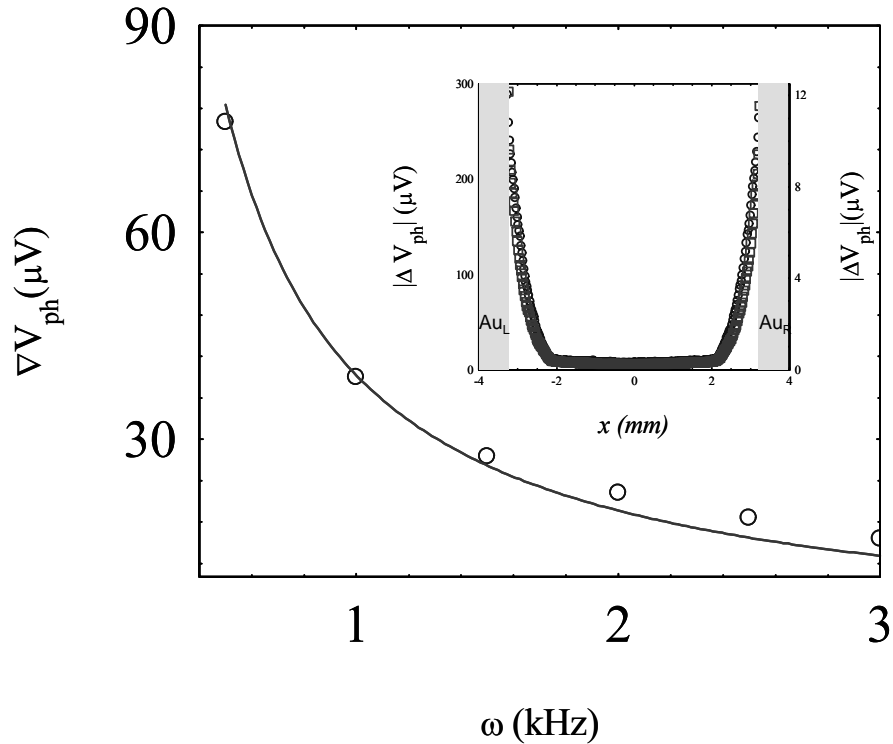


**Figure 5.8** Spatial response of differential photovoltage  $|\Delta V_{ph}|$  ( $= |(\Phi_L - \Phi_R)|$ ) at  $\omega = 75 \text{ Hz}$  (o) and  $1.5 \text{ KHz}$  ( $\square$ ) using lock-in amplifier with illumination by He-Ne laser ( $\lambda = 543 \text{ nm}$ , power =  $60 \mu\text{W}$  and spot diameter  $\sim 10 \mu\text{m}$ ) from semitransparent Al side. Solid line is simulated fit to data. The frequency response for same device ( $L_{\text{Au-Au}} : w :: 6.5 \text{ mm} : 1.5 \text{ mm}$ ).

### 5.3.6 Temperature Dependence of LPV

The temperature dependence of LPV illustrates that  $\Delta V_{ph}(x)$  is not preserved with respect to temperature ( $T$ ), as shown in *Figure 5.9*. For lower  $T$ , apart from the decrease in magnitude of  $\Delta V_{ph}(x = L_{\text{Au-Au}}/2)$ , the range for the spatial dependence also decreases. For  $100 \text{ K} < T < 300 \text{ K}$ ,  $\Delta V_{ph}$  at a particular position  $x$  can be modeled in terms of an activated behavior with an activation energy ( $\Delta$ ), where  $\Delta$  has a minimum value of  $9 \text{ meV}$

at  $|x = \pm 3.25| = L_{\text{Au-Au}}/2$ , which gradually increases with  $x$  and appears to reach a saturated value ( $\sim 0.03 \text{ eV}$ ) for  $x \rightarrow 0$  (**Figure 5.9** inset).

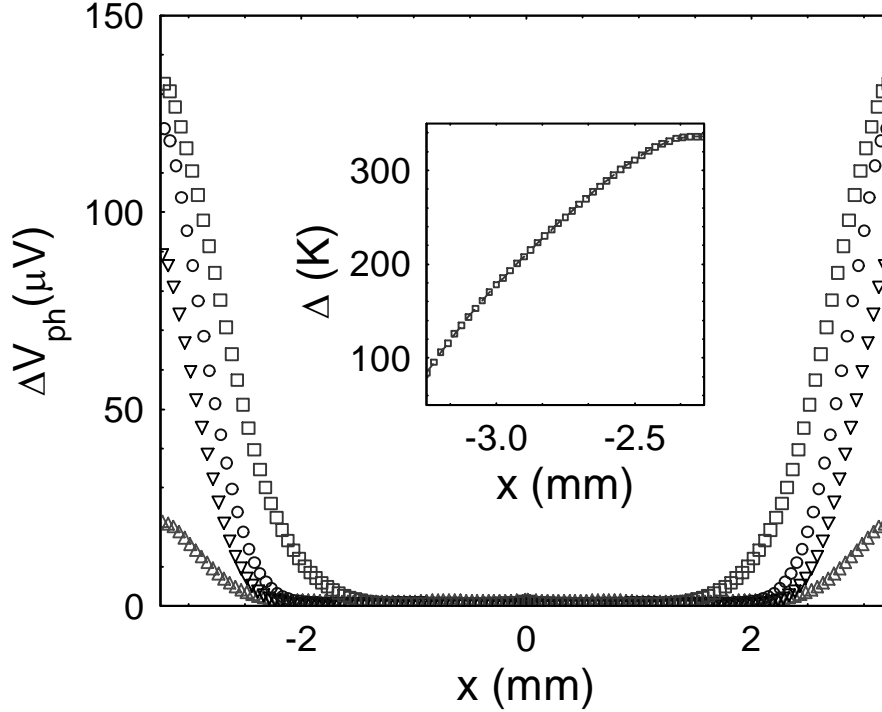


**Figure 5.9** Spatial profile of differential photovoltage  $\Delta V_{ph}$  ( $= |\Phi_L - \Phi_R|$ ) for illumination from glass side at temperature 70 K ( $\Delta$ ), 150 K ( $\nabla$ ), 200 K (o) and 300 K ( $\square$ ) using a He-Ne laser ( $\lambda = 633 \text{ nm}$ , power  $\sim 100 \mu\text{W}$  and beam diameter  $= 100 \mu\text{m}$ ) using a differential lock-in-amplifier. Inset shows the spatial dependence of activation energy ' $\Delta$ ' obtained from temperature dependence of  $\Delta V_{ph}$ .

The temperature dependence of the  $J_L(x)$  was studied to probe the lateral transport characteristics. The complexities involved in the transport processes of these disordered materials were manifested in these results. The multiple traps releasing transport model used for organic semiconductors can be utilized to understand the basic features of the results. The general features of  $|\Delta V_{ph}|(T,x)$  were as follows: (i) The magnitude of  $|\Delta V_{ph}|(x)$  increases with increase in  $T$ . (ii) At lower temperature the spatial dependence of  $|\Delta V_{ph}|(x)$  reduces. (iii) The change in photogeneration of charge carriers with temperature solely cannot explain the  $|\Delta V_{ph}|(T,x)$ , i.e., transport parameters also get modified with

change in temperature. (iv) The activation energy ( $\Delta$ ) (in temperature span 70 K to 300 K) increases as distance increases from either of Au electrode to illumination position and saturates towards the center of device. The temperature dependence can be modeled in terms of Arrhenius behavior as follows:

$$|\Delta V_{ph}| = |\Delta V_{ph0}| \exp\left(-\frac{\Delta}{2kT}\right) \quad (20)$$

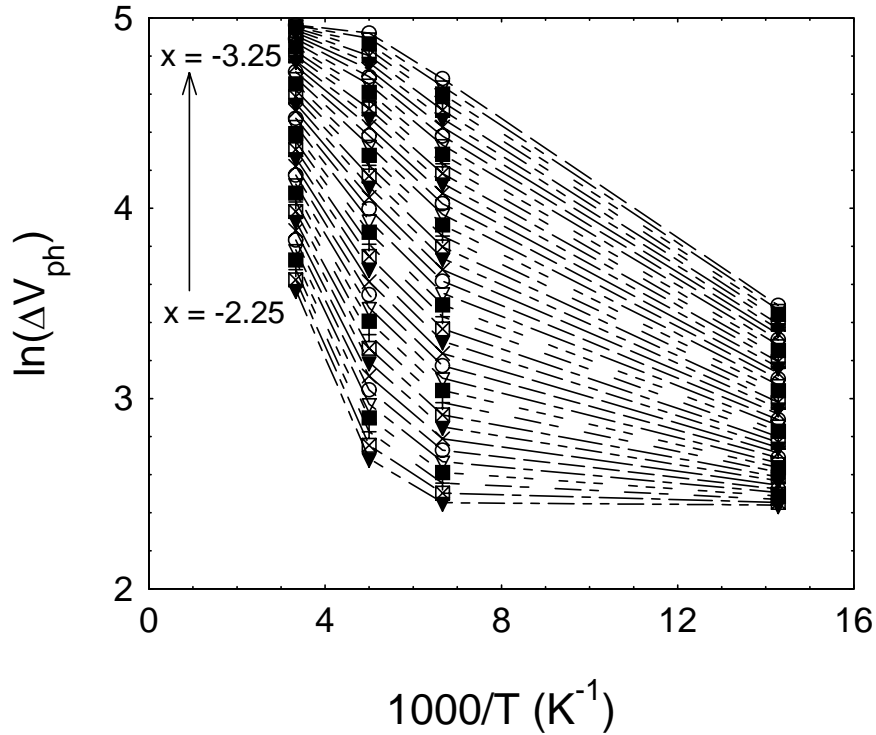


**Figure 5.10**  $\ln\{LPV (= \Delta V_{ph})\}$  versus  $10^3/T$  dependence at different local positions from edge  $Au_L$  ( $x = -3.25$  mm) to towards the center,  $x = -2.25$  mm, for typical device ( $L_{Au-Au} = 6.5$  mm,  $w = 1.5$  mm)

If the photo-carriers generation is away from Au electrode then the carriers trapping is found to be more that result in lesser LPV, as shown in **Figure 5.9**.  $\Delta V_{ph}(T)$  at different  $x$  is plotted (see **Figure 5.10**) to determine  $\Delta(x)$ . The complete physical explanation for the change in  $\Delta$  with illumination positions is found to be difficult, considering the facts about complex temperature dependence of transport parameters in spatially and energetically disordered polymer semiconductors.

### 5.3.7 External Bias Dependence on LPV

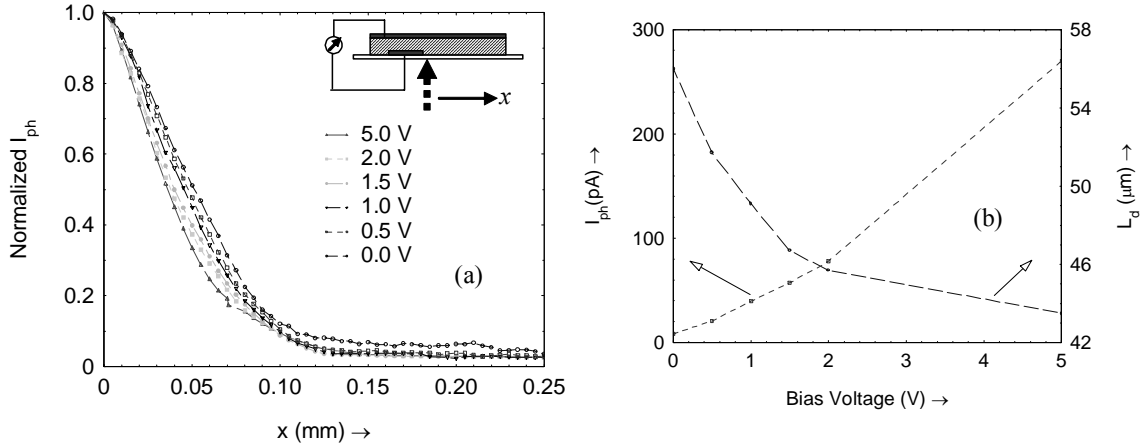


**Figure 5.11** (a) Bias dependence on LPV current profiles using He-Ne ( $\lambda = 633$  nm, power = 60  $\mu\text{W}$  and spot diameter  $\sim 10$   $\mu\text{m}$ ), Al was biased positive. (b) Change in amplitude and LPV decay length with respect to positive bias at Al. Inset shows the device structure.

An external bias was applied on two terminal device structures to determine the change in photogenerated charge carrier transport. There was a mild change observed in the LPV decay length ( $\sim 20$  %), along with a significant change in output photocurrent (almost 90 %) with positive bias on Al electrode (see

Figure 5.11). A modified three terminal device structure was used to utilize this fact in tuning the spatial photo-response of PSDs. In this case Al electrode was deposited in between two Au electrodes (see Figure 5.12a) without overlaps of Schottky interface with Au electrodes. An external bias was applied to Al electrode and photocurrent with transmission profile was obtained as a function of light beam position using lock-in technique, as shown in Figure 5.12b. This device configuration is analogous to MESFET structure, where photocurrent between two Au electrodes with respect to high reverse bias on Al was found to increase. These results can be explained on the basis of higher efficiency of photocarriers generation due to exciton dissociation and charge separation at polymer/Al interface. Lateral photocurrent profiles ( $I_{ph,L}(x)$ ) exhibit an increase in offset

of  $I_{ph,L}(x)$  with an increase in external bias to Al electrode. This positional dependence was found to vanish at high reverse bias condition (positive bias to Al electrode).

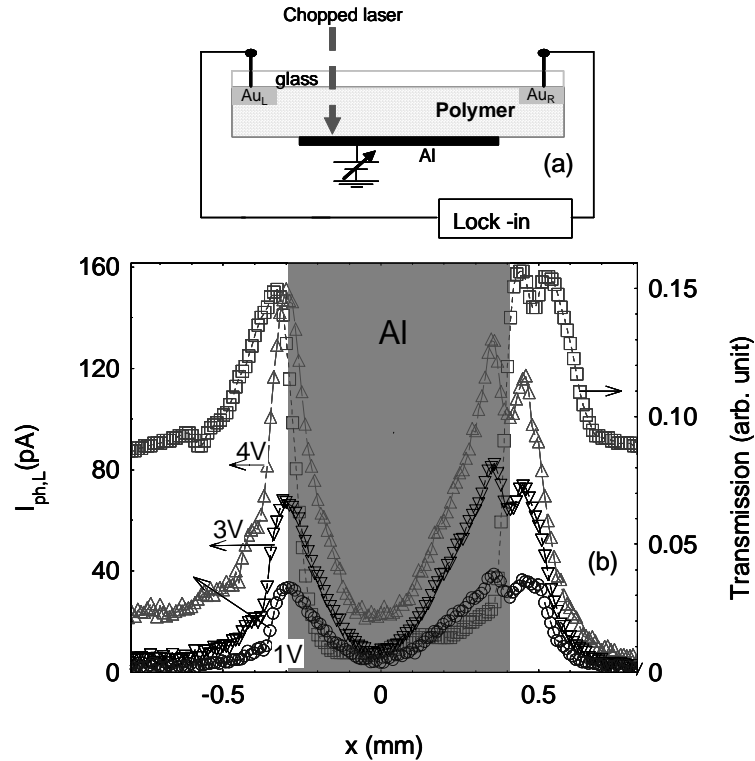


**Figure 5.12** External bias dependence on LPV (a) typical device structure (b) spatial photocurrent response  $|I_{ph,L}(x)|$  at bias voltage 1V (o), 3V (∇) and 4V (Δ) on P3HT based device on illumination with red He-Ne ( $\lambda = 633$  nm, spot diameter =  $10 \mu\text{m}$ , optical power =  $100 \mu\text{W}$ ) and transmission profile recorded simultaneously using lock-in technique.

### 5.3.8 2D Optical Scanning

Two-dimensional PSDs are modified version of 1D PSDs structure, which can provide x-y co-ordinate of optical beam irradiating on any position of active square area of device. There were three model polymer systems studied; among them P3HT was found to be best choice of material for this device. P3HT forms very good 2D transport network where interchain and intrachain hopping probability is highest in lateral plane, this is the reason it led maximum carrier mobility. A typical device structure is shown in **Figure 5.13a**.

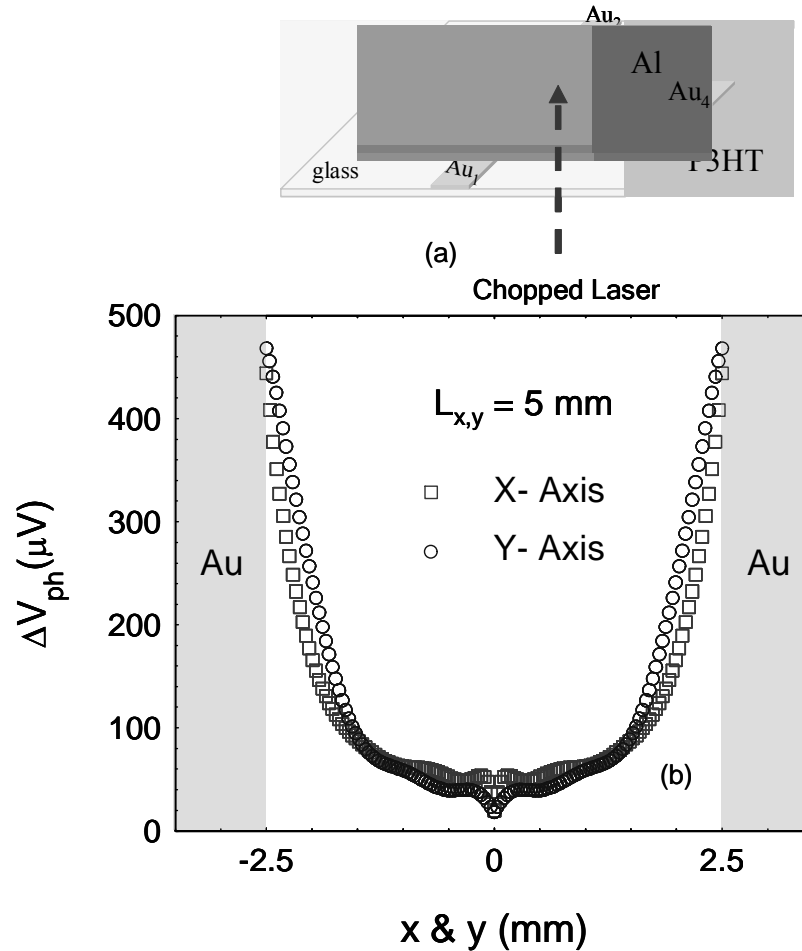


**Figure 5.13** (a) Two-dimensional PSD structure with active area ( $5 \text{ mm} \times 5 \text{ mm}$ ) (b) Spatial differential photovoltage profile in two orthogonal directions (i) between  $Au_1$  &  $Au_2$  ( $\square$ ) while  $Au_3$  &  $Au_4$  were floating and (ii) between  $Au_3$  &  $Au_4$  ( $\circ$ ) while  $Au_1$  &  $Au_2$  were floating when sample was illuminated non-uniformly using diode laser ( $\lambda = 650 \text{ nm}$ , beam spot diameter  $\approx 100 \mu\text{m}$ , optical power  $\approx 0.5 \text{ mW}$ ) by lock-in technique.

A symmetric device structure provides uniform spread of photogenerated charge carriers from the point of illumination according to position of optical beam. There were two spatial lateral photovoltage scans carried out orthogonal to each other (see *Figure 5.13b*). These scans revealed isotropic transport of holes in two different directions (i)

between Au<sub>1</sub> & Au<sub>2</sub> while Au<sub>3</sub> & Au<sub>4</sub> were floating and (ii) between Au<sub>3</sub> & Au<sub>4</sub> while Au<sub>1</sub> & Au<sub>2</sub> were floating. These measurements were carried out using 650 nm diode (Thorlab) laser with spot size  $\sim 100 \mu\text{m}$  at optical power  $\sim 0.5 \text{ mW}$ .

## 5.4 Simulations

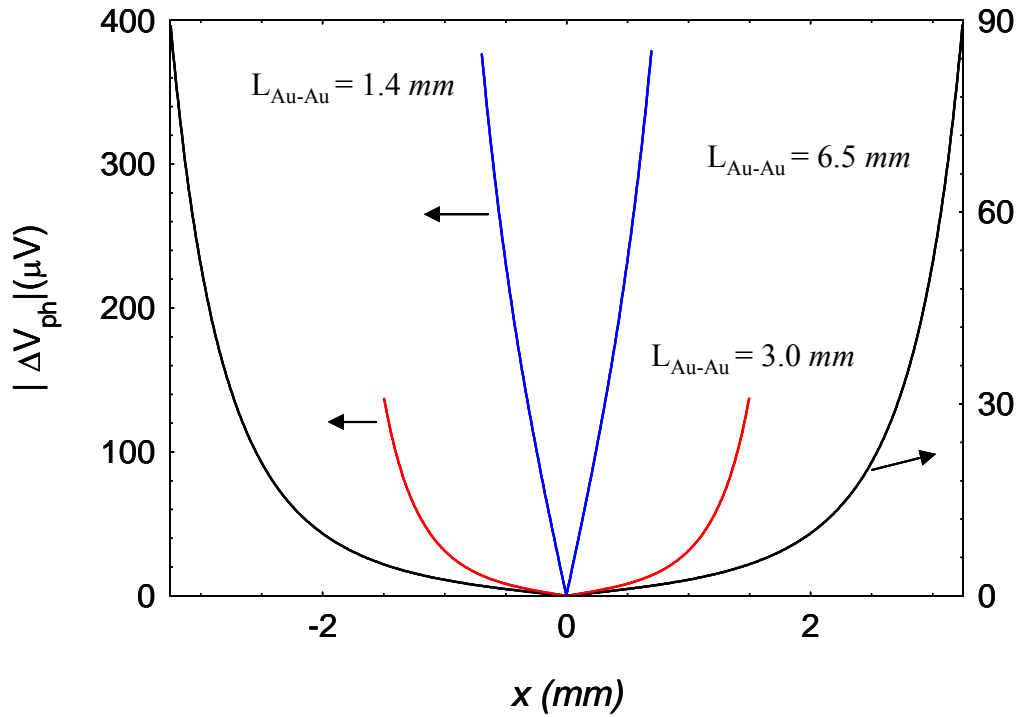


**Figure 5.14** Simulated LPV profiles for three different dimensions of PSDs for same  $w=1.5\text{mm}$

The model described can be solved analytically in a few limiting cases without recourse to a specific form for the SF  $g(r)$ . For example, if the node dimension  $d$  is chosen such that  $d/r_{beam} > 1$ , i.e., only a single node is illuminated and with the neglect of capacitive terms at low chopper frequency limit ( $\omega \rightarrow 0$ ), the set of linear equations (5.15-5.18) may be solved exactly and the resulting photogenerated potential profile is given by (see Eq. 5.19),



$$\phi(r) = \phi_{ill} \left( 1 + \frac{I_s q R_s g(r)}{k_B T} \right)^{-1} \quad (5.21)$$

where  $\phi_{ill}$  is the potential at illuminated node. The potential is seen to decay as the inverse of the SF for large  $r$ . This bears a direct relation to the photogenerated carrier profile  $n(r)$ , since in the small signal limit, whence the excess charge density is proportional to the potential profile ( $n(r) \propto C_i \phi(r)$ )[1], the  $n(r)$  also falls off as the inverse of the SF. The second analytical result obtained by solving the equations close to the centre of the sample is that the LPV has a linear profile close to the centre independent of the device dimensions i.e.  $\Delta V_{ph}(x) \propto |x|$  for  $x \rightarrow 0$  and for an arbitrary  $g(r)$ . The full set of equations for specific model parameters and for a specific form of  $g(r)$  can only be solved numerically.

The first step in making a detailed comparison to experiments is to make a choice for the  $g(r)$  and for the various material and /or device specific parameters of the model such as  $I_{ph}$ ,  $I_s q/k_B T$ ,  $R_s$ ,  $C_s$ , and  $C_t$ . The value for  $I_s$  which gave good fit with all the scan data shown in **Figure 5.7 a-c** and **Figure 5.8** was found to be  $\sim 1.7 \text{ pA}$ , instead of the observed  $I_s \sim 15 \text{ pA}$  possibly arising from a background leakage current factor in the device. Simulated LPV profiles for three different dimensions are shown in **Figure 5.14**. The short circuit photocurrent  $I_{ph}$  between the Au and Al electrodes, for low intensity excitation ( $\approx 100 \text{ } \mu\text{W}$ ) was found to be  $\approx 0.4 \text{ nA}$  for  $L_{\text{Au-Au}} = 1.4 \text{ mm}$ ,  $0.12 \text{ nA}$  for  $L_{\text{Au-Au}} = 3 \text{ mm}$  and  $0.07 \text{ nA}$  for  $L_{\text{Au-Au}} = 6.5 \text{ mm}$  from the I-V measurements of (shorted-Au/P3HT/ Al) devices. Other parameters, such as  $R_s$ ,  $C_s$ ,  $C_t$  and  $g(r)$  can be obtained by (i) a systematic study of the model behavior as a function of the above parameters and (ii) knowledge of the lineshape and frequency response of the lateral photovoltage. The experimental results show that the lineshape of  $\Delta V_{ph}(x)$  crosses over from being linear for  $L_{\text{Au-Au}}/w \cong 1$  (**Figure 5.7a**) to being highly non-linear for  $L_{\text{Au-Au}}/w \cong 4$  (**Figure 5.7c**). This rapid crossover to the non-linearity with an increase in the  $L_{\text{Au-Au}}/w$  ratio places a strong restriction on the functional form of  $g(r)$ .

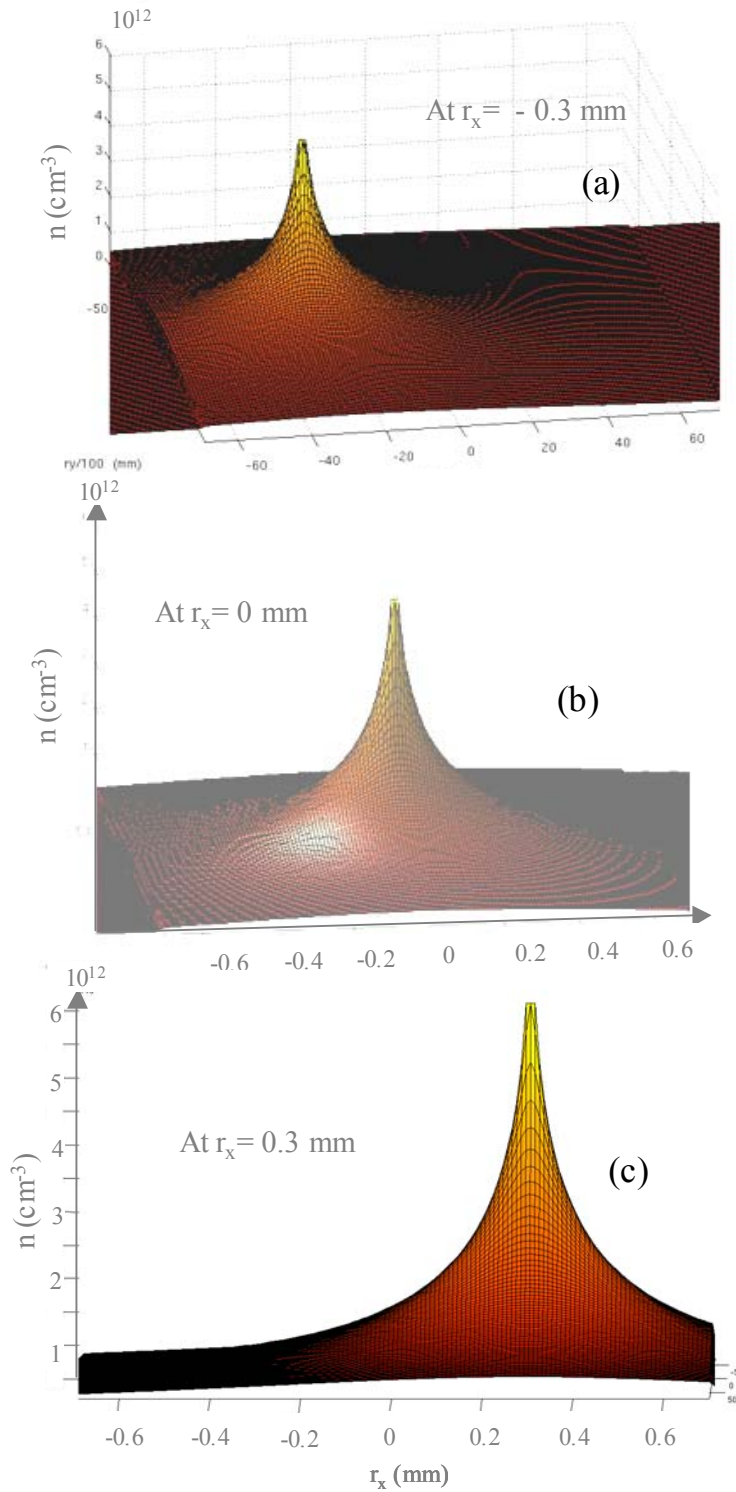


**Figure 5.15** Steady state excess photogenerated hole density profile ( $n(r_x, r_y)$ ) inside P3HT polymer matrix when focused light beam was irradiated at (a)  $r_x = -0.3$  mm, (b)  $r_x = 0$  mm and (c)  $r_x = 0.3$  mm for  $L_{Au-Au} : w :: 1.4 \text{ mm} : 1.5 \text{ mm}$  PSD, depicts the origin of LPV.

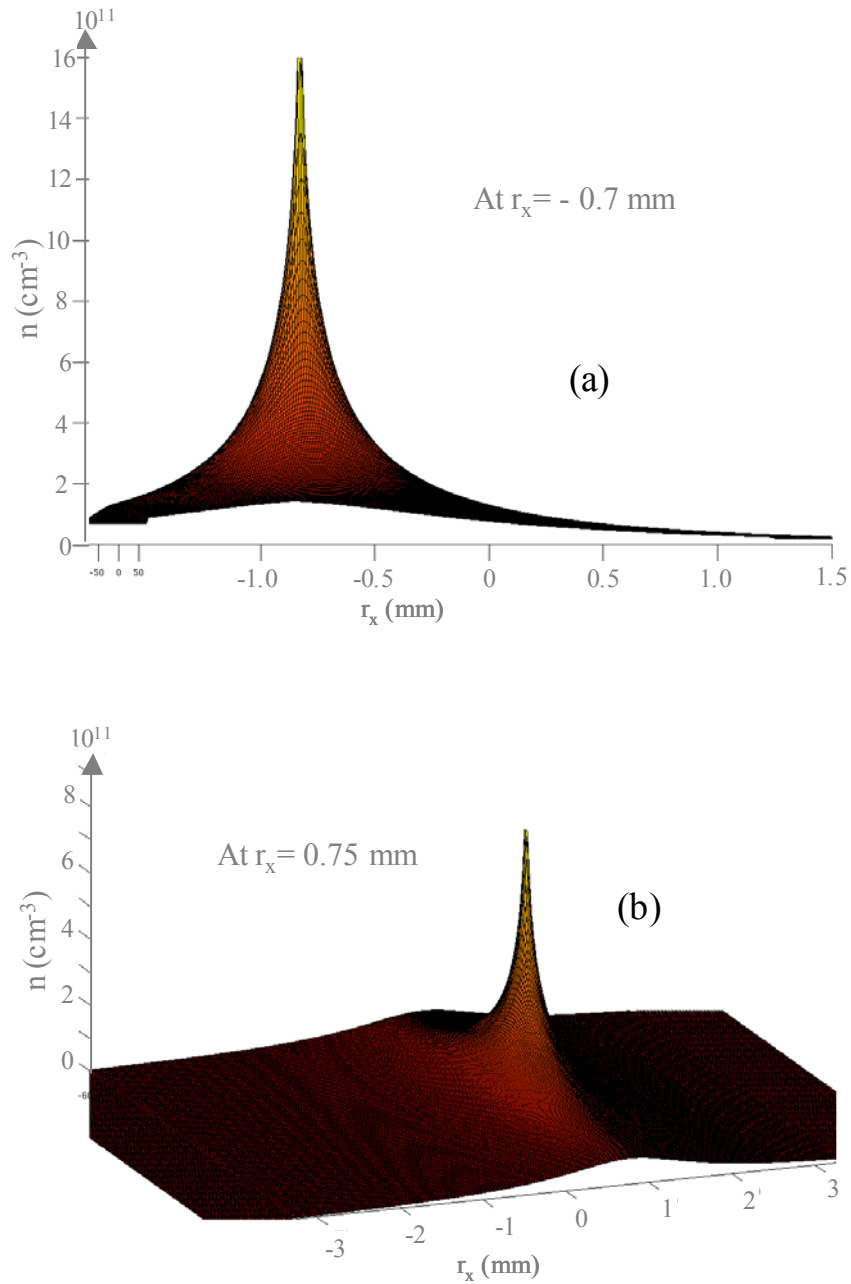


**Figure 5.16** Steady state excess photogenerated hole density profile ( $n(r_x, r_y)$ ) inside P3HT polymer matrix when focused light beam was irradiated at (a)  $r_x = -0.7$  mm for  $L_{Au-Au} : w :: 3 \text{ mm} : 1.5 \text{ mm}$  PSD, (b)  $r_x = 0$  mm and for  $L_{Au-Au} : w :: 6.5 \text{ mm} : 1.5 \text{ mm}$  PSD, depicts the origin of nonlinear LPV due to radially asymmetric charge density profile.

The polynomial and logarithmic forms [19] were found to vary too slowly to be able to account for the rapidity of the crossover; and the only (simple) function which satisfied this criterion was

$$g(r) = \exp\left[\left(\frac{r}{\xi}\right)^\alpha\right] \quad (5.22)$$

where  $\alpha$  is an exponent and  $\xi$  is a length scale characteristic of the material under consideration. This function belongs to a more general class of functions that arise in the study of wave scattering from rough surfaces; where  $\alpha/2$  is called Hurst exponent, which determines how jagged the surface is, while  $\xi$  is an effective cutoff length for roughness [20]. A qualitative analogy from the above in terms of charge carrier scattering was derived, from a disordered network of sites to conjecture, that  $\alpha$  is a measure of disorder and  $\xi$  is a characteristic length scale representing a cutoff for fractal nature of disorder.

## 5.5 Discussion

A systematic study of the model behavior using the above function shows that the lineshape of  $\Delta V_{ph}(x)$  is determined almost completely just by the two parameters  $\alpha$  and  $\xi$  appearing in the  $g(r)$ . The other parameters, as mentioned above play almost no role in the lineshape, but are crucial in determining the magnitude and the frequency response of  $\Delta V_{ph}(x)$ , shown in **Figure 5.8** and **Figure 5.7a-c**. A theoretical fit to the experimental lineshape shown in **Figure 5.14** yields  $\alpha = 0.5 \pm 0.1$  and  $\xi = 50 \pm 5 \mu m$ . The frequency response of  $1/\omega$  found experimentally restricts the choice of  $R_s$ ,  $C_t$  and  $C_s$ . A quantitative fit to the magnitude of  $\Delta V_{ph}(x)$  for the  $L_{Au-Au} = 6.5 \text{ mm}$  sample (**Figure 5.7c**), along with the  $1/\omega$  constraint mentioned above, results in the following model parameters:  $R_s = 10^{11} \Omega/sq$ ,  $C_t = 0.36 \text{ pF}$  and  $C_s = 5 \times 10^{-4} \text{ pF-sq}$ .

Based on these values, the resistivity  $\rho_s = R_s t$  of the polymer medium is estimated to be  $\sim 7 \text{ M}\Omega\text{-cm}$  (for  $t \approx 700 \text{ nm}$ ), and is consistent with the directly determined value [21]. An estimate of depletion width  $w_d$  at Schottky interface, obtained using the transverse capacitance as  $w_d = \varepsilon \varepsilon_r A / C_t$ , where  $A = d^2 = 100 \mu m^2$  and  $\varepsilon_r = 3.5$ , yields  $\sim$

8.5 nm. The model parameters, that have been found by comparison with data for a device of particular  $L_{\text{Au-Au}}/w \cong 4$  (**Figure 5.7c**), can be utilized to predict the lineshapes and magnitudes of the other devices over a wide range of  $L_{\text{Au-Au}}/w$  in excellent agreement with the experimental results (**Figure 5.7a-c**). It is also observed by fitting the lineshapes of the profiles that  $\xi$  decreases by an order of magnitude for  $T < 100$  K. Studies of  $\xi(T)$  can lead to an understanding of physical processes involved in electrical transport characteristics. A characteristic time scale underlying the lateral charge transport is estimated as  $\tau_l \approx R_s C_s \approx 50 \mu\text{s}$ , which may be interpreted in terms of slowly releasing traps yielding large traversal times [17]. Organic semiconductors have a distribution of lifetime for charge carriers; these steady state length scales come from long-lived states. The form of the  $g(r)$  is expected to depend strongly on the morphology of the polymer, e.g. chain orientations and packing of nano-crystalline domains as reported recently for P3HT [22]. Hence the parameter  $\xi \sim 50 \mu\text{m}$  may be interpreted as the underlying characteristic length scales arising from trap concentration energetic (dictated by specific processing conditions to obtain the P3HT films) and is essentially a measure of the spread of the photogenerated charge carrier profile. For example, the same set of measurements on MEHPPV, which also forms a Schottky type interface with Al [18], show significant differences. The observed LPV for MEHPPV systems is quite small with the signal rapidly decreasing as a function of position within tens of  $\mu\text{m}$  from the ohmic electrode in the device geometries for  $L_{\text{Au-Au}}$  as small as  $\sim 280 \mu\text{m}$ . Thus, MEHPPV may be understood within the same framework as having a much smaller  $\xi$  indicating a much greater degree of disorder than P3HT.

The charge carrier profile  $n(r)$  extracted from the model is proportional to  $C_i \phi(r)$ , where the proportionality constant is just the volume of a single node element. In the limiting case of a single illuminated node and purely real impedances, from Eq. (5.21)  $n(r)$  decays as

$$n(r) = n_0 \left[ 1 + \frac{I_s q R_s g(r)}{k_B T} \right]^{-1} \quad (5.23)$$

where  $n_0 = C_t \phi_{ill} / (q d^2 t) \cong 10^{15} \text{ cm}^{-3}$  for P3HT ( $\phi_{ill} = 0.05 \text{ V}$  obtained from the simulation), implying local drift mobility ( $\mu_h = 1 / \rho_s n_0 q$ )  $\approx 10^{-3} \text{ cm}^2 (\text{Vs})^{-1}$ . Upon using the specific form for  $g(r)$  (see Eq. (5.22)) in Eq. (5.23),  $n(r)$  is found to vary as  $n_0 \exp(-(r/\xi)^\alpha)$ . It is to be noted that  $n(r)$  has much larger spatial spread than the optical beam profile  $r_{beam} \ll \xi$ , and gets increasingly asymmetric for beam position close to the Au electrodes highlighting the origin of LPV (**Figure 5.15**) in these systems. Simulation studies on polymer PSDs are useful in prediction of optimum, device structure designs as well as to make an appropriate choice of material.

## 5.6 Conclusions

In summary, a technique is demonstrated based on lateral photovoltage as a valuable method to study charge carrier kinetics in polymer semiconductors. The prevalence of LPV over large length scales, which are several orders of magnitude greater than the microscopic transport parameters, as observed for the case of P3HT, is a direct measure of the efficiency of charge carrier transport and disorder prevailing in the system. The spreading impedance approach describes the results comprehensively and provides additional insight into the microscopic parameters and the photogenerated, charge carrier distribution in these polymer based structures.

The salient features of polymer PSDs of different  $L_{\text{Au-Au}}$  is summarized as follows:

- (i) The spatial-responsivity of P3HT based PSDs scales with  $L_{\text{Au-Au}}$ , as shown in **Figure 5.7**, are comparable to earlier reported results on an organic heterostructure based PSDs [8] and commercially available PSDs like Sharp Inc., Japan 3151F and Hamamatsu S9155,  $L_{\text{Au-Au}} = 5\text{mm}$ , 1D PSD (tested in our laboratory), but with a drawback in terms of the response speed.
- (ii) The signals are a combination of resistive and capacitive response and the time constants governed by the geometry of the device as well as the microscopic parameters such as the defects distribution and energetics.

- (iii) The linearity of the position dependent response is sustained over a wide range of  $L_{\text{Au-Au}}$  ( $25 \mu\text{m} < L_{\text{Au-Au}} < 5 \text{ mm}$ ) albeit non-linearity, observed even for  $L_{\text{Au-Au}} = 2 \text{ cm}$ .
- (iv) The device is most efficient (linear) for wavelength corresponding to the band-edge and thickness comparable to the reciprocal of the absorption co-efficient.
- (v) In presence of a high reverse bias, the position dependence of the photovoltage is considerably reduced (see *Figure 5.12b*) and is consistent with the predictions [1].

## References

---

- [1] G. Lucovsky, *J. Appl. Phys.* **31**, 1088 (1960)
- [2] (i) Abdulhalim, *J. Phys. D: Appl. Phys.* **37**, 1376 (2004)  
(ii) H. Niu, T. Matsuda, S. Okada and M. Takai, *Jpn. J. Appl. Phys.* **16**, 1589 (1977).  
(iii) L. Pereira, D. Brida, E. Fortunato I. Ferreira, H. Aguaas, V. Silva, M. F. M. Costa, V. Teixeira and R. Martins, *J. Non-Cryst. Solids* **299**, 1289 (2002)
- [3] W. Schottky, *Phys. Z* **31**, 913 (1930)
- [4] K. A. Fynn, J. Bajaj, L. Farone, *IEEE Trans. Elect. Dev.* **42**, 1775 (1995)
- [5] S. V. Kalinin, D. A. Bonnell, *J. of Appl. Phys.* **91**, 832 (2002)
- [6] J. Osterman, A. Hallen, S. Anand, *Appl. Phys. Lett.* **81**, 3004 (2002)
- [7] M. W. Xu, T. Hantschel, W. Vandervorst, *Appl. Phys. Lett.* **81**, 177 (2002)
- [8] (i) B. P. Rand, J. Xue, M. Lange, S. R. Forrest, *IEEE Photonics Tech. Lett.* **15**, 1279 (2003)  
(ii) E. Fortunato, D. Brida, I. Ferreira, H. Águas, P. Nunes, R. Martins, *Thin Solid Films* **383**, 310 (2001)  
(iii) J. Henry, J. Livingstone, *Adv. Mater.* **13**, 1023 (2001)
- [9] (i) R. Kersting, U. Lemmer, R. F. Mahrt, K. Leo, H. Kurz, H. Bassler, E. O. Gobel, *Phys. Rev. Lett.* **70**, 3820 (1993)  
(ii) U. Rauscher, H. Bassler, D. D. C. Bradley, M. Hennecke *Phys. Rev. B* **42**, 9830 (1990)  
(iii) J. M. Leng, S. Jeglinski, X. Wei, R. E. Benner, Z. V. Vardney, F. Guo, S. Mazumdar, *Phys. Rev. Lett.* **72**, 156 (1994)
- [10] D. Kabra, Th. B. Singh, K. S. Narayan, *Appl. Phys. Lett.* **85**, 5073 (2004)
- [11] E. H. Rhoderick, R. H. Williams in *Metal semiconductor contacts*, (Clarendon Press, Oxford, 1988).
- [12] I. H. Campbell, T. W. Hagler, D. L. Smith, J. P. Ferraris, *Phys. Rev. Lett.* **76**, 1900 (1996)
- [13] K. Yoshino, H. Takahashi, K. Muro, Y. Ohmori, R. Sugimoto, *J. Appl. Phys.* **70**, 5035 (1991)



- 
- [14] H. Sirringhaus, P. J. Brown, R. H. Friend, M. M. Nielsen, K. Bechgaard, B. M. W. L-Voss, A. J. H. Spiering, R. A. J. Janssen, E. W. Meijer, P. Herwig, D. M. de Leeuw, *Nature* **401**, 685 (1999)
- [15] D. E. Markov, P. W. M. Blom *Phys. Rev. B* **72**, 161401 (2005)
- [16] M. G. Harrison, J. Gruner, G. C. W. Spencer, *Phys. Rev. B* **55**, 7831 (1997)
- [17] E. J. Meijer, A. V. G. Mangnus, C. M. Hart, D. M. De Leeuw, T. M. Kalpwijk, *Appl. Phys. Lett.* **78**, 3902 (2001)
- [18] I. Musa, W. Eccleston, *Jpn. J. Appl. Phys.* **37**, 4288 (1998)
- [19] J. Verma, D. Kabra, K. S. Narayan, N. S. Vidhyadhiraja, *European Phys. J. Appl. Phys.* 2007. (submitted)
- [20] S. K. Sinha, E. B. Sirota, S. Garoff, *Phys. Rev. B* **38**, 2297 (1988)
- (ii) B. B. Mandelbrodt, *The Fractal Geometry of Nature* (Freeman, New York, 1982)
- [21] S. Nagamatsu, S. S. Pandey, W. Takashima, T. Endo, M. Rikuawa, K. Kaneto, *Synth. Met.* **121**, 1563 (2001)
- [22] (i) V. I. Arkhipov, E. V. Emelianova, P. Heremans, H. Bassler, *Phys. Rev. B* **72**, 235202 (2005)
- (ii) I. I. Fishchuk, A. K. Kadashchuk, H. Bässler, D. S. Weiss, *Phys. Rev. B* **66**, 205208 (2002)



# CHAPTER 6

## Summary and Future Directions

---

### 6.1 Summary

This thesis is focused on the study of length scales in model polymer systems, which are of fundamental importance in understanding the transport mechanisms and are crucial parameters for device development. A modified scanning photocurrent contrast microscopy technique was designed and implemented for these studies. Patterned device substrates with dimensions over a large range (1  $\mu\text{m}$  to 2 mm) were used in these experiments. The method provided a measure of the relative degree of order for charge transport, introduced by varying film processing conditions and yields length scales for *p*-type and *n*-type transport in these systems. The generality of the approach to probe both *p*-type and *n*-type can implement for valuable insight in the design of high-efficient solar cells and ambipolar devices. The advantages and the utility of this scanning  $I_{\text{light}}$  approach was particularly evident in case of anisotropic systems such as PFO-TT.

Structural ordering of polymer chains improved the photogenerated charge carriers transport processes in nematic liquid crystalline oriented polymer films. The results obtained from these studies gave an insight of interchain and intrachain hopping processes that occur in these materials. Mobility-lifetime product was found to be an order higher for both electrons and holes, in the case of intrachain transport (transport along aligned chains direction). Decay length ratios for electrons and holes exhibited higher degree of ambipolar conduction. Enhanced transport in aligned direction and higher degree of ambipolar conduction compliment this material for their good performance in optoelectronic devices. These studies envision the use of this polymer for polarization photo-sensor, polarized light emitting diodes and light-emitting transistors.

An outcome of the studies led to the explanation of lateral photovoltaic (LPV) effect observed in these systems. LPV was observed using a local optical probe on

device structures consisting of the semiconducting polymer film with a Schottky type back contact and a front pair of ohmic contacts. The measurements carried out for a large range of interelectrode length ranging from 25  $\mu\text{m}$  to 2 cm was studied in detail as a function of temperature, wavelength, and modulation frequency of the photoexcitation. A spreading impedance approach in the context of a discrete circuit element model was used to obtain a quantitative understanding of the spatial dependence and the frequency response of the LPV.

The LPV technique was used as a valuable method to study charge carrier kinetics in polymer semiconductors. The prevalence of LPV over large length scales, which were several orders of magnitude greater than the microscopic transport parameters, as observed for the case of P3HT, is a direct measure of the efficiency of charge carrier transport and the disorder prevailing in the system. The spreading impedance approach described the results comprehensively and provided additional insights into the microscopic parameters and the photogenerated, charge-carrier distribution in these polymer based structures. A successful application of LPV in terms of P3HT polymer based PSD was demonstrated.

The salient features of polymer PSDs of different  $L_{\text{Au-Au}}$  was summarized as follows:

- (i) The spatial-responsivity of P3HT based PSDs scales with  $L_{\text{Au-Au}}$ , was comparable to earlier reported results on an organic heterostructure based PSDs and commercially available PSDs, for example Sharp Inc., Japan 3151F and Hammamtsu S9155,  $L_{\text{Au-Au}} = 5\text{mm}$ , 1D PSD (tested in our laboratory) but with a drawback in terms of the response speed.
- (ii) The signals were a combination of resistive and capacitive responses and the time constants governed by the geometry of the devices as well as the microscopic parameters such as the defects distribution and the energetics.
- (iii) The linearity of the position dependent response was sustained over a wide range of  $L_{\text{Au-Au}}$  ( $25 \mu\text{m} < L_{\text{Au-Au}} < 5 \text{mm}$ ) albeit non-linearity, was observable even for  $L_{\text{Au-Au}} = 2 \text{cm}$ .

- (iv) The device was most efficient (linear) for wavelength corresponding to the band-edge and thickness comparable to the reciprocal of the absorption co-efficient.
- (v) In the presence of a high reverse bias, the position dependence of the photovoltage was considerably reduced.

## 6.2 Future Directions

Studies of interfaces between organic semiconductors and metals indicate variety of processes and contributions from sub-bandgap levels, which arises from the formations of quasiparticles like the bi-polarons, polarons etc. From a device perspective, charge transfer processes occur when organic materials come in contact with the metals. Similar interfacial phenomena are observed at organic-organic, organic – inorganic (nano-composites) and organic-liquid interfaces. These electrostatic phenomena are known from long time. However, the details of the electrostatic interactions have not been clarified, e.g., possibly owing to either the difficulty in the preparation of sophisticated interface or the lack of technique to gain information on nanometer-scale interfacial electrostatic interactions. As such, the issue of electrostatic interactions is still under continuous study. Photo-physics of these semiconductors has achieved enormous attention. The photovoltaic properties of these semiconductors have been studied in different context to get better understanding or to address fundamental roadblocks, which need to be solved, for the optimum efficiency of solarcells. In bulk heterojunction (BHJ) solarcell, a mixture of polymer (donor - acceptor) is being used to enhance charge generation efficiency. The mixing, phase separation of polymers, the percentage effective area of good efficiency and interfacial dynamics are the important factors to be checked with close observations. A local optical probe has specific advantages to study these opto-electronically rich materials. In continuation to the same theme of work with the knowledge of energy levels of semiconductors (amorphous, polycrystalline or crystalline) and correct choice of metals, many interesting interfacial properties (energy transfer, charge transfer or domain boundaries dynamics, nanometric electrostatic phenomena at molecular interfaces etc), along with bulk properties like mobility, resistivity etc., can be addressed using a local optical probe.

There are interesting optically anisotropic systems like discotic molecules, rigid back-bone polyfluorenes derivatives, self assembled supramolecular structure of P3HT etc., that can be aligned on substrates, which induces electrical anisotropic behavior. Material specific optical energy beam and a proper optical setup can give a 3D electrical field distribution to enlighten the photo-physics of these materials. This can be used not only to enhance our understanding, but also to tailor the system with new methodologies. A particular advantage in organic semiconductors is the possibility to engineer macromolecular structure, especially in blend systems, where the phase separation length scales and organization, can be controlled. Application of the electrostatic techniques to these systems is quite challenging, due to the presence of nanostructure level disorders, low dielectric constants enhancing Columbic interactions, quasi charge particles etc. Local optoelectronic processes need to be investigated on sub  $\sim 100\text{nm}$  level to make correlation between morphology and photo-physics of these materials, without damaging the polymer film. A local time resolved photocurrent microscopy, on these domain structures, can reveal important photo-physics of these materials.